Title
Dynamics of Endothelial Metabolomics in Vascular Development and Repair

Author
Beebe, Tyler James

Publication Date
2015

UNIVERSITY OF CALIFORNIA

Los Angeles

Dynamics of Endothelial Metabolomics in Vascular Development and Repair

A dissertation submitted in partial satisfaction of the

requirements for the degree Doctor of Philosophy

in Bioengineering

by

Tyler James Beebe

2015

2015

ABSTRACT OF DISSERTATION

Dynamics of Endothelial Metabolomics in Vascular Development and Repair

By

Tyler James Beebe
Doctor of Philosophy in Bioengineering
University of California, Los Angeles 2015
Professor Tzung Hsiai, Chair

Hemodynamic shear stress is intimately linked with endothelial metabolic effects, regulating key mechanisms in endothelial function, homeostasis, and repair. *In-vivo* modulation of shear stress signaling pathways in the zebrafish model allows for identification of mechanisms with potential therapeutic implications. The following studies combine *in-vivo* zebrafish models with *in-vitro* shear stress studies to characterize the mechanisms whereby shear stress regulates vascular development and repair.

We investigated shear stress-modulated genes via microarray, and identified Angiopoietin-2 (Ang-2), a well known regulator of angiogenesis and vascular development, as a potential target for further mechanistic study. Oscillatory shear stress (OSS) induced Ang-2 mRNA expression in a Wnt-signaling dependent manner. Inhibition of Wnt signaling or Ang-2 expression supressed endothelial cell migration and

tube formation, which were rescued by human recombinant Ang-2 treatment. These results were recapitulated in the embryonic zebrafish model using heat-shock inducible transgenic *Tg(hsp70l:dkk1-GFP)* and *Tg(kdrl:GFP)* embryos injected with Ang-2 morpholino. Inhibition of Wnt signaling with IWR-1 also impaired vascular repair after tail amputation, which was rescued by injection of zAng-2 mRNA. Taken together, this data demonstrated shear stress activated Ang-2 via canonical Wnt signaling in vascular endothelial cells, and recapitulated shear stress-Wnt-Ang-2 signaling vascular repair in the zebrafish model.

Shear stress-modulated gene- and protein-based mechanisms result in significant changes at the metabolomic level. In the second part of my thesis, we examined the role of emerging mechano-sensitive metabolic pathways in vascular repair. Metabolomic analysis revealed both pulsatile shear stress (PSS) and OSS significantly increased endothelial glycolytic metabolites, but decreased gluconeogenic metabolites. Additionally, both OSS and PSS up-regulated the expression of PKCε. We therefore tested whether shear stress modulates endothelial metabolomics to promote vascular repair via PKCε-mediated glycolytic metabolites. Treatment with pro-glyocolytic metabolites *in-vitro* rescued tube formation following treatment with siPKCε. To recapitulate vascular repair in transgenic *Tg(flk1:GFP)* zebrafish embryos, we decreased viscosity and fluid shear stress by micro-injection of *GATA-1a* morpholino oligonucleotide (MO). In the zebrafish tail amputation model, *GATA-1a* MO impaired and delayed vascular repair. Co-injection of PKCε mRNA with *GATA-1a* MO rescued this phenomenon. Injection of *epo* mRNA to increase viscosity resulted in enhanced tail repair. Overall, our studies revealed that shear responsive VEGFR- PKCε-metabolomic signaling modulates glycolytic metabolites to influence vascular repair.

Mitochondria are the metabolic center of the cell, and mitochondrial state is intimately linked to endothelial function. To further investigate the effect of shear stress on endothelial metabolic function, we examined the effect of physiological pulsatile shear stress (PSS) on mitochondrial membrane potential ($\Delta\Psi_m$) and the role of Mn-SOD expression on $\Delta\Psi_m$. PSS induced a dynamic increase in $\Delta\Psi_m$, while silencing Mn-SOD attenuated PSS-mediated $\Delta\Psi_m$ increase. Mn-SOD mimetic MnTMPyP increased $\Delta\Psi_m$ to the similar extent as induced by PSS. Our findings suggest that PSS modulates mitochondrial function by increasing mitochondrial $\Delta\Psi_m$, in part, via Mn-SOD up-regulation.

In addition to using the embryonic zebrafish model to investigate vascular repair, we worked to develop technologies enabling the use of the adult zebrafish as a model for genetic and chemically-induced cardiomyopathies. To address the confounding effects from sedation of fish and removal from the aquatic habitat for micro-electrocardiogram (μECG) measurements, we developed waterproof and wearable flexible electronic sensors to uncover the circadian variation in heart rate (HR) and heart rate variability (HRV). Innovations including an ultra-soft silicone integrated jacket, matching Young's modulus to the fish surface, and embedded micro-glass spheres to reduce the effective density enabled physiological ECG telemetry in the fish's natural habitat without the need for sedation. The novel features of the flexible silicon jacket for μECG telemetry unraveled the biological clock and normalization of QT intervals at following ventricular resection at 26 days post ventricular amputation, providing the first evidence of new physiological phenomena during cardiac injury and repair. Additionally, we revealed Amiodarone-mediated QTc prolongation, HR reduction and HRV increase otherwise masked by sedation. This light weight and waterproof design holds promise to advance the next generation of mobile health and drug discovery.

This dissertation of Tyler James Beebe is approved.

Daniel Kamei

Thao Nguyen

Benjamin Wu

Tzung Hsiai, Committee Chair

University of California, Los Angeles

2015

DEDICATION

This work is dedicated to my wife, family, and friends who have selflessly supported me as well my colleagues and advisors who have pushed me to excel.

TABLE OF CONTENTS

LIST OF TABLES AND FIGURES

Chapter Two: Shear Stress-Activated Wnt-Angiopoietin-2 Signaling Recapitulates Vascular Repair in Zebrafish Embryos

Chapter Three: Dynamics of Endothelial Metabolomics to Promote Vascular Repair

Chapter Four: Pulsatile Shear Stress Increased Mitochondrial Membrane Potential: Implication of Mn-SOD

Chapter Five: Flexible and Waterproof Micro-Sensors to Uncover Zebrafish Circadian Rhythms: The Next Generation of Cardiac Monitoring for Drug Screening

ACKNOWLEDGEMENTS

This thesis is the culmination of an extraordinary journey which would have not been imaginable without the never-ending support and encouragement of so many. I am grateful for my parents, who always fed my thirst for knowledge and discovery from when I was a young child always asking “why?” to when they allowed me to travel all the way to Los Angeles to study at USC. I am thankful for the financial support and opportunity USC gave me to discover my passion for biomedical engineering.

It was at USC where I first met Dr. Tzung Hsiai, who has guided my academic journey from a wide-eyed undergraduate to a still-wide-eyed PhD candidate. He has always been supportive, willing to help with anything, and challenging, pushing me to think deeper and push further. He taught me how to keep an eye towards the future, pushing to apply novel technologies to answer fundamental and clinically relevant questions. He has shown me the true value of teamwork and collaboration, where the whole is much greater than the sum of the parts. This thesis is the culmination of my work under his tutelage, and I am proud of what we have accomplished together.

Transitioning to UCLA, I am grateful for the support of the Bioengineering department, who welcomed me and made me feel at home, even though the blue and yellow took some getting used to. I am especially grateful for Dr. Benjamin Wu, Dr. Daniel Kamei, Anne-Marie Dieters, and Stacey Tran Fong who helped our transition be as smooth as possible. The staff at the Veterans Administration, especially Jerry Dungan, Tomika Levi, James Gonzales, Marianne Kimmerle, and Jackie Pious-Gaines, helped our lab to get established and helped me to learn to navigate the VA system. I would also like to thank my thesis committee, Dr. Thao Nguyen, Dr. Benjamin Wu, and, Dr. Daniel Kamei for their advice and support.

An adventure like this cannot be undertaken alone, and I am indebted to all of my colleagues who I have worked alongside. I am especially grateful for Dr. Rongsong Li, Dr. Nelson Jen, Juhyun Lee, Dr. Rene Packard, Hilary Chen, Amir Kaboodrangidaem, Eugene Song, Kyung-in Baek, Dr. Fei Yu, Dr. Lisong Ai, Dr. Hung Cao, Dr. Jianguo Ma, Dr. Yichen Ding, and Dr. Peng Fei. Working alongside them has made this experience possible, and much more enjoyable.

I have also had the privilege of working with many great people from many different institutions including Shell Zhang and Dr. Y.C. Tai from Caltech, Dr. BongJin Kang and Dr. Kirk Shung from USC, Dr. Xiaolei Xu from the Mayo Clinic, and Dr. Neil Chi and Dr. Yury Miller from UCSD. Within UCLA, my work has been greatly enhanced via collaboration with Howard Choi, Dr. David Liem, Dr. Peipei Ping, Dr. Thao Nguyen, Hirohito Shimizu, Dr. Yuan Dong, and many others.

Last, but certainly not least, throughout this whole process I have relied on the daily support and encouragement of my wife, Michelle, who has celebrated my success and encouraged me in the midst of failures. In her, God gave me a perfect partner, and I am excited for the future He has for us together.

CURRICULUM VITAE

2010 B.S. in Biomedical Engineering, University of Southern California

PUBLICATIONS

Guan Z, Lee J, Dong S, Jen N, Beebe T, Hsiai T, Ho CM, Fei P. “A compact plane illumination plugin device to enable light sheet fluorescence imaging on an inverted wide-field microscope.” *Biomedical Optics Express.* (in press).

Zhang X*, Beebe T*, Jen N, Lee CA, Tai Y, Hsiai TK. “Flexible and waterproof micro-sensors to uncover zebrafish circadian rhythms: The next generation of cardiac monitoring for drug screening.” *Biosens Bioelectron*. 2015 Sep 15; 71:150-7.
*Authors contributed equally

Zhao Y*, Cao H*, Beebe T*, Zhang H, Zhang X, Chang H, Scremin O, Lien CL, Tai YC, Hsiai TK. “Dry-contact microelectrode membranes for wireless detection of electrical phenotypes in neonatal mouse hearts.” *Biomed Microdevices.* 2015 Apr; 18(2):40.
*Authors contributed equally

Li R, Navab K, Hough G, Daher N, Zhang M, Mittelstein D, Lee K, Pakbin P, Saffari A, Bhetraratana M, Sulaiman D, Beebe T, Wu L, Jen N, Wine E, Tseng CH, Araujo JA, Fogelman A, Sioutas C, Navab M, Hsiai TK. “Effect of exposure to atmospheric ultrafine particles on production of free fatty acids and lipid metabolites in the mouse small intestine.” *Environ Health Perpect.* 2015 Jan; 123(1):34-41.

Li R*, Beebe T*, Jen N*, Yu F, Takabe W, Harrison M, Cao H, Lee J, Yang H, Han P, Wang K, Shimizu H, Chen J, Lien CL, Chi NC, Hsiai TK. “Shear stress-activated Wnt-angiopoietin-2 signaling recapitulates vascular repair in zebrafish embryos.” *Arterioscler Thromb Vasc Biol*. 2014 Oct; 34(10):2268-75.
*Authors contributed equally

Cao H*, Yu F*, Zhao Y*, Scianmarello N, Lee J, Dai W, Jen N, Beebe T, Li R, Ebrahimi R, Chang DS, Mody FV, Pacella J, Tai YC, Hsiai T. “Stretchable electrochemical impedance sensors for intravascular detection of lipid-rich lesions in New Zealand White rabbits.” *Biosens Bioelectron*. 2014 Apr 15; 54:610-6.
*Authors contributed equally

Lee J, Moghadam ME, Kung E, Cao H, Beebe T, Miller Y, Roman BL, Lien CL, Chi NC, Marsden AL, Hsiai TK. “Moving domain computational fluid dynamics to interface with an embryonic model of cardiac morphogenesis.” *PLoS One*. 2013 Aug 23; 8(8).

Li R, Mittelstein D, Fang K, Beebe T, Quigley K, Berliner J, Hsiai TK. “Angiopoeitin-2 modulates Survivin expression in OxLDL-induced endothelial apoptosis.” *Biochem Biophys Res Commun.* 2012 Jan 6; 417(1):619-22.

Yu F, Dai X, Beebe T, Hsiai T. “Electrochemical impedance spectroscopy to characterize inflammatory atherosclerotic plaques.” *Biosens Bioelectron.* 2011 Dec 15; 30(1):165-73.

Li R, Beebe T, Cui J, Rouhanizadeh M, Ai L, Wang P, Gundersen M, Takabe W, Hsiai TK. “Pulsatile shear stress increased mitochondrial membrane potential: implications of Mn-SOD.” *Biochem Biophys Res Commun*. 2009 Oct 16; 388(2):406-12.

Li R, Ning Z, Cui J, Khalsa B, Ai L, Takabe W, Beebe T, Majumdar R, Sioutas C, Hsiai T. “Ultrafine particles from diesel engines induce vascular oxidative stress via JNK activation.” *Free Radic Biol Med.* 2009 Mar 15; 46(6):775-82.

Chapter One: Introduction

1.1 Shear Stress and Endothelial Function

Endothelial cells form the inner lining of all blood vessels, serving as a barrier and regulating nutrient transport to surrounding tissue, and also coordinating vessel development [1]. Hemodynamic blood flow imparts shear stress, cyclic stretch, and hydrostatic pressure on the endothelium [2, 3]. While cyclic stretch plays an important role maintaining endothelial function [3], shear stress exerts a significant impact in directing developmental, physiological, and pathophysiological endothelial responses [3-9].

Shear stress is the parallel friction drag force generated by blood flow over the endothelium. The contractility of the heart imparts cyclic variations in shear stress. The local spatial ($\partial\tau/\partial x$) and temporal ($\partial\tau/\partial t$) components of shear stress largely determine endothelial cell phenotypes [10-13]. At the lateral wall of bifurcations, oscillatory shear stress (OSS), bidirectional with zero net forward flow, has been implicated in induction of oxidative stress and inflammation, initiation of atherosclerosis, and is considered to be “pro-atherogenic” [12, 14-16]. Conversely, pulsatile shear stress (PSS), unidirectional with high shear flow, which develops in the straight portions of arteries, promotes anti- thrombotic, anti-inflammatory, anti-oxidant responses, and is considered “anti-atherogenic” [3, 17-19].

Shear stress modulates many endothelial functions, such as vessel permeability, proliferation, endothelial activation, and other homeostatic responses, through complex mechanotransduction signaling pathways [2, 3, 6]. Endothelial cells rely on multiple different mechanosensor systems to transduce mechanical signals. Integrins, transmembrane protein receptors that bind cells to the extracellular matrix (ECM), are responsible for transducing bulk deformations in cell cytoskeleton through focal adhesions, leading to the activation of focal adhesion kinase (FAK) and c-Src to initiate signaling [2, 20]. Deformations in the cellular cytoskeleton in response to shear stress can also activate the cell adhesion protein PECAM1, which in turn transduces intracellular signaling with PKC [21, 22]. Shear stress also activates mechanically sensitive K^+ and Ca^{2+} ion channels [23]. Additionally, transmembrane proteins such as G protein-coupled receptors and membrane bound structures such as the glycocalyx contribute to mechanosignaltransduction [24]. The activation of these cellular shear stress sensors leads to the activation of multiple signaling molecules including protein kinase C (PKC), FAK, c-Src, Rho family GTPases, PI3K, and MAPKs, for the initiation and propagation of multiple signaling pathways [2, 22, 24].

1.2 Shear Stress and Vascular Development

Vascular development and repair are key processes in wound healing [25], embryonic growth [26], and are an essential component of tumor growth and metastasis [27]. Vascular endothelial cells are continually subjected to shear stress, which is intimately involved in stem cell [28, 29] and mesenchymal progenitor [30] differentiation into vascular endothelial cells[28, 31-35].

The development and maturation of the vasculature is a complex process involving many factors contributing to an integrated sequence of events [1]. An endothelial tip cell leads vascular sprouting, followed by endothelial stalk cells which elongate the branch through proliferation [1]. This process has been shown to be under the strict control of VEGF and Notch signaling. VEGF promotes tip cell induction and filopodia formation as well as inducing the expression of Notch ligand Delta-like 4, which activates Notch signaling [36]. Two additional key growth factors are angiopoietin-1 (Ang-1) and angiopoietin-2 (Ang-2), whose roles in vascular development have been extensively investigated [37-40]. Shear stress-mediated Ang-2 in mature vascular endothelium was recently reported to play a role in tubulogenesis [41] and to confer atheroprotection [42].

While Ang-1 is constitutively released by the perivascular cells, Ang-2 is released from the Weibel-Palade bodies in endothelial cells [43, 44]. Ang-2 binds to endothelial specific receptor tyrosine kinase 2 (TIE-2), and acts as a negative regulator of Ang-1/TIE-2 signaling during angiogenesis [45]. Earlier studies demonstrated that Ang-2 release from Weibel-Palade bodies is induced by endothelial stretch, which occurs during hypertension [46]. However, the mechanisms underlying reactivation of developmental genes such as Ang-2 in endothelial cells remain elusive.

Hemodynamic forces are complex regulators of endothelial homeostasis [47]. Disturbed flow, including oscillatory shear stress (OSS), is a bidirectional flow associated with a net-zero forward flow that develops in the curvatures or branching points of the vasculature [48-51]. OSS-induced Ang-2 promotes tubular formation and migration of cultured endothelial cells [41]. While stretching isolated arterial endothelial cells further promotes the paracrine effect of Ang-2 release, Ang-1 release inhibits these effects [46]. Ang-2 stimulates arteriogenesis in C57Bl/6J mice with a ligated femoral artery [52], and confers atheroprotection in apo*E*-null mice. In contrast, over-expression of Ang-1 induces smooth muscle cell migration and monocyte chemotaxis [42]. However, there remains a paucity of literature in shear stress-activated developmental genes, and the mechanisms underlying OSS-induced Ang-2 expression remain to be elucidated.

1.3 Shear Stress and Endothelial Metabolomics

While many studies have focused on the genomic and proteomic processes involved in vessel development and repair, as well as the effect of shear stress on gene expression and protein post-translational modification, these approaches present an incomplete picture of the cellular state. Genes and proteins are highly subject to epigenetic regulation and post-translational modification, respectively, which can drastically alter the observed phenotype [53]. Emerging technologies in mass spectrometry have advanced the field of metabolomics, the study of small chemical transformed during metabolism, to provide a functional snapshot of ceullular state [53-56].

Many diseases such as cancer and diabetes are known to have strong effects on cellular metabolism [57, 58]. Recently identified metabolites; namely, polyamines such as spermine for acute stroke, cinnamoylglycine, nicotinamide, and cysteine-glutathione disulfide for kidney cancer, and 3-hydroxykynurenine and oxidized glutathione for Parkinson disease, have further led to new biomarkers and therapeutic targets [59-61]. In this context, elucidating mechano-signal transduction underlying metabolomic pathways paves the way to study cellular homeostasis [62, 63], migration [64], and vascular development [36].

The metabolomic profile of the endothelium is unique in that endothelial cells generate more than 80% of their ATP via the glycolytic pathway despite having immediate access to oxygen in the blood [65]. This is advantageous in the instance of vascularizing avascular tissues through sprouting, where endothelial cells are entering oxygen-depleted tissue [36]. Endothelial cells are resistant to hypoxia in the presence of glucose, but become oxygen-sensitive in a low-glucose environment [66]. Additionally, low-oxidative metabolism generates fewer reactive oxygen species and less oxidative stress in a high-oxygen environment [36]. Triggers such as hypoxia can induce a rapid switch from a long-term quiescent state to active growth [36]. As they switch from quiescence to proliferation and migration, endothelial cells increase their glycolytic flux [67].

In addition to environmental factors, endothelial glycolsyis is subject to numerous hemodynamic forces [68]. Laminar shear stress activates key endothelial mechanosensor Krüppel-like factor 2(KLF2) to suppress 6-phosphofructo-2-kinase/fructose-2,6-biphosphatase 3 (PFKFB3), which synthesizes fructose-2,6-bisphosphate, a potent stimulator of glycolysis [67, 69]. Shear-activated eNOS produces nitric oxide (NO) [70, 71] to activate Protein Kinase C isoform epsilon (PKCε), which, in turn, attenuates production of mitochondrial reactive oxygen species (ROS) to confer cardioprotection via metabolism-related proteins in the setting of ischemia-reperfusion injury [29-32][72-76]. Additionally, shear-responsive VEGF- and eNOS-signaling activates PKCε to modulate endothelial cell proliferation, lumen formation, and cellular homeostasis [77, 78]. [79]. The mechanotranduction signaling pathways underlying PKCε-mediated metabolomic pathways to promote angiogenesis and vascular repair are potential targets for enriching or inhibiting endothelial migration and vascular repair.

1.4 Regulation of Mitochondrial Function

Although the majority of endothelial ATP is generated via glycolysis [65], mitochondria remain a key regulator for signaling cellular responses to environmental cues and maintaining homeostasis [62, 80-84]. One main mode of mitochondrial signaling in the endothelium is the regulated production of reactive oxygen species (ROS) [85], which plays an important role in endothelial migration [64] and atherosclerosis [86-88]. Hemodynamics, particularly fluid shear stress, regulates the generation of vascular nitrogen (RNS) and ROS [48, 50, 89]. While eNOS is the major source of RNS, the NADPH oxidase system is considered as a major source of ROS in vascular endothelial cells [89, 90]. Mitochondria are also an important source of cellular superoxide anion ($O_2^{\cdot -}$) and H_2O_2 [87]. Mitochondrial ROS can regulate VEGF receptor transactivation as well as affect endothelial sprouting and apoptosis [91-93]. Endothelial mitochondrial dysfunction plays a role in a range of cardiovascular disease such as hypertensions and atherosclerosis [94-96].

The formation of mitochondrial ROS (mtROS) is dependent on $\Delta\Psi_m$ [97], and mtROS level increases exponentially as $\Delta\Psi_m$ is hyperpolarized above −140 mV [98]. Mitochondrial membrane potential ($\Delta\Psi_m$) is an important indicator of mitochondrial energetic state and cell viability [99]. Oxidative phosphorylation in the mitochondria drives the proton translocation across the mitochondrial inner membrane to intermembrane space [100], generating an electrochemical proton gradient that is expressed as $\Delta\Psi_m$ [99]. $\Delta\Psi_m$ is coupled with oxidative phosphorylation to drive ATP synthesis [101, 102]. During myocardial reperfusion injury, opening of the mitochondrial permeability transition pore (MPTP) collapses $\Delta\Psi_m$ and uncouples oxidative phosphorylation, resulting in ATP depletion and apoptosis [103, 104]. Fluid shear stress is reported to influence mitochondrial ATP synthesis, which is coupled with $\Delta\Psi_m$ [105].

In response to oxidative stress, mitochondrial manganese superoxide dismutase (Mn-SOD) is up-regulated [106], leading to dismutation of $O_2^{\bullet -}$ anion to H_2O_2. In response to laminar shear stress, cytosolic CuZn-SOD expression is also up-regulated [107]. A potential mechanism of shear stress modulating $\Delta\Psi_m$ via Mn-SOD would help us to elucidate the metabolic effects of shear stress with implications to endothelial homeostasis and vascular repair.

1.5 Zebrafish Model of Vascular Development and Repair

Vascular development and repair are multi-dimensional processes intimately tied to complex micro-environments which are difficult to fully recapitulate *in-vitro*. As angiogenic research has pushed towards clinical relevance, many *in-vivo* models have been developed [108]. The embryonic zebrafish model has become prominent due to a number of advantages over other models such as mice or other small mammals.

During the embryonic and larval stages, embryos are transparent and undergo rapid cardiovascular development, which has been well-characterized [109-111]. Zebrafish have a closed circulatory system, and the anatomical form of the developing vasculature is highly similar to that in humans [109, 110]. The optical transparency allows high-resolution optical imaging of blood vessels anywhere in the developing animal using transmitted light or fluorescent techniques [110]. The small size of zebrafish embryos allows them to receive sufficient oxygen by passive diffusion during early development, leading to normal tissue development in the absence of a functional cardiovascular system [110]. Cardiovascular development, structure, and function are relatively conserved between lower vertebrates and mammals. The small size of the zebrafish further allows for high-throughput analysis in response to genetic, epigenetic, and pharmaceutical perturbations with relevance to development and regeneration [112-115].

There are genetically engineered TALEN and CRISPR models of adult fish to model human disease states, as well as tools including morpholino oligonucleotides and RNA microinjections to genetically modify embryos and test hypotheses [116]. Considering these advantages, the zebrafish model has quickly become prominent in for developmental research, cardiac morphogenesis, and blood vessel development [117-122].

1.6 Zebrafish Cardiac Monitoring

In addition to the benefits outlined above, the adult zebrafish model is of significant research interest due to its exceptional cardiac regenerative capacity. Adult zebrafish have the remarkable capacity to fully regenerate their myocardium after up to 20% ventricular resection within 2 months without evidence of scar tissues [123]. The mechanisms behind this regenerative capacity are the subject of many studies, including fate-mapping studies, cardiomyocyte migration, and focus on the electro-mechanical coupling of regenerated cardiomyocytes [124, 125]. Assessment of physiological functions to study this phenomenon has been hampered, however, by the small size of the fish and the difficulty of performing studies in an aquatic environment.

Over the last decade, the advent of flexible microelectronic membranes is evidenced by the biomedical applications to interrogate electrical depolarization in the small vertebrate hearts [126, 127], and the deployment of intravascular flexible shear stress sensors to assess atherosclerotic plaque[127]. These parylene-based high-density electrode arrays have further enabled electrical stimulation in the retina to restore vision and spinal cord to restore locomotion [128]. Stretchable multi-electrode arrays (MEA) further unravel aberrant electrophysiological phenotypes of small animal models of heart regeneration[129]. The MEA membranes adhere to the non-planar body surface, identifying spatial variations in cardiac injury currents from zebrafish hearts[129]. The PDMS-based epidermal electronics revolutionized non-invasive monitoring for mapping cardiac conduction and brain activity [130, 131]. These high density arrays offer precise spatial control of stimulation and recording otherwise challenging with the traditional fine-wire electrodes [128].

The average length of an adult fish is 2 to 4 cm, accessible for relatively low-cost and high-throughput small molecule screening[132]. Their physiological complexity also provides conserved models of human disease for *in vivo* validation studies [122]. The biological characteristics of zebrafish are suitable for toxicity testing, including eco-toxicology[133]. However, the *Clock* gene involved in the central oscillation to coordinate endogenous rhythms is linked to the generation of circadian rhythms[134]. Thus, sedation of zebrafish influences the circadian variations in heart rate (HR) and heart rate variability (HRV) in response to cardiac injury or to drug testing.

The first micro-electrocardiogram (μECG) signals obtained from adult zebrafish required muscle paralysis [135-137]. The gill motion was arrested to reduce electromagnetic (EMG) artifacts while oxygenation was provided to prevent hypoxia and arrhythmias via a needle-to-mouth resuscitation [135-137]. Our group avoided paralytic agents to establish high signal-to-noise ratios for μECG signals via wavelet transform with Tricaine-based sedation [136, 137]. However, translating the zebrafish model to unequivocal drug screening and toxicity testing in the absence of sedation has remained an unmet challenge.

Chapter Two: Shear Stress-Activated Wnt-Angiopoietin-2 Signaling Recapitulates Vascular Repair in Zebrafish Embryos

This manuscript is adapted with permission and excerpted from:

Li R, Beebe T, Jen N, Yu F, Takabe W, Harrison M, Cao H, Lee J, Yang H, Han P, Wang K, Shimizu H, Chen J, Lien CL, Chi NC, Hsiai TK. “Shear stress-activated Wnt-angiopoietin-2 signaling recapitulates vascular repair in zebrafish embryos.” Arterioscler Throm Vasc Biol. 2014 Oct; 34(10): 2268-75. Wolters Kluwer Health Lippincott Williams & Wilkins © No modifications will be permitted.

2.1 Introduction

Mechanotransduction is implicated in differentiation of embryonic stem cells to vascular endothelial cells [138-140]. Hemodynamics; namely, fluid shear stress, is intimately involved in stem cell [31, 141] and mesenchymal progenitors[142] differentiation to vascular endothelial cells. While the roles of angiopoietin-1 (Ang-1) and angiopoietin-2 (Ang-2) during vascular development have been extensively investigated, shear stress-mediated Ang-2 in mature vascular endothelium was recently reported to play a role in tubulogenesis [143] and to confer atheroprotection [144].

Although Ang-1 is constitutively released by the perivascular cells, Ang-2 is released from the Weibel-Palade bodies in endothelial cells [145, 146]. Ang-2 binds to endothelial specific receptor tyrosine kinase 2 (TIE-2), and acts as a negative regulator of Ang-1/TIE-2 signaling during angiogenesis [147]. Earlier studies demonstrated that Ang-2 release from Weibel-Palade bodies is induced by endothelial stretch, which occurs during hypertension[148]. However, the mechanisms underlying reactivation of developmental genes such as Ang-2 in endothelial cells remain elusive.

Hemodynamic forces are complex regulators of endothelial homeostasis [149]. Disturbed flow, including oscillatory shear stress (OSS), is a bidirectional flow associated with a net-zero forward flow that develops in the curvatures or branching points of the vasculature [16, 150-152]. OSS-induced Ang-2 promotes tubular formation and migration of cultured endothelial cells [143]. While stretching isolated arterial endothelial cells further promotes the paracrine effect of Ang-2 release, Ang-1 release inhibits these effects [148]. Ang-2 stimulates arteriogenesis in an C57Bl/6J mice with a ligated femoral artery [153], and confers atheroprotection in apo*E*-null mice. In contrast, over-expression of Ang-1 induces smooth muscle cell migration and monocyte chemotaxis [144]. However, there remains a paucity of literature in shear stress-activated developmental genes, and the mechanisms underlying OSS-induced Ang-2 expression remain to be elucidated.

Canonical Wnt/β-catenin signaling pathway regulates development, cell proliferation and migration [154]. In this study, we investigated whether shear stress activated Ang-2 via canonical Wnt signaling pathway. Both endothelial Ang-2 expression and Wnt TOPflash reporter activity were up-regulated in response to OSS. While Wnt agonist Wnt3a promoted Ang-2 mRNA expression, Dkk-1 treatment or Ang-2 siRNA inhibited endothelial cell migration and tube formation. Wnt-Ang-2 signaling was further recapitulated in the zebrafish embryos, in which Ang-2 mRNA was down-regulated in heat-shock inducible DKK-1 transgenic *Tg(hsp70l:Dkk1-GFP)* fish. Ang-2 morpholino micro-injection further impaired development of subintestinal vessels (SIV) at 72 hours post fertilization (hpf). Thus, we provide new insights in shear stress-activated Wnt-Ang-2 signaling with a translational implication in vascular development and repair.

2.2 Materials and Methods

2.2.1 Vascular endothelial cell culture and chemical reagents

Human aortic endothelial cells (HAEC) were purchased from Cell Applications (San Diego, CA, USA). The endothelial cells were cultured in endothelial growth medium (Cell Applications, San Diego, CA) supplemented with 4% Fetal Bovine Serum (FBS). HAEC were propagated for experiments between passages 4 and 7. Human recombinant Dickkopf-1 (DKK-1) and human recombinant Wnt3a were purchased from R&D systems (Minneapolis, MN). Human recombinant Ang-2 (0.5 µM) (ProSpec Inc, East Brunswick, NJ) was used to rescue endothelial cell migration and tube formation.

2.2.2 Mechanotransduction of vascular endothelial cells

A dynamic flow system was used to generate pulsatile shear stress (PSS) and oscillatory shear stress (OSS) as previously described [150, 155]. The flow system was designed to simulate physiologic shear stress occurring at human arterial branching points with well-defined slew rates ($\partial\tau/\partial t$), time-averaged shear stress (τ_{ave}), frequency, and amplitude. The cells were applied to flow in DMEM culture medium supplemented with 1% FBS and maintained at a temperature of 37°C and pH of 7.4. Confluent monolayers of HAEC grown on glass slides were subjected to three flow conditions at 1 Hz for 4 hours: 1) control at no flow state, 2) pulsatile flow with time-average shear stress (τ_{av}) = 23 dyne/cm^2 accompanied by a stress slew rate ($\partial\tau/\partial t$=71 dyne/cm^{-2}/s at 1 Hz), and 3) oscillating flow (0±3 dyne/cm^2) with τ_{ave}=0 dyne/cm^2 at 1 Hz. For oscillating flow, minimal forward flow at a mean shear stress of 0.2 dyne/cm^2 was provided every hour to deliver nutrients and to remove waste products from the cells.

2.2.3 TOPflash Wnt reporter activity assay

Wnt signaling was measured via TOPflash lentivirus reporter (Addgene plasmid 24307). Lentiviruses were prepared as reported [156]. HAEC grown to sub-confluence were infected with TOPflash lentiviruses at 1:1 ratio in the presence of 6μg/ml polybrene for overnight incubation. Next day, HAEC were subjected to OSS or treated with 20mM of LiCl as a positive control for 8 hours. The cells were then collected and lysed in passive lysis buffer (PLB, Promega), and luciferase activities were quantified with Luminometer using Bright-Glow substrate (Promega).

2.2.4 Immunoflurorescence and the quantification of nuclear β-Catenin

HAEC monolayers were subjected to OSS for 4 hours as described above, and were fixed with 4% paraformaldehyde thereafter. The cells were incubated with anti-β-Catenin (Cell Signaling Technologies, MA), stained with Alexa Fluor 488 secondary antibody(Life Techologies, NY), and mounted with Vectashield mounting medium with DAPI (Vector Laboratories, CA). Fluorescent images were acquired using an inverted microscope (Olympus, NJ) and a CCD camera (Jenoptik, FL). Nuclear β-Catenin fluorescent intensities were quantified via Matlab (Mathworks, MA). Fluorescent β-Catenin signals would be considered positive if co-localized with DAPI fluorescent, and would be compared with the control as fold-change of control.

2.2.5 Ang-2 knock-down

Scrambled control siRNA, and Ang-2 siRNA were obtained from Qiagen (Valencia, CA). siRNA (60nmol/L) was transfected to HAEC with Lipofectamine RNAiMAX (Invitrogen, Carlsbad, CA) as described previously [157]. Cells were used for confirmation of gene knockdown or function assay 48 hours after transfection. There was no observable damage due to the transfection procedure.

2.2.6 Endothelial cell migration and tube formation assays with Wnt inhibitors and Ang-2 siRNA

For the migration assay, confluent HAEC monolayers were scratched by using the 1000 μL pipette tips. The monolayers were washed once, and the medium was replaced with the endothelial cell medium in the presence or absence of Wnt inhibitor DDK-1 or DMSO (vehicle control). After 6 hours of incubation at 37°C, the original scratch lines were photographed and compared with the control.

For the tube formation assay, HAEC were suspended in DMEM (Invitrogen, Carlsbad, CA) with 25ng/ml of VEGF and 5% FBS. HAEC were added to 96-well plate coated with growth factor-reduced Matrigel (BD Biosciences, San Jose, CA) at 20,000 cells/well. The cells were incubated for 8 hours in the presence or absence of DDK-1. Tube formation was compared between the treatment and control using a phase contrast microscope (Olympus IX70). To determine cell viability, we incubated cells in Matrigel with Calcein AM dye (Molecular Probes) at 5 μM for 15 minutes. In the live cells, this dye was converted to a green-fluorescent Calcein after acetoxymethyl ester hydrolysis by intracellular esterases [158].

2.2.7 Construction of HA-tagged zebrafish Ang-2 (zAng-2) and preparation of zAng-2 mRNA

To facilitate the detection of zAng2 protein, we constructed zAng2 with HA tag. zAng2 cDNA (in plasmid pDONR221) was provided by Dr. Sara Childs at the University of Calgary. The zAng2 cDNA was amplified from the donor plasmid and cloned into the plasmid pCS2+ at the BamH I and EcoR I sites with HA tag sequence at the C-terminal end. Clones with the z-Ang-2 cDNA insert were selected by PCR screening. Four clones with z-Ang2 insert were verified by transfecting the plasmids into HEK-293 cells. RNA was extracted to verify mRNA expression by RT-PCR and zAng2 protein expression was verified by Western blot with anti-HA-tagged antibody. Clone #2 was confirmed to express both zAng-2 mRNA and the HA-tagged z-Ang2 protein (**Supplemental Figure 1**). zAng2 mRNA was made from the clone 2 plasmid using the mMessage SP6 kit (Invitrogen, CA) following the manufacturer's instruction.

2.2.8 Quantitative real-time PCR analysis

Angiopoietin-2 (Ang-2) and Axin2 mRNA expressions were measured by quantitative RT-PCR. Total RNA was isolated using Bio-Rad Total RNA kit (Bio-Rad, Hercules, CA). RNA was reverse-transcribed using iScript™ cDNA synthesis kit (BioRad), followed by PCR amplification with qPCR Master Mix (Applied Biological Materials Inc. Richmond, BC, Canada). Ang-2 mRNA expression levels were normalized to glyceraldehyde-3-phosphate dehydrogenase (GAPDH). The primer sequence of Ang-2, Axin2 and GAPDH were provided in **Table 2.** The differences in C_T values for various intervals versus control were used to determine the relative difference in the levels of Ang-2 mRNA expression.

2.2.9 Western blot analysis

Cells were washed with phosphate-buffered saline, harvested, and lysed with RIPA buffer. The lysate was centrifuged at 12,000g for 10 minutes, and the resulting supernatants were used as the whole cell lysate. Protein concentration was determined using DCP assay (Bio-Rad, Hercules, CA). Proteins were separated by 4–20% polyacrylamide gel with SDS and electroblotted onto the polyvinylidene difluoride membranes (GE Healthcare, Buckinghamshire, UK) and were blocked overnight at 4°C in Tris-buffered saline-Tween20 (TBS-T) containing 5% non-fat dry milk (Bio-Rad, Hercules, CA). Ang-2 protein expression was detected with anti-Ang-2 (SantaCruz), and equal loading was verified by blotting with anti-β-tubulin (Millipore Inc). After treatment with horse radish peroxidase-conjugated anti-goat (Santa Cruz) or anti-mouse IgG antibody (Jackson ImmunoResearch, PA) for 1 hour at room temperature, chemilluminescence signals were developed with Supersignal Western Pico (Pierce) and recorded with FluorChem FC2 (Alpha Inotech Inc, San Leandro, CA). Densitometry scans of western blots were performed by using the software installed in FluorChem FC2.

2.2.10 Vasculogenesis assay using *Tg(kdrl:gfp)* transgenic zebrafish embryos

Transgenic *Tg(kdrl:GFP*) fish, were provided by both Ellen C. Lien at Children's Hospital Los Angles and Jau-Nian Chen at UCLA. Kdrl, also known as flk-1, a VEGF receptor 1, is tissue-specific for vascular endothelial cells. Fish were collected at 0 hour-post-fertilization (hpf). Ang-2 inhibition was performed via micro-injection of anti-sense morpholino oligomer (MO) (GeneTools, LLC, Philomath, OR). The MO sequences used were provided in **Table 2**. Control and Ang-2 MOs were dissolved in water to make 0.3mM stock solution with addition of 0.1mM p53 MO. Immediately after collection at 0 hpf, approximately 30-40 embryos were randomly chosen for morpholino micro-injections with 2nL MO stock for the control, Ang-2 Splicing MO, and Ang-2 ATG MO solutions. To rescue, we co-injected 25ng zAng-2 mRNA with Ang-2 MO. All of the embryos were maintained in E3 medium at 28˚C. After 72 hpf, all of the embryos were examined under fluorescence microscope (Olympus IX70, Olympus, Japan) for vasculature phenotypes. Embryos from each treatment condition were then collected for Ang-2 mRNA expression by quantitative RT-PCR.

2.2.11 Subintestinal vein (SIV) Quantification

Fluorescent Tg(*flk1:GFP*) zebrafish SIV lengths were quantified using a custom Matlab script. Briefly, SIV areas were cropped out from embryo image and fluorescent intensities standardized between samples. SIV structures were extracted by thresholding and skeletonizing the image. The result was summed to determine total SIV lengths in pixels and compared to controls to determine fold changes in lengths.

2.2.12 Heat-shock induction of DKK-1 in transgenic *Tg(hsp70l:dkk1-GFP)* embryos to inhibit Wnt signaling and Wnt target genes

Heat-shock inducible transgenic *Tg(hsp70l:dkk1-GFP)* embryos, provided by Neil C. Chi at University of California, San Diego, were used to inhibit canonical Wnt signaling. DKK-1 acts as a potent inhibitor by binding to Wnt receptors LPR5/6. We heat-shocked the embryos at 48 hpf to show a robust GFP expression. Heat shock-induction of DKK-1 was performed in a 38°C water bath for an hour for twenty embryos (*n*=20). Heat shocked embryos exhibited DKK-1-GFP expression (Olympic IX70 Fluorescence microscope). Quantitative RT-PCR using previously reported Wnt target gene, Axin-2 [159], was performed as a positive control for the effect of DKK-1 induction. Individual heat-shock treatments and subsequent assays were performed in four independent experiments. For each experiment, 4 embryos were collected from heat-shock and control groups and lysed for RNA isolation using Bio-Rad Total RNA kit (Bio-Rad, Hercules, CA). The primer sequences for zebrafish Ang-2, Axin-2 and the reference gene β-actin were presented in **Table 2.**

2.2.13 Inhibition of Wnt signaling via IWR-1 in *Tg(kdrl:GFP)* transgenic embryos

Transgenic *Tg(kdrl:gfp)* zebrafish embryos were used to assess vasculogenesis in response to inhibition of Wnt signaling. IWR-1(Sigma-Aldrich) acts as an inhibitor of the canonical Wnt signaling pathway by affecting the gene Porcupine (porcn), which adds a palmitoyl group to Wnt proteins essential to their signaling ability, and is required for Wnt secretion. To assess the time- and dose-dependent effects on the Wnt signaling pathway, we introduced IWR-1 to the growth medium at two different time frames (24 and 48 hpf) and at two different concentrations (10 and 20 μM) (**Table 1**). DMSO (0.1%) was also introduced to the growth medium at which IWR-1 was added to nullify any unknown effects of DMSO at the gene expression levels. IWR-1 was administered in a solution mixed with 0.1% DMSO (as a solvent). At 72 hpf, quantitative RT-PCR was performed to assess Ang-2 and Axin-2 mRNA expression.

2.2.14 Tail injury study using *Tg(kdrl:GFP)* zebrafish embryos

Transgenic *Tg(kdrl:GFP)* embryos were used to assess vascular repair in response to tail injury. Fish larvae were grown to 72 hpf in standard E3 medium. The larvae were first anaesthetized in 0.02% tricaine solution to allow for precise tail placement. The posterior tail segment was then amputated by approximately 100 µm from the tip of the tail using a surgical scalpel under a stereo microscope (MEIJI Techno EMZ series, MEIJI, Japan). After amputation, fish were isolated and placed into E3 medium, E3 medium with 20µM IWR-1. zAng-2 mRNA injection at 2-cell stage plus IWR-1 was also performed. Fish tail sections were imaged under a fluorescent microscope (Olympus IX71, Olympus, Japan) to visualize the blood vessels immediately after amputation and every 24 hours thereafter over the next 3 days. Images were compared to show the differences in regrowth of blood vessels between the different treatment groups at 0 day post amputation (dpa), 1 dpa, and 3 dpa.

2.2.15 Statistical analysis

Data were expressed as mean ± SD and compared among separate experiments. Comparisons of multiple values were made by one-way analysis of variance (ANOVA), and statistical significance for pairwise comparison was determined by using the Turkey test. *P*-values of < 0.05 were considered statistically significant.

2.3 Results

2.3.1 Oscillatory shear stress activated Ang-2 expression via Wnt signaling

In a dynamic flow system[155], oscillatory shear stress (OSS) up-regulated Wnt signaling activity in HAEC. TOPflash reporter assay demonstrated a 2.3-fold-increase in Wnt signaling activity in response to OSS, and a 2.8-fold increase in response to LiCl, a positive control ($p < 0.05$, n=3) (**Fig. 1A**). In parallel, OSS increased nuclear β-catenin content by 1.33-fold compared to static condition ($p < 0.05$, n=4) (**Fig. 1B**). Wnt signaling inhibitor Ionomycin inhibited nuclear β-catenin translocation (**Supplemental Fig V**). Furthermore, OSS up-regulated Axin-2 mRNA, a well-known Wnt target gene, by 3-fold ($p < 0.05$, n=4), which was attenuated by a Wnt inhibitor, IWR-1 (**Fig. 1C**). OSS also up-regulated Ang-2 mRNA expression by 1.4-fold ($p < 0.05$, n=4), which was attenuated by IWR-1 (**Fig. 1D**). OSS further up-regulated Ang-2 mRNA to a greater extent than did pulsatile shear stress (PSS), and OSS also up-regulated Ang-2 protein expression ($p < 0.05$, n=4) (**Figs. 1E and 1F**). Thus, OSS induced Ang-2 expression via cannonical Wnt signaling in HAEC.[143] .

2.3.2 Ang-2 is a Wnt target gene for endothelial repair

Ang-2 knock-down with siRNA (siAng-2) significantly reduced both Ang-2 mRNA and protein expression (**Figs. 2A and 2B**). Transfecting HAEC with siAng-2 impaired tube formation at 8 hours (**Fig. 2C**), and cell migration at both 4 and 8 hours (**Fig. 2D**). siAng-2 studies were further validated with a second set of independently designed Ang-2 siRNA sequences (**Fig. 2A-2D**).

To assess Ang-2 as one of the Wnt target genes, we demonstrated that human recombinant DKK-1 treatment down-regulated Ang-2 mRNA expression in a dose- and time-dependent manner (normalized to GAPDH, $p < 0.05$ vs. Control, n=3) (**Fig. 3A**), whereas recombinant Wnt3a treatment up-regulated Ang-2 in a dose-dependent manner ($p < 0.05$ vs. control, n=3) (**Fig. 3B**). DKK-1 treatment also impaired endothelial migration (**Fig. 3C**) and tube formation at 8 hours (**Fig. 3D**), which were rescued by recombinant Ang-2 treatment (**Figs. 3C and 3D**). The down-regulation of Ang-2 by DKK-1 was not due to apoptosis since DKK-1 treatment had no effect on cell viability at our time points (**Supplemental Fig II**). Ionomycin treatment similarly reduced endothelial cell migration and tube formation (**Supplemental Fig VI**). Taken together, Ang-2 is a Wnt target gene, with an implication in endothelial repair.

2.3.3 Inhibition of Wnt signaling down-regulated Ang-2 expression in Zebrafish embryos

To recapitulate Ang-2 as a Wnt target gene in zebrafish embryos, we used transgenic *Tg(hsp70l:Dkk1-GFP)* lines . Heat-shock induction of DKK-1-GFP resulted in down-regulation of both Axin-2 and Ang-2 mRNA expression while VE-cadherin expression remained unchanged (**Fig. 4A**); whereas heat shock of wild-type fish did not have any effect on Axin-2 or Ang-2 expression (**Supplementary Fig. III**). To further validate Ang-2 as a Wnt target gene, we used IWR-1, a small molecule Wnt inhibitor, to interrogate Axin-2 and Ang-2 mRNA expression. Both genes were down-regulated in dose- and duration-dependent manners at 72 hpf (**Fig. 4B and 4C**). These findings corroborated Ang-2 as a Wnt target gene in the zebrafish embryos.

2.3.4 Ang-2 Morpholinos (MO) impaired vascular development in Zebrafish embryos

To further elucidate whether Ang-2 was implicated in subintestinal vessel (SIV) development, we used transgenic *Tg(kdrl:GFP)* zebrafish embryos (**Fig. 5A**). Micro-injection of 0.5 µM Ang-2 ATG MO or splicing MO to the 2-cell stage embryos impaired SIV development at 72 hpf (**Fig. 5B, Supplemental Fig. IV**). Co-injection of zebrafish Ang-2 (zAng-2) mRNA restored SIV formation (**Fig. 5B).** Quantitatively, SIV length was reduced by 65% in response to ATG-MO injection, which was rescued by zAng-2 mRNA injection ($p < .01$, $n = 20$) **(Fig. 5C).** Furthermore, Wnt inhibitor IWR-1 impaired SIV formation, which was partially rescued by zAng-2 co-injection **at 72 hpf (Figs. 5D and 5E)..** A similar effect was observed with Ionomycin treatment (**Supplemental Fig VII**). Thus, Ang-2 is implicated in SIV development, recapitulating endothelial tube formation (**Fig. 2**).

2.3.5 IWR-1 impaired vascular repair

We further assessed whether Wnt signaling was implicated in endothelial repair in the *Tg(kdrl:GFP)* zebrafish embryos at 72 hpf. Tail amputation was performed approximately 100 µm from the tip (**Fig. 6A**). In the control group, vascular repair led to a closed loop between dorsal longitudinal anastomotic vessels (DLAV) and dorsal aortas (DA) at 3 days post amputation (dpa) (**Fig. 6A**). Treatment with 10µM IWR-1 inhibited vascular endothelial repair at 3 dpa (**Fig.6A)**. Tail amputation performed at 72 hpf to the fish injected with zAng-2 mRNA at 2-cell stage and treated with 10μM IWR-1 exhibited tail repair at 3 dpa (**Fig. 6A**). Both the control and zAng-2 injection groups exhibited a significantly higher rate of regeneration as compared to IWR-1 treatment alone ($p < .05$, $n = 20$) (**Fig. 6B**). These findings support the implication of Wnt-Ang-2 signaling in vascular repair.

2.4 Discussion

In this study, we recapitulate a shear stress-activated Wnt-Ang-2 signaling pathway using the developmental zebrafish model. In our dynamic flow system, canonical Wnt signaling was implicated in OSS-induced Ang-2 expression [143], which influenced vascular endothelial cell migration and tube formation. In the zebrafish embryos, the mechano-reactivated Wnt-Ang-2 signaling was implicated in both subintestinal vessel development and tail repair. Thus, shear stress-reactivated Wnt target genes (**Supplemental Table I**), in this case, Ang-2 confers therapeutic potential in restoring endothelial repair.

The Wnt/β-catenin signaling pathway plays an important role in both development and tissue repair [160-164]. Several molecules negatively regulate canonical Wnt signaling, including Dickkopfs (DKK-1), the secreted frizzled-related proteins (sFRP-1, sFRP-2, sFRP-3, and sFRP-4), and the Wnt inhibitory factor (Wif-1) [165, 166] as well as small molecules such as IWR-1. Treatment with DKK-1 and siAng-2 knock-down inhibited endothelial cell migration and tube formation. In corollary, Ionomycin, a Calcium ionophore, is well-recognized to down-regulate β-catenin/Tcf signaling in Wnt pathway [167]. In the colon cancer cells, Ionomycin disrupted β-catenin and TCF binding, nuclear translocation of β-catenin, and suppression of TCF complexes binding to its specific DNA-binding sites [168]. We also demonstrated that Ionomycin attenuated nuclear translocation of β-catenin, resulting in: 1) down-regulation of both Ang-2 mRNA and protein expression (**Supplemental Figure V)**, 2) inhibition of tube formation, 3) endothelial migration, 4) proliferation (**Supplemental Figure VI**), and 5) inhibition of SIV development in the zebrafish model (**Supplemental Figure VII)**. In this context, the complementary use of Wnt-signaling inhibitors; namely, DKK-1, IWR-1 or siAng-2 knockdown, with recombinant or zebrafish Ang-2 mRNA corroborated reactivation of Wnt-Ang-2 signaling in vascular endothelial repair.

Using the Angiogenesis PCR SuperArray (PAHS-024), we identified a host of Wnt/β-catenin target genes.. Ang-2 was one of the shear stress-responsive angiogenic factors (data not shown),. In response to low shear stress (1 dyne/cm^2), VEGF-dependent induction of Ang-2/Tie-2 system is implicated in endothelial homeostasis, proliferation and differentiation; in response to high shear stress (30 dyne/cm^2), FOXO1-dependent down-regulation of Ang-2 occurs [169, 170]. We demonstrate that OSS up-regulated Ang-2 mRNA to a greater extent than did PSS, and OSS-regulated Ang-2 protein expression by 2.2-fold (**Figs. 1E and IF**). Furthermore, OSS activated Ang-2 expression via Wnt signaling both in mature endothelial cells and in a developmental zebrafish model. Ang-2 is a secreted glycoprotein that is expressed by endothelial cells and vascular progenitor cells, and the release of Ang-2 from activated endothelial cells antagonizes the binding of Ang-1 to the Tie-2 receptor, thus sensitizing the endothelial cells to pro-angiogenic and/or pro-inflammatory stimuli [147]. Ang-2 promotes endothelial chemotaxis and tube formation by inhibiting Ang-1-mediated phosphorylation of Tie-2 [171]. Over-expression of Ang-2 can impart an anti-angiogenic effect as an Ang-1/Tie-2 inhibitor by disrupting embryonic blood vessel formation, resulting in a phenotype similar to that of Tie-2 knockout [172]. Ang-2 is further implicated in regulating Wnt target Survivin expression to mitigate oxidized LDL-induced apoptosis in human aortic endothelial cells [173]. Elevated Ang-2 levels promote tumor progression [174], and are associated with obesity [175]. Endothelial-specific Ang-2 over-expression further promotes vascular permeability and hypotension during septic shock, whereas inhibition of the Ang-2/Tie-2 interaction attenuates lipopolysaccharide-induced hypotension and reduces mortality rate[176]. Nevertheless, the precise mechanism whereby OSS modulates Ang-2 expression in maintaining endothelial homeostasis and in promoting vascular repair warrants further investigation.

The use of transgenic zebrafish model recapitulated shear stress-reactivated Wnt-Ang-2 signaling pathway. Zebrafish Ang-2 orthologs have been recognized to play an important role in zebrafish vascular development, particularly for intersegmental vessel (ISV) sprouting and subintestinal vessel (SIV) formation prior to 72 hpf [177]. ISV sprouting occurs between 24 hpf to 72 hpf, and SIV formation originate from the duct of Cuvier between 48 to 72 hpf [109]. Both ISV and SIV are anatomic milestones for monitoring disrupted angiogenesis [178]. Analogous to the *in vitro* model of vascular repairs, we demonstrate Ang-2 knock-down with morpholinos resulted in impaired SIV formation in *Tg(kdrl:GFP)* fish (**Fig. 5**). Furthermore, we demonstrate that inhibition of Wnt-signaling pathway disrupted vascular repair in response to tail amputation (**Fig. 6)**. Taken together, these findings provide new mechanotransduction insights underlying the reactivation of Wnt target genes with a therapeutic implication for vascular development and repair.

2.5 Acknowledgements

We are grateful to Dr Nusse at Stanford University School of Medicine for providing us with the plasmid to produce TOPFlash reporter lentiviruses. We are also thankful to Dr Childs at the University of Calgary for providing us with the zebrafish Ang-2 cDNA (in plasmid pDONR221). These studies were supported by the National Institutes of Health R01HL-083015 (Dr Hsiai), R01HD069305 (Drs Chi and Hsiai), R01HL111437 (Drs Hsiai and Chi), and R01HL096121 (Dr Lien).

Table 1. IWR-1 treatment scheme for *Tg* (*kdrl:GFP*）zebrafish embryos

Condition	IWR-1 Concentration	Treatment Start time	Treatment duration
E3 medium + 0.1% DMSO	0	24 hpf	48 hr
E3 medium + 0.1% DMSO	10 μM	24 hpf	48 hr
E3 medium + 0.1% DMSO	20 μM	24 hpf	48 hr
E3 medium + 0.1% DMSO	10 μM	48 hpf	24 hr
E3 medium + 0.1% DMSO	20 μM	48 hpf	24 hr

Table 2. Sequencing Information of qRT-PCR primers and Mopholinos

Primer/MO name	**Sequence**
Human Ang-2 forward	5´- GAC CAC GAG ACT TGA ACT TCA G-3´
Human Ang-2 reverse	5´- GGA TGA TGT GCT TGT CTT CCA TAG -3´
Human GAPDH forward	5’- CCT CAA GAT CAT CAG CAA TGC CTC CT -3’
Human GAPDH reverse	5’- GGT CAT GAG TCC TTC CAC GAT ACC AA -3’
Zebrafish Ang-2 forward	5’- CCA ATC TT CTA AGC CAA TCA GCG GAA -3’
Zebrafish Ang-2 reverse	5’- CCA CAT CTG TCA GTT TGC GCG TGT TT -3’
Zebrafish Axin2 forward	5’- GGA CAC TTC AAG GAA CAA CTA C -3’
Zebrafish Axin2 reverse	5’- CCT CAT ACA TTG GCA GAA CTG -3’
Zebrafish β-Actin forward	5’- TGG ATC AGC AAG CAG GAG TAC G -3’
Zebrafish β-Actin reverse	5’- AGG AGG GCA AAG TGG TAA ACG C -3’
Zebrafish Standard Control MO	5’- CCT CTT ACC TCA GTT ACA ATT TAT A-3’
Zebrafish Ang-2 Splicing MO	5'- TCA TTT GAT CAG CCT CAC CTG CGT C -3'
Zebrafish Ang-2 ATG MO	5'- GGC AGG CTG TCC ATC CCA GGA AAC C -3'
Zebrafish p53 MO	5’- GCG CCA TTG CTT TGC AAG AAT TG -3’
Zebrafish Ang-2 Splicing MO PCR primer forward	5’- AGGAAAGGAAGCTGGAGACC-3’
Zebrafish Ang-2 Splicing MO PCR primer reverse	5’- TGTTACGAGTGGAGCTGGCC-3’

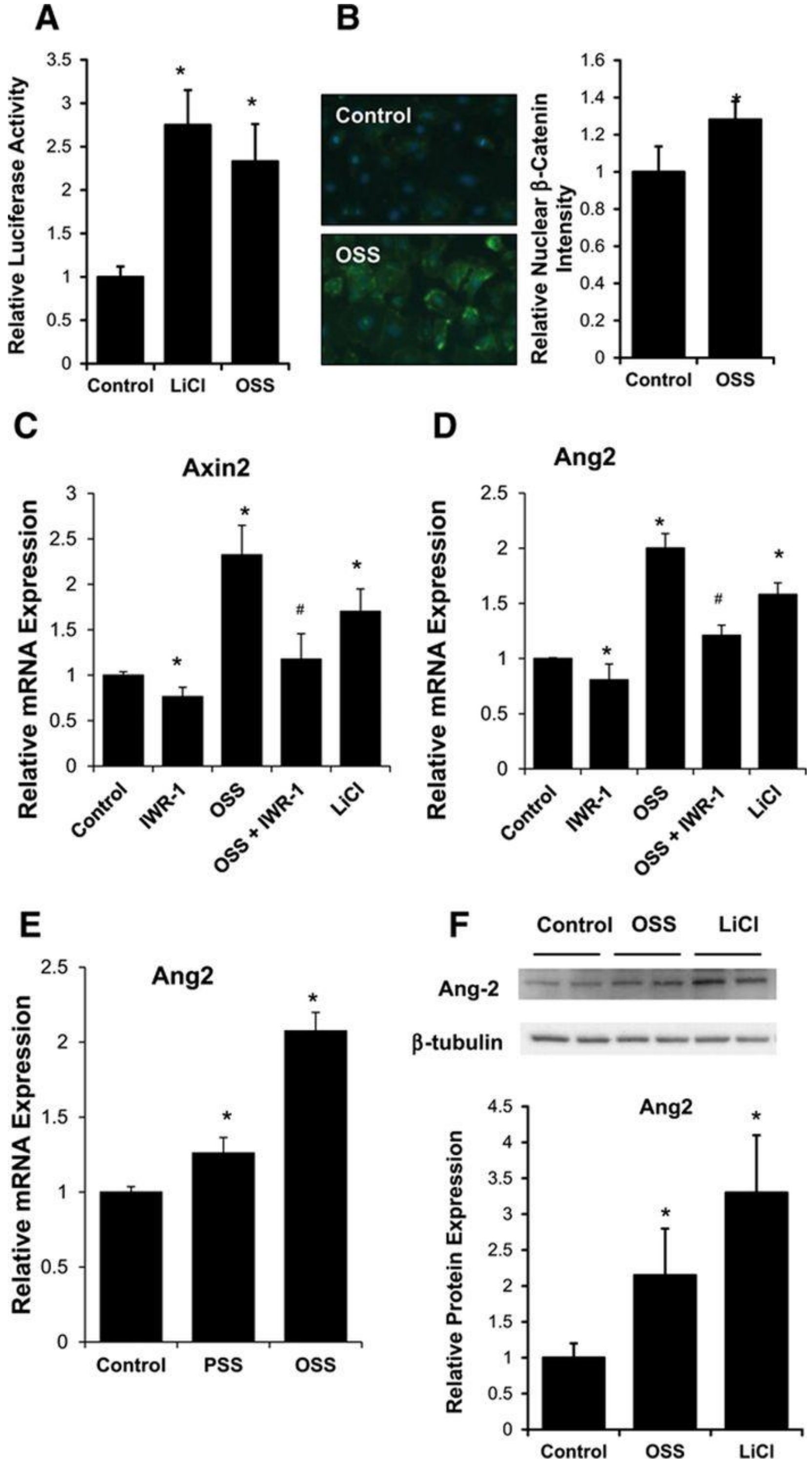

Figure 1. Oscillatory shear stress (OSS) promoted Ang-2 expression via Wnt signaling.

(A) Topflash reporter assay revealed that OSS for 8 hours significantly activated Wnt signaling. LiCl, a wnt-signaling inducer, was used as positive control (Control=1.00±0.06; LiCl=2.78±0.42; OSS=2.35±0.46; *$p<0.05$ vs control; n=4). **(B)** OSS induced a 1.3-fold increase in nuclear β-catenin fluorescence in canonical Wnt signaling pathway (*P<0.05; n=4). **(C)** OSS upregulated a well-recognized Wnt target gene, Axin-2, which was attenuated in the presence of IWR-1, a Wnt inhibitor (normalized to GAPDH: control=1.00±0.038; IWR-1=0.76±0.10; LiCl=1.70±0.25; OSS=2.32±0.32; OSS+IWR-1=1.18.±0.28; *P<0.05 vs control; #P<0.05 vs OSS; n=4). IWR downregulated but LiCl upregulated Axin-2 expression (*P<0.05 vs control; n=4). **(D)** OSS further upregulated Ang-2 mRNA expression, which was also attenuated in the presence of IWR-1 (normalized to GAPDH: control=1.00±0.01; IWR-1=0.81±0.14; LiCl=1.58.±0.10; OSS=2.00±0.13; OSS+IWR-1=1.21±0.09; *P<0.05 vs control; $^{\#}p<0.05$ vs OSS; n=4). IWR downregulated but LiCl upregulated Ang-2 expression (*$p<0.05$ vs control; n=4). **(E)** Pulsatile shear stress (PSS) upregulated Ang-2 mRNA expression by 1.21.±0.10-fold (*$p<0.05$ vs control; n=4), whereas OSS upregulated Ang-2 expression by 2.08±0.12-fold (normalized to GAPDH: *$p<0.05$ vs control; n=4). **(F)** In corollary, both OSS (24 hours) and LiCl significantly upregulated Ang-2 protein expression as quantified by densitometry (normalized to β-tubulin: *$p<0.05$ vs control; n=4).

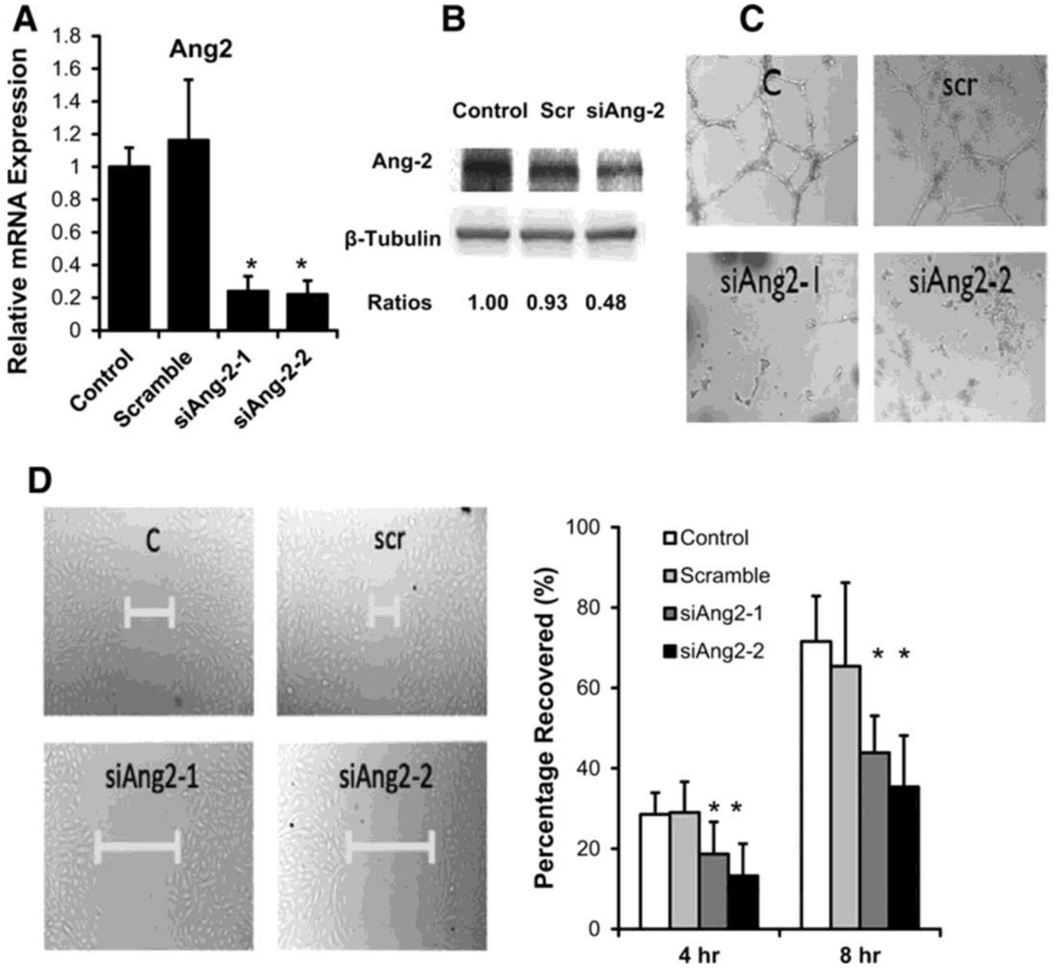

Figure 2. Knockdown of angiopoeitin-2 retarded human aortic endothelial cell (HAEC) migration and tube formation.

HAEC were transfected with 50 nmol/L scrambled siRNA (Scr), or in-house designed or independently designed Ang-2 siRNA (siAng2-1 and siAng2-2, respectively) for 48 hours. The cells were used for Ang-2 mRNA expression, Matrigel assay for tube formation, and scratch assay for cell migration. **(A)** Transfection with siAng-2 significantly reduced Ang-2 mRNA expression (**p*<0.05; n=4) and **(B)** protein expression by >50%. **(C)** HAEC tube formation was inhibited at 8 hours after siAng-2 transfection. D, HAEC monolayers were scratched using pipette tips and cultured in the presence of Scr, siAng2-1, and siAng2-2 (50 nmol/L). siAng-2 also inhibited HAEC migration. Bar graphs quantified cell migrations in terms of percentage after scratching at 4 hours (*$p<0.05$; n=4) and 8 hours (*$p<0.05$; n=4). Both the migration studies and the Matrigel assays were representative of 4 independent experiments with reproducible findings.

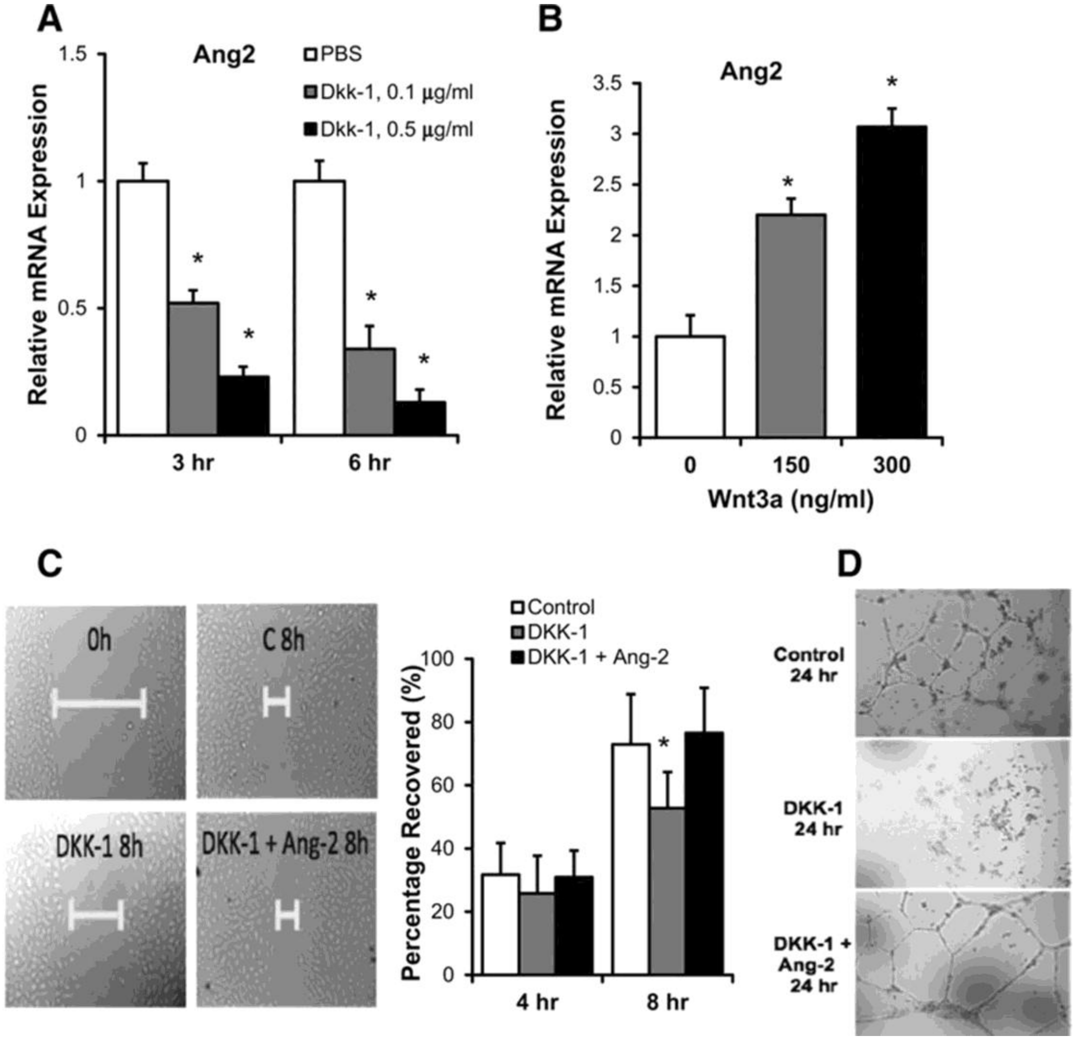

Figure 3. Wnt signaling mediated human aortic endothelial cell (HAEC) migration and tube formation is Ang-2-dependent.

(A) HAEC monolayers were treated with 0.1 and 0.5 µg/mL of DKK-1 for 3 and 6 hours, respectively. Quantitative reverse transcriptase-polymerase chain reaction revealed downregulation of Ang-2 mRNA expression in the presence of DKK-1 in a dose- and time-dependent manner (normalized to GAPDH: *p<0.05 vs control; n=3). **(B)** Ang-2 mRNA expression was upregulated in response to treatment with human recombinant Wnt3a for 3 hours (normalized to GAPDH: *p<0.05 vs control; n=3). **(C)** HAEC monolayers were scratched using pipette tips and cultured in the presence or absence of 0.5 µg/mL of human recombinant DKK-1. DKK-1 inhibited cell migration, which was rescued by recombinant Ang-2 treatment (0.5 µg/mL). Bar graphs quantified cell migrations in terms of percentage after scratching at 4 and 8 hours (*$p<0.05$; n=4). **(D)** HAEC were cultured in the Matrigel in the presence or absence of 0.5 µg/mL of DKK-1. After 8 hours, tube formation was inhibited in the presence of DKK-1 (0.5 µg/mL), which was rescued by Ang-2 treatment (0.5 µg/mL). Both the migration studies and the Matrigel assays were representative of 4 independent experiments with reproducible findings.

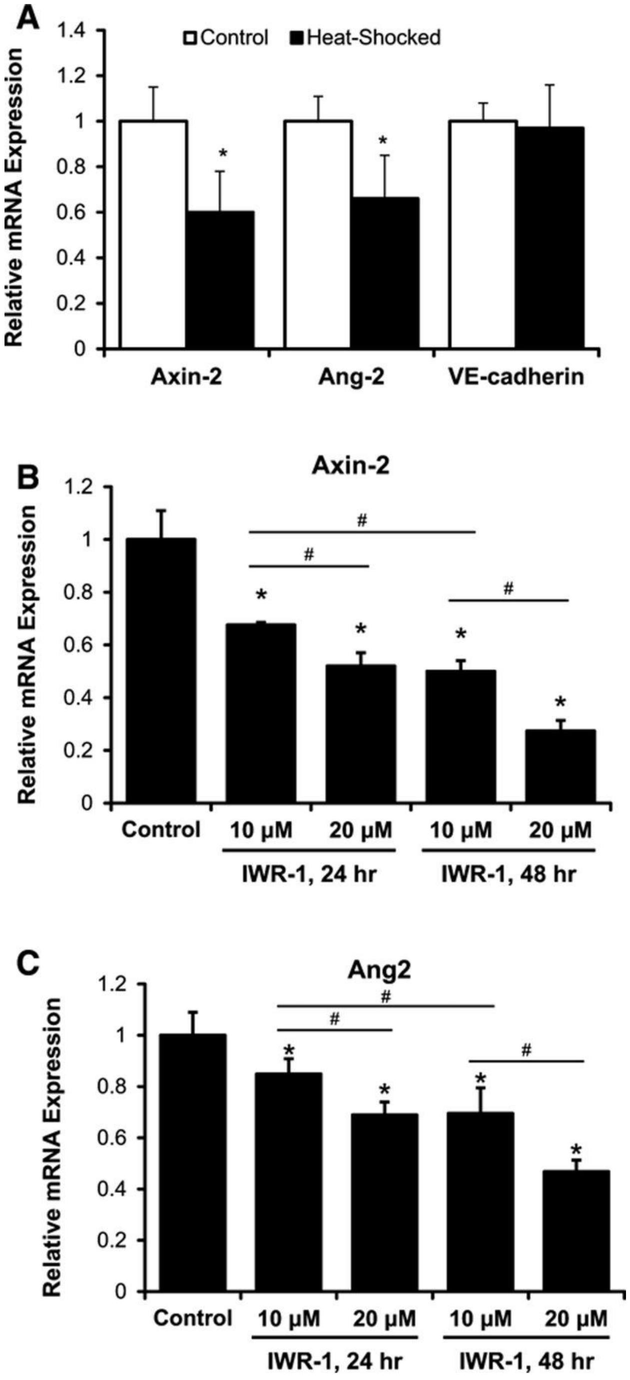

Figure 4. Treatment of *Tg(hsp70:DKK-1-GFP)* zebrafish embryos with IWR-1 recapitulated Ang-2 as a Wnt target gene.

(A) *Tg(hsp70l:Dkk1-GFP)* embryos were heat-shocked at 48 hours post fertilization (hpf) at 37°C for 1 hour. Axin-2, a well-recognized Wnt target gene, was used as a reference control. In Tg(hsp70l:Dkk1-GFP) embryos, both Axin-2 and Ang-2 mRNA expressions were downregulated in response to heat-shock induction of DKK-1 (*$p<0.05$ vs control; n=4). DKK-1 did not significantly change the expression of VE-Cadherin, suggesting DKK-1–induced downregulation of Axin-2 and Ang-2 was not because of potential vascular toxicity by heat-shock induction of DKK-1. B and C, IWR-1 also downregulated both Axin-2 and Ang-2 mRNA in a dose-dependent manner in the *Tg(kdrl:GFP)* fish at 72 hpf. Ang-2 expression was downregulated to a greater extent >48 hours treatment (starting at 24 hpf) when compared with 24-hour treatment (starting at 48 hpf; *$p<0.05$ vs control; $^{\#}p<0.05$ for pair-wise comparison; n=4).

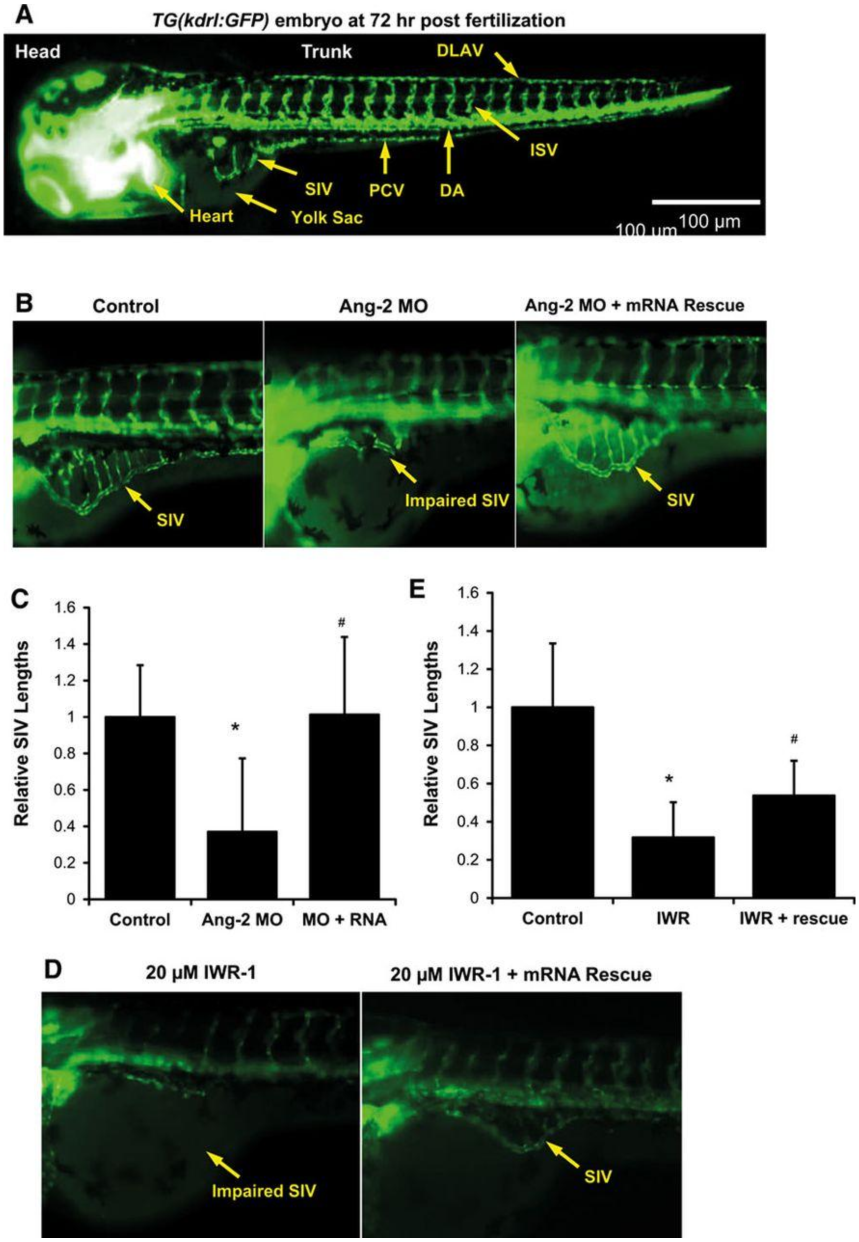

Figure 5. Ang-2 morphant injection impaired subintestinal vein (SIV) formation in Zebrafish embryos.

(**A**) Vasculature of transgenic zebrafish *Tg(kdrl:GFP)* at 72 hours post fertilization (hpf) reveals SIV, intersegmental vessel (ISV), dorsal longitudinal vein (DLAV), dorsal aorta (DA), and posterior cardinal vein (PCV). **(B)** Embryos injected with the control MO developed normal SIV at 72 hpf. Ang-2 ATG-MO injection (0.5 µmol/L) impairs SIV formation. Coinjection of zAng-2 mRNA (25 ng) with Ang-2 months rescued SIV formation. **(C)** Quantification of SIV length was performed and there was a significant difference between control and injection with morpholino (*$p<0.001$; n=20). zAng-2 mRNA injection rescued the SIV formation ($^{\#}p<0.001$; n=20). **(D)** Treatment with Wnt signaling inhibitor IWR-1 impaired SIV formation. Injection with zAng-2 mRNA (25 ng) was able to rescue SIV formation partially. **(E)** Quantification of SIV length showed significant reduction after IWR-1 treatment (*$p<0.001$; n=20), whereas injection with zAng-2 mRNA significantly increased SIV length ($^{\#}p<0.001$; n=20).

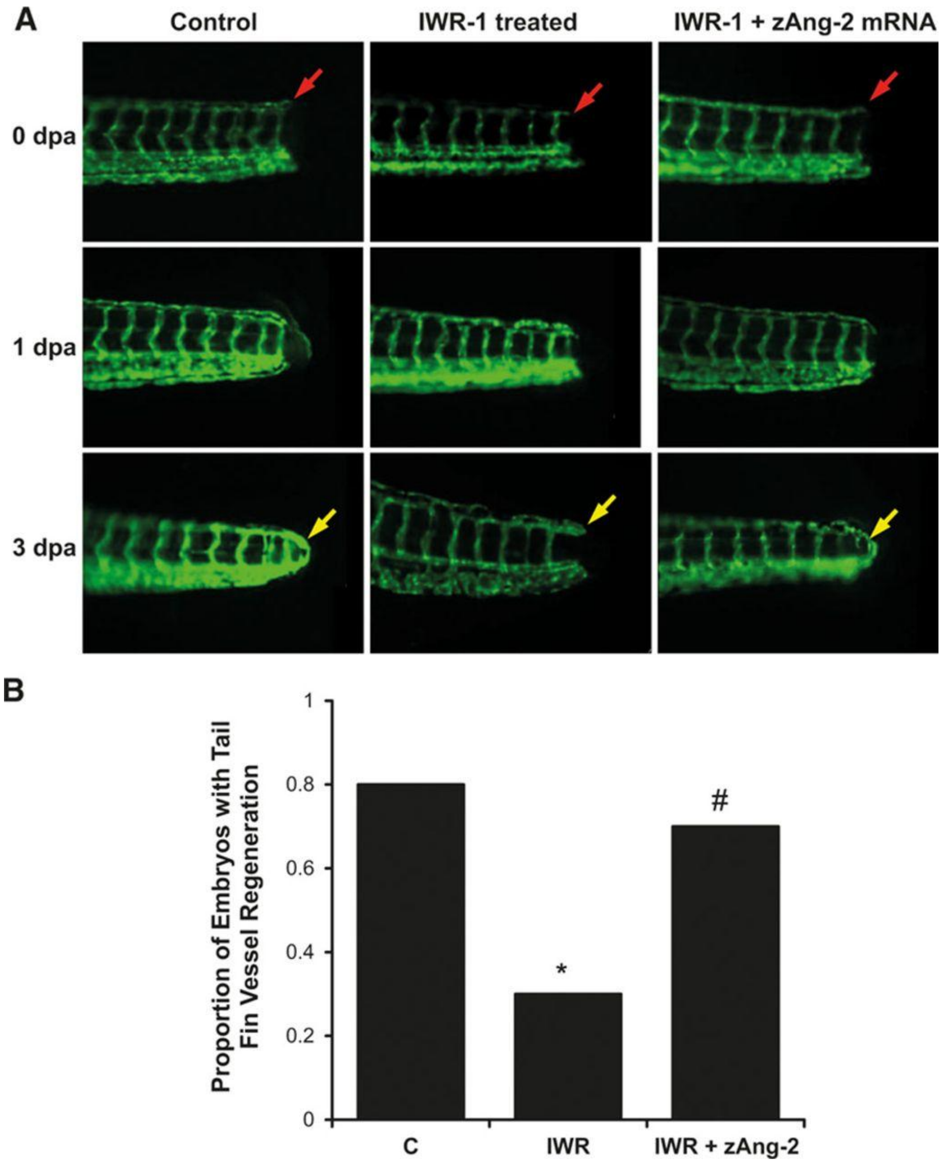

Figure 6. Wnt-Ang-2 signaling and vascular endothelial repair.

(A) The tails of transgenic *Tg(kdrl:GFP)* zebrafish embryos were amputated at 72 hours post fertilization. At 0 day post amputation (dpa), the red arrow pointed to the site of injury. At 1 dpa, initiation of endothelial repairs was present. At 3 dpa, complete tail repair was observed, as indicated by the yellow arrow. IWR-1 treatment (10 µmol/L) inhibited tail repair at 3 dpa. zAng-2 mRNA injection restored tail repair in IWR-1–

treated fishes at 3 dpa. **(B)** Quantification of tail repair. These experiments were repeated for n=20 in each treatment group, and each fish was assessed for the presence of tail repair at 3 dpa. The proportion of fish exhibiting tail repair in each group showed a significant difference between the control and IWR-1 treatment conditions (*$p<0.01$; n=20) and between IWR-1 treatment with and without zAng-2 mRNA injection ($^{\#}p<0.05$; n=20).

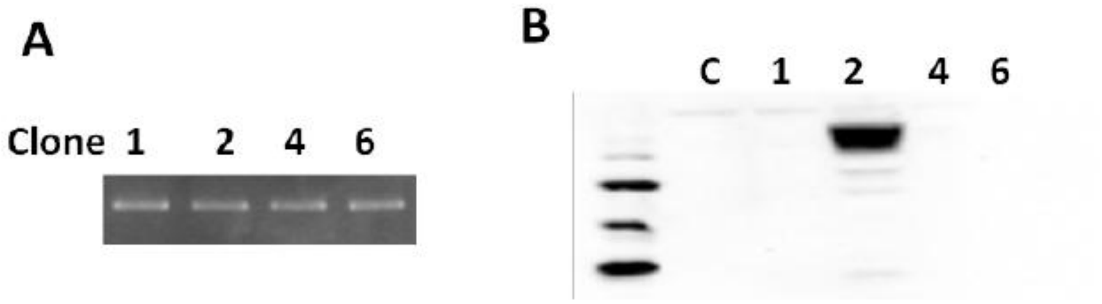

Supplemental Figure I. Verification of HA-tagged zAng2 expression.

(A) pCS2-zAng-HA plasmids were transfected into HEK-293 cells. RNA was isolated to verify zAng2-HA mRNA expression by qRT-PCR. **(B)** zAng2-HA protein expression was verified by Western blots using anti-HA antibody.

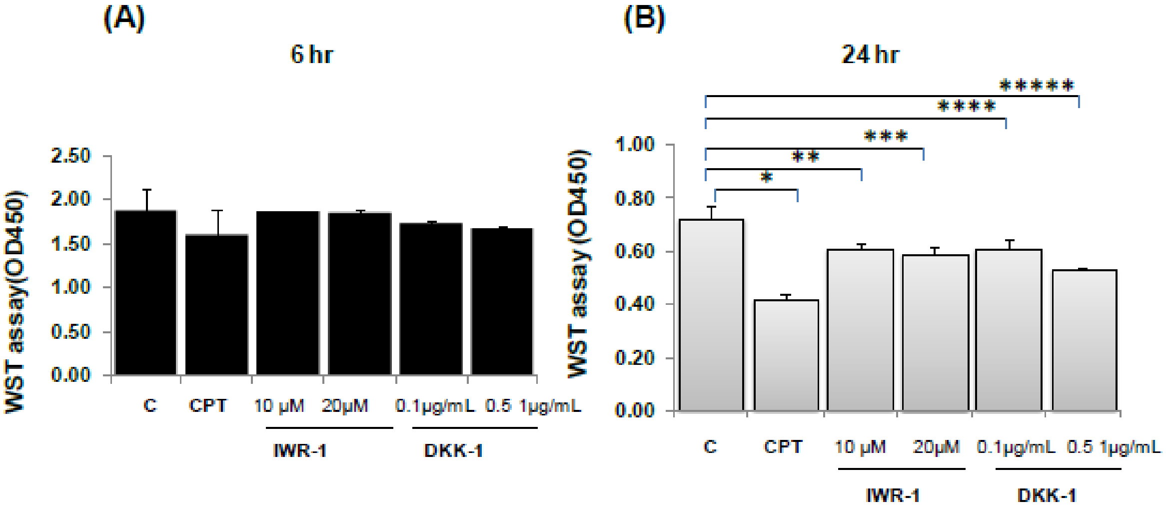

Supplemental Figure II. **Inhibition of Wnt signaling and cell viability**.

(**A**) After 6 hours of incubation, IWR-1 and DKK did not significantly reduce cell viability (p > 0.05 vs. control, n=3). (**B**) After 24 hours of incubation, both IWR-1 (at 10 μM and 20 μM) and Dkk-1 (at 0.1 μg/mL and 0.5 μg/mL) significantly reduced HAEC viability (*, **, ***, ****, *****p<0.05 vs. control, n=3). C denotes the control, CPT (Camptothecin) was used as a positive control for apoptosis.

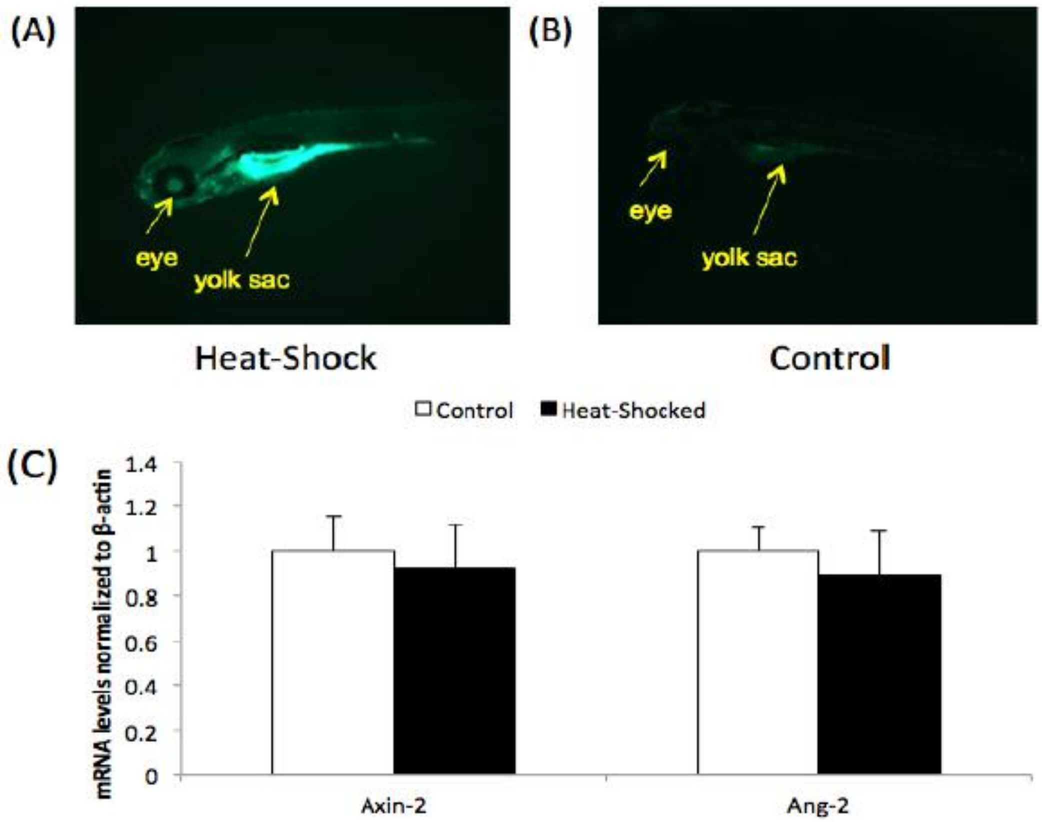

Supplemental Figure III. The effect of heat shock on non-transgenic fish on Axin2 and Ang-2 mRNA expression.

(A) Heat-shock induction of the *Tg(hsp70l:Dkk1-GFP)* embryos at 48 hpf at 37°C for 1 hour resulted in an increase in DKK-1-GFP expression. **(B)** In the absence of heat-shock induction, DKK-1-GFP was not expressed. **(C)** Heat-shock of non-transgenic (wild-type) fish showed no changes in Axin-2 or Ang-2 expression as compared to control ($p > 0.05$, n=3).

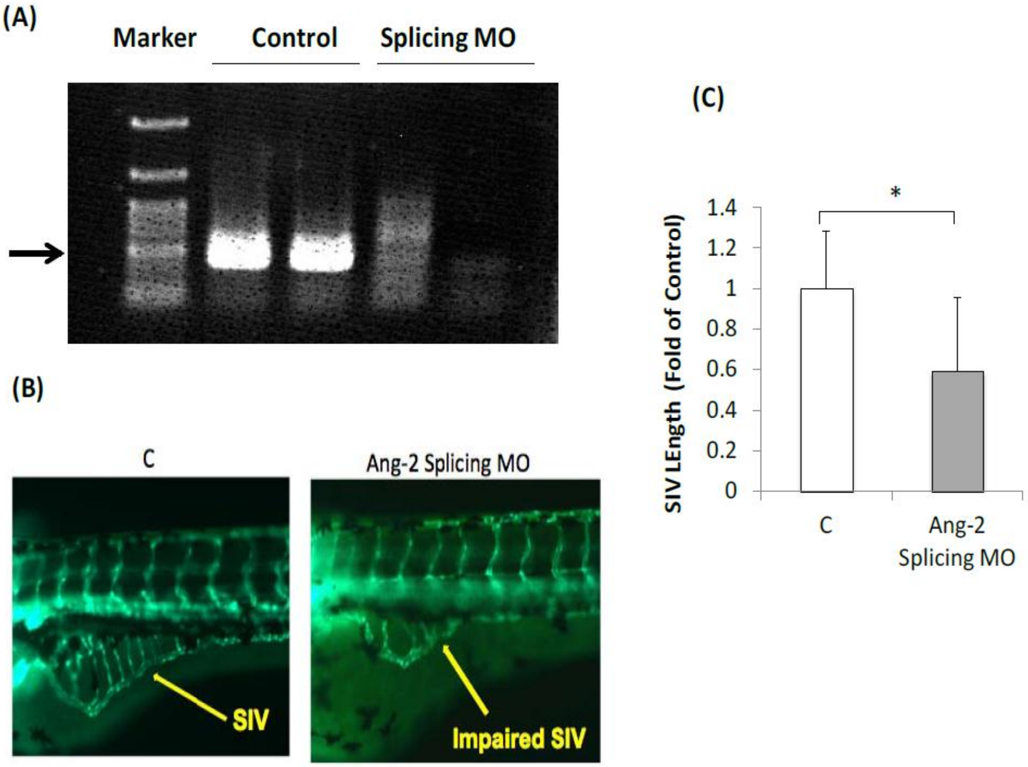

Supplemental Figure IV. zAng-2 splicing morpholino inhibited SIV formation.

(A) RT-PCR was performed to validate the effect of Ang-2 splicing MO using primers that covered the exon 2-intron 2 boundary of Ang-2 (Lamont RE1, Vu W, Carter AD, Serluca FC, MacRae CA, Childs SJ. **Hedgehog signaling via angiopoietin1 is required for developmental vascular stability**. Mech Dev. 2010 Apr;127(3-4):159-68). The splicing morpholino injection resulted in a decrease in the wild type band intensity (arrow) in comparison with the controls. **(B)** The splicing morpholino micro-injection into the 2-egg stage resulted in an impaired SIV formation at 72 hpf (representative photos). **(C)** Quantification of the SIV length revealed a 41% reduction in SIV length in response to Ang-2 splicing MO (* $p < 0.01$, n=20).

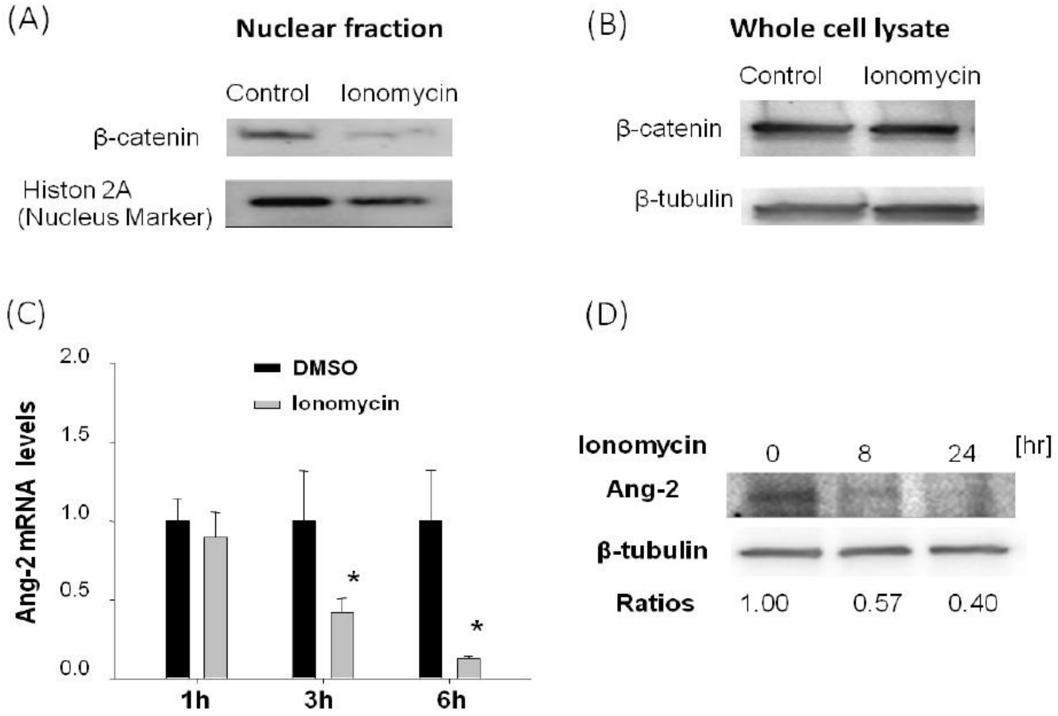

Supplemental Figure V. Ionomycin reduced Ang-2 expression by attenuating nuclear translocation of β-catenin.

(A) Ionomycin treatment at 5 μmol/L attenuated nuclear fraction of β-catenin in HUVEC. **(B)** Ionomycin treatment did not alter the overall β-catenin quantity in the whole cell lysate. **(C)** RNAs were isolated HUVEC that were treated with 5μmol/L of Ionomycin for 1h, 3h, and 6h, respectively. Ionomycin attenuated Ang-2 mRNA expression in HUVEC as normalized to GAPDH (**p* < 0.05 vs. Control cells with 0.1%DMSO treatment, n = 3). **(D)** Ionomycin attenuated Ang-2 protein levels. Entire cell lysates were collected by RIPA buffer and 50 μg of entire cell protein was prepared for Ang-2 protein levels. The relative expression was normalized to β-tubulin from density scan data. The blots were representative of two independent experiments with identical results.

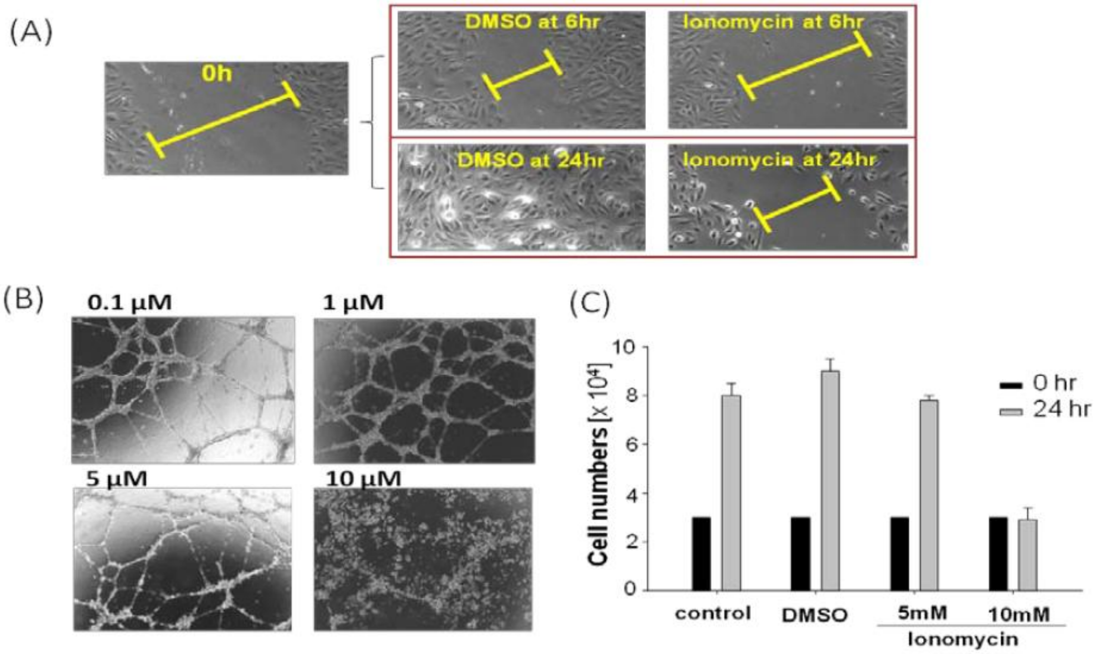

Supplemental Figure VI. Wnt signaling pathway influenced endothelial cell migration and tube formation via Angiopoietin-2.

(A) Ionomycin inhibited cell migration in HUVEC monolayer scratch assay. **(B)** HUVEC were cultured on the Matrigel in the presence of 0.1 – 10 μmol/L of Ionomycin for 8 hours. Ionomycin inhibited tube formation in a dose-dependent manner. **(C)** HUVEC were seeded in the 6-well plates and cultured for 24 hours in the presence or absence of Ionomycin at the indicated concentration, and were then trypsinized and counted with hemocytometer. HUVEC treated with the high concentration of Ionomycin ceased to proliferate.

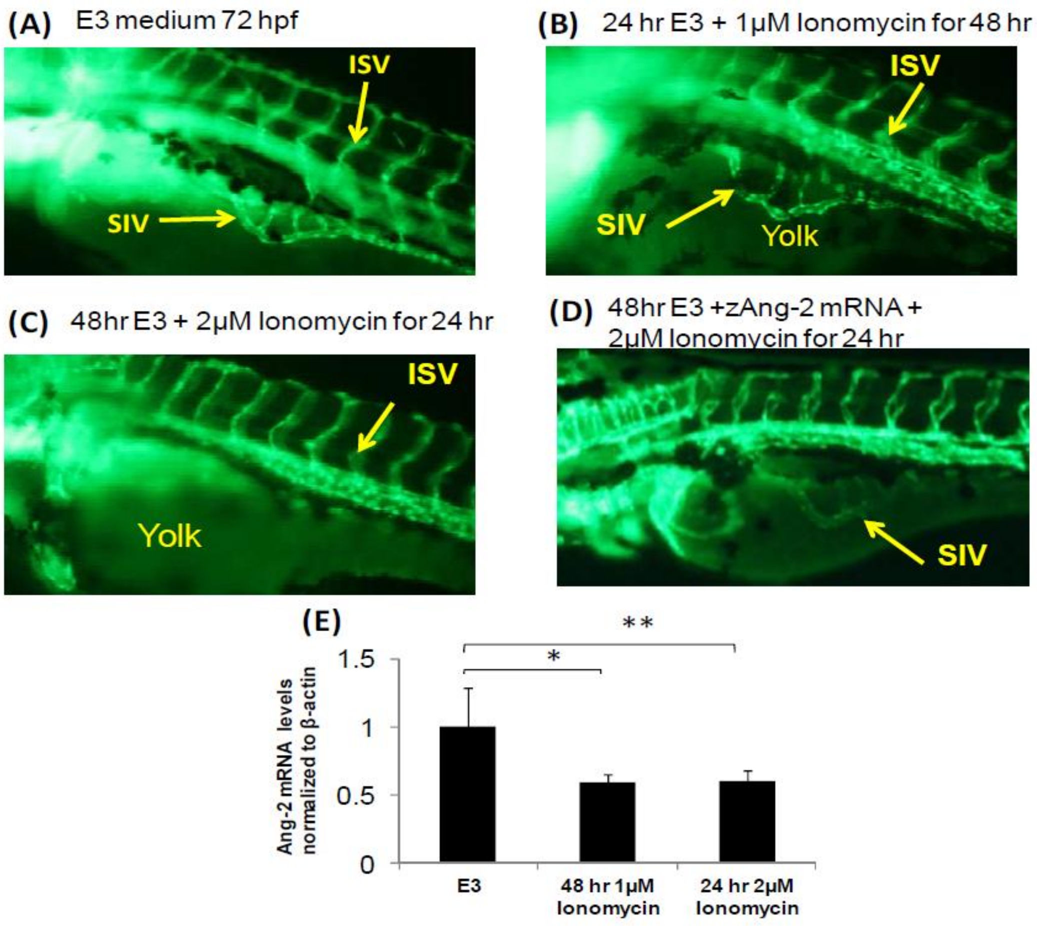

Supplemental Figure VII. Ionomycin impaired SIV formation that was rescued by Ang-2.

(**A**) Presence of SIV at 72 hpf in E3 medium. (**B**) 1μM Ionomycin starting at 24 hpf disrupted SIV formation, or (**C**) 2μM Ionomycin starting at 48 hpf inhibited SIV formation. (**D**) Micro-injection of 9 ng zAng-2 mRNA at the two-cell stage rescued SIV formation in the presence of 2μM Ionomycin. (**E**) qRT-PCR revealed that treatment at 48 hpf with 2 μM Ionomycin for 24 hr significantly down-regulated Ang-2 expression (**p* < 0.01 vs. E3; ***p* <0.01 vs. E3, n=3).

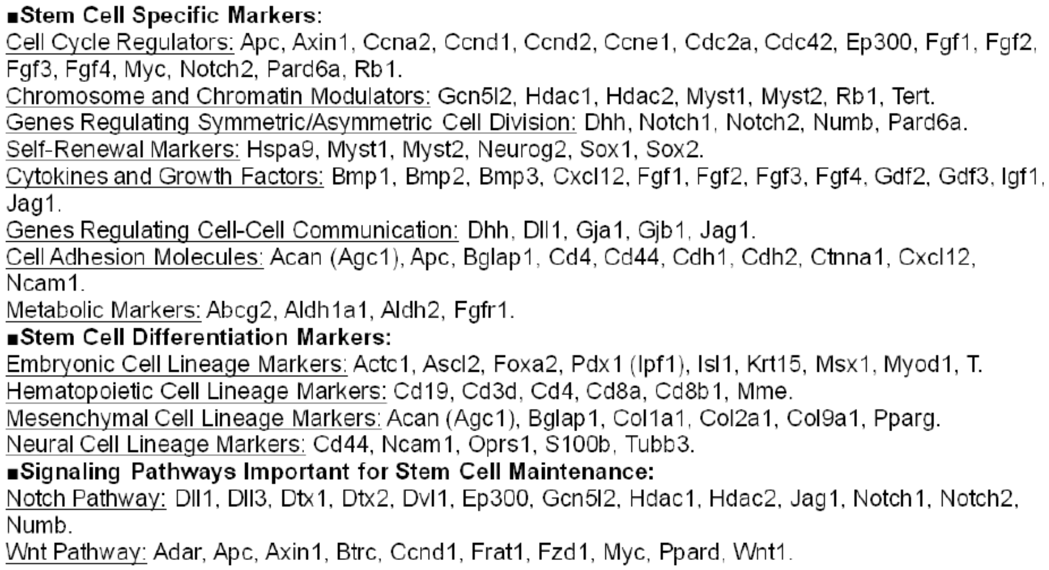

■Stem Cell Specific Markers:
Cell Cycle Regulators: Apc, Axin1, Ccna2, Ccnd1, Ccnd2, Ccne1, Cdc2a, Cdc42, Ep300, Fgf1, Fgf2, Fgf3, Fgf4, Myc, Notch2, Pard6a, Rb1.
Chromosome and Chromatin Modulators: Gcn5l2, Hdac1, Hdac2, Myst1, Myst2, Rb1, Tert.
Genes Regulating Symmetric/Asymmetric Cell Division: Dhh, Notch1, Notch2, Numb, Pard6a.
Self-Renewal Markers: Hspa9, Myst1, Myst2, Neurog2, Sox1, Sox2.
Cytokines and Growth Factors: Bmp1, Bmp2, Bmp3, Cxcl12, Fgf1, Fgf2, Fgf3, Fgf4, Gdf2, Gdf3, Igf1, Jag1.
Genes Regulating Cell-Cell Communication: Dhh, Dll1, Gja1, Gjb1, Jag1.
Cell Adhesion Molecules: Acan (Agc1), Apc, Bglap1, Cd4, Cd44, Cdh1, Cdh2, Ctnna1, Cxcl12, Ncam1.
Metabolic Markers: Abcg2, Aldh1a1, Aldh2, Fgfr1.
■Stem Cell Differentiation Markers:
Embryonic Cell Lineage Markers: Actc1, Ascl2, Foxa2, Pdx1 (Ipf1), Isl1, Krt15, Msx1, Myod1, T.
Hematopoietic Cell Lineage Markers: Cd19, Cd3d, Cd4, Cd8a, Cd8b1, Mme.
Mesenchymal Cell Lineage Markers: Acan (Agc1), Bglap1, Col1a1, Col2a1, Col9a1, Pparg.
Neural Cell Lineage Markers: Cd44, Ncam1, Oprs1, S100b, Tubb3.
■Signaling Pathways Important for Stem Cell Maintenance:
Notch Pathway: Dll1, Dll3, Dtx1, Dtx2, Dvl1, Ep300, Gcn5l2, Hdac1, Hdac2, Jag1, Notch1, Notch2, Numb.
Wnt Pathway: Adar, Apc, Axin1, Btrc, Ccnd1, Frat1, Fzd1, Myc, Ppard, Wnt1.

Supplemental Table I. List of genes in the Stem Cell RT^2 Profiler^{TM} PCR Array (SuperArray®).

Stem-cell specific markers, stem cell differentiation markers, and genes in signaling pathways important for stem cells maintenance were analyzed using qRT-PCR array. We analyzed expression of a focused panel of genes related to stem cell biology in response to fluid shear stress. Bioinforamtics approaches were based on the above functional gene groupings. Based on the initial grouping of the genes into different categories, we have first identified gene subsets in the Wnt pathway whose gene expression levels were significantly elevated at specific time points in response to shear stress. In the Wnt pathway, genes cooperate with each other to perform certain functions. Thus, the expression levels of genes in the Wnt pathway were highly correlated.

[Supplemental Videos Available Online]

Supplemental Video I: Micro-injection with the control MO displayed a normal blood circulation in dorsal aorta (DA), posterior cardinal vein (PCV), and subintestinal vein (SIV) at 72 hpf.

Supplemental Video II: Micro-injection with Ang-2 MO (0.5uM) led to absence of circulation despite cardiac contraction at 72 hpf.

Supplemental Video III: *Tg(hsp70l:DKK1-GFP)* fish were imaged for blood flow at 72hpf without heat-shock **(A)** or after validating DKK1-GFP expression following one hour heat-shock at 48 hpf **(B)**. DKK-1 did not have apparent effect on blood flow.

Chapter Three: Dynamics of Endothelial Metabolomics to Promote Vascular Repair

3.1 Introduction

Atherosclerosis is a systemic disease; however, its manifestations tend to be focal and eccentric [35, 48, 50, 89, 179-183]. While the spatial ($\partial\tau/\partial x$) and temporal ($\partial\tau/\partial t$) components of shear stress largely determine the focal nature of vascular oxidative stress and pro-inflammatory states, the emergent mechano-sensitive metabolic pathways provide new insights into the dynamic production of metabolites to maintain cellular homeostasis [54, 55]. [56]. Recently identified metabolites; namely, polyamines such as spermine for acute stroke, cinnamoylglycine, nicotinamide, and cysteine-glutathione disulfide for kidney cancer, and 3-hydroxykynurenine and oxidized glutathione for Parkinson disease, have further led to new biomarkers and therapeutic targets [59-61]. In this context, elucidating mechano-signal transduction underlying metabolomic pathways paves the way to study cellular homeostasis [62, 63], migration [64], and vascular development [36].

Fluid shear stress imparts mechano-signal transduction to promote differentiation of embryonic stem cells to vascular progenitors in angiogenesis [29-31] [184] [185, 186]. While VEGF-mediated angiogenesis has been extensively studied in cancer treatment [187, 188], shear stress-responsive VEGF signaling and metabolite production have been poorly understood in vascular angiogenesis and vascular repair [189-191] [192]. The metabolomic profile of the endothelium is unique in that despite having immediate access to oxygen in the blood, endothelial cells generate more than 80% of their ATP via the glycolytic pathway [65]. This is advantageous in the instance of vascularizing avascular tissues through sprouting, where endothelial cells are entering oxygen-depleted tissue [36]. Endothelial cells are resistant to hypoxia in the presence of glucose, but become oxygen-sensitive in a low-glucose environment [66]. Additionally, low-oxidative metabolism generates fewer reactive oxygen species and less oxidative stress in a high-oxygen environment [36] Endothelial cells can rapidly switch from a long-term quiescent state to active growth in response to hypoxia or growth factors[36]. As they switch from quiescence to proliferation and migration, endothelial cells increase their glycolytic flux [67].

In addition to environmental factors, endothelial glycolsyis is subject to numerous hemodynamic forces [68]. Laminar shear stress activated Krüppel-like factor 2(KLF2) to suppress 6-phosphofructo-2-kinase/fructose-2,6-biphosphatase 3 (PFKFB3)-mediated glycolysis to mitigate angiogenesis and vessel sprouting [67, 69]. Shear-activated eNOS produces nitric oxide (NO) [70, 71] to activate Protein Kinase C isoform epsilon (PKCε), which, in turn, attenuates production of mitochondrial reactive oxygen species (ROS) to confer cardioprotection via metabolism-related proteins in the setting of ischemia-reperfusion injury[29-32 [72] [73, 74] [75] [76]. Additionally, shear-responsive VEGF- and eNOS-signaling activates PKCε to modulate endothelial cell proliferation, lumen formation, and cellular homeostasis [77, 78]. [79]. However, the mechanotransduction underlying PKCε-mediated metabolomic pathways to promote angiogenesis and vascular repair remains elusive.

In this context, **we tested whether shear stress modulates endothelial metabolomics to promote vascular repair via PKCε-mediated glycolytic metabolites.** We observed that both pulsatile shear stress (PSS) and oscillatory shear stress (OSS) significantly increased endothelial glycolytic metabolites; namely, xylitol and dihydroxyacetone, but decreased gluconeogenic metabolites metabolites; namely, aspartic acid. Both PSS and OSS up-regulated PKCε expression and activity via VEGF receptor, and constitutively active PKCε increased basal glycolysis activity, implicating that shear stress-responsive PKCε modulates glycolysis. To recapitulate vascular repair in transgenic *Tg(flk1:GFP)* zebrafish embryos, we decreased viscosity and fluid shear stress by performing micro-injection of *GATA-1a* morpholino oligonucleotide (MO) to inhibit hematopoeisis. *GATA-1* MO impaired and delayed vascular repair in response to tail amputation. Co-injection of PKCε mRNA with *GATA-1a* MO rescued tail repair. Injection of epo mRNA to increase viscosity resulted in increased tail repair. By analyzing shear-responsive endothelial metabolomics, we gain new insights into shear stress-responsive VEGFR- PKCε signaling to modulate glycolytic metabolites to influence vascular repair.

3.2 Materials and Methods

3.2.1 Vascular Endothelial Cell Culture

Human aortic endothelial cells (HAEC) were purchased from Cell Applications and cultured in endothelial growth medium (Cell Applications) supplemented with 5% Fetal Bovine Serum (FBS) (Gibco). HAEC were propagated for experiments between passages 5 and 10. HUVEC were purchased from Cell Applications and cultured in Dulbecco's Modified Eagle Medium (DMEM) (Gibco) supplemented with 5% FBS. HUVEC were propagated for experiments between passages 4 and 8.

3.2.2 Dynamic Flow System to Interrogate Vascular Endothelial Cells

A dynamic flow system was used to generate well-defined pulsatile (PSS) and oscillatory (OSS) shear stress as previously described [193]. The flow system was designed to simulate physiologic shear stress occurring at human arterial branching points with well-defined slew rates, time-averaged shear stress, frequency, and amplitude. DMEM culture media supplemented with 1% FBS was maintained at a temperature of 37°C and pH of 7.4. Confluent monolayers of HAEC grown on glass slides were subjected to three flow conditions at 1 Hz for 4 hours: 1) Static control at no flow state, 2) Pulsatile flow with time-averaged shear stress of 23 dyne/cm^2 accompanied by a stress slew rate ($\partial\tau/\partial t = 71$ dyne $\cdot$ cm^{-2} $\cdot$ s^{-1}), and 3) Oscillating flow (0.1 ± 4 dyn cm^2).

3.2.3 Metabolomic Analysis

Metabolite samples were collected from HAEC exposed to PSS, OSS, or static conditions for 4 hours. Cells were trypsinized, fixed in 4% PFA, and immediately stored at -80°C prior to shipment over dry ice to the West Coast Metabolomics Center at UC Davis. GC-TOF analysis was performed at the West Coast Metabolomics Center, as untargeted analysis on primary metabolism.

3.2.4 SeaHorse Mitochondrial Function Analysis

HAEC were exposed to either CA-AdvPKCε or DN-AdvPKCε, followed by treatment with 50 uM H_2O_2 or control DMEM + 1% FBS. Mitochondrial function was analyzed using the Seahorse XF analyzer system as described with a 24-well assay plate format [194]. Glycolysis levels were determined through measurements of the extracellular acidification rate [195].

3.2.5 AE-PKCε Mouse Model of Ischemia-Reperfusion Injury

Animals used in the study were PKCε transgenic mice generated using a cDNA of active PKCε driven by the α-myosin heavy chain promoter to achieve cardiac-specific expression [76, 196, 197]. AE PKCε transgenic mice express a PKCε molecule that favors the open and active conformation whereas DN PKCε mice express a dominant negative form of the same molecule. Metabolite extracts were prepared from murine hearts as described previously [76]. Proton magnetic resonance spectroscopy (1H-NMR) was performed as described online [198].

3.2.6 Chemical Reagents

Human recombinant Vascular Endothelial Growth Factor (VEGF) was purchased from Fisher Scientific and dissolved in PBS. Cediranib was purchased from SelleckChem and dissolved in DMSO.

3.2.7 Quantitative Real-Time PCR Analysis

Protein Kinase C isoform epsilon (PKCε) mRNA expression was measured by quantitative RT-PCR. Total RNA was isolated using Aurum Total RNA Mini Kit (Bio-Rad). RNA was reverse-transcribed using iScript cDNA synthesis kit (Bio-Rad), followed by PCR amplification with iScript RT-PCR Kit with SYBR Green (Bio-Rad). The expression levels were normalized to actin.

The forward primer sequence for PKCε was 5'- GAG CCG CCA CTT CGA GGA CTG -3' and the reverse primer was 5'- TTG TGG CCG TTG ACC TGA TGG -3'. The forward primer sequence for Actin was 5'- ACC CAC ACT GTG CCC ATC TAC -3' and the reverse primer was 5'- TCG GTG AGG ATC TTC ATG AGG -3'. The forward primer sequence for PFKFB3 was 5' – GGA GGC TGT GAA GCA GTA CA – 3' and the reverse primer was 5' – CAG CTA AGG CAC ATT GCT TC – 3'. The differences in C_T values for various intervals versus control were used to determine the relative difference in the levels of PKCε mRNA expression.

3.2.8 Adenoviral Vectors

Human constitutively active PKCε and dominant-negative PKCε adenoviruses were generously provided by Dr. Allen Samarel at the Loyola University Medical Center and Dr. Peipei Ping at the University of California Los Angeles. The technique used for PKCε adenovirus was described previously [199].

3.2.9 Western Blot Analysis

Cells were harvested, washed with phosphate-buffered saline and lysed with RIPA buffer. The lysate was centrifuged at 12,000g for 10 minutes, and the resulting supernatants were used as the entire cell lysate. Proteins were separated by 4–20% polyacrylamide gel with SDS and electroblotted onto the polyvinylidene difluoride membranes (GE Healthcare, Buckinghamshire, UK) and were blocked overnight at 4°C in Tris buffered saline-Tween20 (TBS-T) containing 5% non-fat dry milk (BioRad laboratory, CA). PKCε protein expression was detected with anti-PKCε (Santa Cruz Biotech), and equal loading was verified by blotting with anti-β-tubulin (Millipore Inc). After treatment with peroxidase-conjugated anti-goat (Santa Cruz) or anti-mouse IgG antibody (Jackson ImmunoResearch, PA) for 1 hour at room temperature, chemilluminescence signal was developed with Supersignal Western Pico (Pierce) and recorded with FluorChem FC2 (Alpha Inotech Inc, San Leandro, CA). Antibodies against autophagy-associated genes were purchased from Abcam for LC3 and from Boster Biological Technologies for p62. Parallel blots were performed with anti-b-tubulin (Millipore, Inc.) for loading normalization. Densitometry was performed to quantify blot bands as previously described [200].

3.2.10 *Tg(flk-1:EGFP)* Transgenic Zebrafish Model to Study Vascular Injury and Repair

Tg(flk-1:EGFP) Transgenic zebrafish embryos were generously provided by Prof. Ellen C. Lien (Children's Hospital Los Angeles, Los Angeles, CA) for assessing vascular injury and repair in response to tail amputation. Flk-1, VEGF receptor 1, is tissue-specific for vascular endothelial cells. Fish embryos were injected with either a PKCε morpholino (MO) or a control nonsense MO. Injection was validated by qRT-PCR analysis of PKCε gene expression. The following MO sequences were used. Standard Control negative MO: 5'- CCT CTT ACC TCA GTT ACA ATT TAT A-3'; Zebrafish *p53* apoptosis suppression MO (p53MO): 5'- GCG CCA TTG CTT TGC AAG AAT TG -3'; *PKCε* splice MO: 5'- CTC CAT TAA AAA CCA CCA TGA TGA C -3'; *Gata-1a* MO: 5'- CTGCAAGTGTAGTATTGAAGATGTC-3'; *Tnnt2a* MO: (5'- CGCGTGGACAGATTCAAGAGCCCTC-3'. MOs were dissolved in water to make 0.3mM stock solution with addition of 0.1mM p53 MO. Immediately after collection at 0 hpf, approximately 30-40 embryos were randomly chosen for micro-injections. All of the embryos were maintained in E3 medium at 28˚C.

Injected fish larvae were grown to 72 hpf in standard E3 medium, followed by amputation of the posterior tail segment by ~100 µm from the tip of the tail. The larvae were anesthetized in 0.02% tricaine solution to allow for precise placement. Amputation was performed with a surgical scalpel under a stereo microscope (MEIJI Techno EMZ series, MEIJI, Japan) for both control and treatment groups. After amputation, fish were separated to allow for same-fish control. Fish tail sections were imaged (Olympus IX71, Olympus, Japan) to visualize the blood vessels immediately after amputation and every 24 hours thereafter over the next 3 days. Regeneration of blood vessels was compared between the different treatment groups at 0 day post amputation (dpa), 1 dpa, and 3 dpa.

3.2.11 Cloning of PKCε RNA for Rescue

Mouse PKCε cDNA was amplified from a donor plasmid (purchased from Addgene) and cloned into the plasmid pCS2+ at the BamH I and EcoR I sites. Clones with the PKCε cDNA insert were selected by PCR screening. The pCS2+PKCε plasmid was verified by transfecting the plasmids into HEK-293 cells, followed by detecting PKCε protein expression by Western blot with anti-PKCε antibody (**Supplemental Figure)**. mRNA was synthesized from the cloned plasmid using the mMessage SP6 kit (Invitrogen, CA). Transcribed PKCε mRNA was purified with the total RNA isolation kit (Bio-Rad) for *in vivo* rescue experiments.

3.2.12 siRNA Transfection

siRNA Transfection was performed with Lipofectamine RNAiMax (Invitrogen). HAEC were plated in 6 well plates or standard glass slides on the day prior to transfection. The cells were transfected with 50 nM PKCε or KDR siRNA (Qiagen). Transfection media were changed to normal growth media after 4 hours of transfection. Cells were used for confirmation of gene knockdown or assay at 48 hours after transfection.

3.2.13 *In-Vitro* Tube Formation Assay

HUVEC cells were grown in a 96-well plate at 20,000 cells/well on a 100 µL Matrigel Growth-factor-reduced matrix (BD Biosciences) that was allowed to solidify before seeding cells in DMEM + 5% FBS + 25 ng/mL VEGF. Tube growth was allowed for six hours, and wells were imaged to visualize tube formation with a microscope

(Olympus). Images were analyzed using S.CORE image analysis, with tube formation index (TFI) representing a quantification of the images.

3.2.14 Mitochondrial Superoxide Assay

Mitochondrial superoxide ($mtO_2^{\cdot -}$) was analyzed both quantitatively by flow cytometry and qualitatively by fluorescent imaging. In a 6-well format for FACS analysis, cells were incubated with 10 μM mitoSOX dye (Invitrogen) for 15 minutes, then lysed and rinsed three times with PBS buffer to remove residual dye. Samples were then analyzed using FACS analysis, with gating to remove debris or clusters.

For qualitative imaging of $mtO_2^{\cdot -}$ levels during tube formation, tube formation assay was performed as described above, with media that was absent of phenol red. At 6 hr, cells were incubated with 10 μM mitoSOX dye for 30 minutes, rinsed three times with DPBS, and then fixed with PFA. Cells were imaged using fluorescent microscopy.

3.2.15 Statistical Analysis

Data were expressed as mean ± SD and compared among separate experiments. Comparisons of multiple values were made by one-way analysis of variance (ANOVA), and statistical significance for pairwise comparison was determined by using the Tukey test. *P*-values of < 0.05 were considered statistically significant.

3.3 Results

3.3.1 Metabolomic Analysis in Response to Pulsatile and Oscillatory Shear Stress

HAEC in response to PSS, OSS, and static conditions were analyzed by Gas chromatography time-of-flight mass spectrometry (GC-TOF) to assess the production of 156 distinct metabolites. Six statistically significant metabolites; namely, xylitol, methionine sulfoxide, lyxitol, erythrose, dihydroxyacetone, and aspartic acid, were up-regulated ($p < 0.01$, n= 6) by both PSS and OSS. In response to PSS and OSS, these six metabolites were sufficiently separated by the Principal component analysis (PCA) (**Fig. 1a, 1b**).

PSS increased glycolysis-related metabolites, xylitol and dihydroxyacetone, by 2.36 and 2.29-fold, respectively, and reduced aspartic acid by 3.57-fold. Similarly, OSS induced 1.62 and 2.55-fold increases for the same glycolytic metabolites, and a 1.69-fold decrease for aspartic acid (**Fig. 1c**). PSS additionally significantly increased intracellular glucose, fructose-6-phosphate, and fructose-1-phosphate.

3.3.2 Shear-Responsive PKCε Modulates Glycolytic Metabolites

PKCε-mediated glycolytic activity is hypothesized based on an observed increase in glycolysis-related metabolites; namely, alanine, glucose, and lactate, to confer cardiac protection in the setting of ischemia reperfusion injury in the active PKCε transgenic mouse model (**Fig. 1d**). Both PSS and OSS increased PKCε mRNA expression by 58% and 73%, respectively. Pre-treatment with Cediranib (10 μM), a VEGFR-inhibitor, attenuated shear stress-mediated PKCε expression (**Fig. 2a**). VEGF-dependent PKCε protein expressions were also increased by PSS and OSS by 38% and 42%, respectively, and these increases were attenuated by VEGFR-inhibitor (**Supplemental Fig. 1**). As a corollary, PKCε activity was increased in response to PSS and OSS by 60% and 80%, respectively (**Fig. 2b**).

To assess whether shear stress-activated PKCε modulates glycolysis, we analyzed endothelial metabolic activity using a SeaHorse Flux Analyzer. Treatment with constitutively active PKCε adenovirus (CA-AdvPKCε) increased basal (3.11-fold, *n*

= 4, $p < 0.01$) and maximum (2.52-fold, $n = 4$, $p < 0.01$) glycolytic flux compared to dominant negative control (DN-AdvPKCε). Elevated glycolytic flux was also observed in response to H_2O_2 (50 µM)-induced oxidative stress (2.13-fold basal, 2.45-fold maximum, $p < 0.01$, $n = 4$) (**Fig. 2d,e**). In the presence of H_2O_2, treatment with CA-AdvPKCε increased PFKFB3 mRNA expression compared to dominant negative control ($p < 0.05$, $n = 3$) (**Fig. 2f**). Pulsatile shear stress additionally increased PFKFB3 mRNA expression by 2.6-fold ($p < 0.01$, $n = 6$) (**Supplemental Figure 2**).

3.3.3 Vascular Repair is Dependent on Shear-Induced PKCε

To determine whether shear stress-responsive PKCε modulated vascular repair, we used transgenic *Tg(kdrl:EGFP)* zebrafish embryos (**Fig. 4a**). Embryos injected with control morpholino (MO) developed vascular repair as demonstrated by a closed loop between the dorsal longitudinal anastomotic vessels and dorsal aortas at 3 days post tail amputation (dpa) (**Fig. 3a, Fig. 4b, Supplemental Video 1**). *GATA-1a* MO injection inhibited hematopoeisis to reduce blood viscosity and shear stress, resulting in significant attenuation of tail repair at 3 dpa (**Fig. 3c,d, Fig. 4c, Supplemental Video 2**). Tail repair developed as hematopoeisis resumed at 6 dpf, and a closed loop was observed at 7 dpf (**Fig. 4c**). However, co-injection of PKCε mRNA with *GATA-1a* MO (**Fig. 4f**) rescued vessel repair at 3 dpa. As a corollary, treatment with PKCε MO to silence PKCε protein expression significantly mitigated tail repair at 5 dpf (**Fig. 5a**). Co-injection of PKCε mRNA with PKCε MO rescued tail repair (**Fig. 5a**). We further induced zero net blood-flow by using *TNNT-2* MO to inhibit cardiomyocyte contraction, and we recapitulated an impaired vascular repair similar to *GATA-1a* MO at 5 dpf (**Fig. 4d**). In the absence of cardiac contractile function, the *TNNT*-2 MO-injected embryos developed severe pericardial edema. Increasing erythrocyte production to raise blood viscosity and shear stress through injection with epo mRNA increased tail repair compared to control (**Fig. 3b,d, Fig. 4e, Supplemental Video 3**). Proportion of embryos exhibiting vessel repair at 5 dpf was quantified for statistical analysis (**Fig. 4g**). These findings support that PKCε is implicated in shear stress-modulated vascular repair.

3.3.4 PKCε-Dependent Glycolytic Pathway Modulates Vascular Repair

To further elucidate the role of PKCε underlying vessel repair, we employed an *in-vitro* Matrigel model of tube formation with human aortic endothelial cell (HAEC). Silencing PKCε with siRNA decreased tube formation by 40% as quantified by tube length compared to scrambled control (**Fig. 5b,c**). Over-expression of PKCε by CA-AdvPKCε adenovirus increased tube formation by 2.1-fold compared to a LacZ control adenovirus treatment (**Fig. 5b,c**). Tube formation was disrupted by treatment with 10 μM of VEGFR-inhibitor in HAEC transfected with a control LacZ virus (**Fig. 5b,d**), and restored in HAEC treated with constitutively active PKCε adenovirus (**Figs. 5b,d**). Treatment with glycolytic metabolites dihydroxyacetone and xylitol increased tube formation, while gluconeogenic metabolite aspartic acid inhibited tube formation under oxidative stress conditions (**Fig. 6a**). Treatment with pro-glycolytic metabolites xylitol, dihydroxyacetone, glucose, fructose-6-phosphate, and fructose-1-phosphate rescued tube formation *in-vitro* in the absence of PKCε (**Fig. 6b**). These data corroborates the role of PKCε-responsive metabolism in tube formation during vascular repair.

3.3.5 PKCε is Mito-Protective in Response to Oxidative Stress

To demonstrate the vascular protective role of PKCε in the setting of mitochondrial superoxide ($mtO_2^{\cdot -}$) production, we quantified MitoSOX fluorescence intensity via FACS analysis. HAEC tube formation was inhibited in response to H_2O_2 (200 μM), whereas over-expression of PKCε attenuated H_2O_2-mediated increase in $mtO_2^{\cdot -}$ production (**Fig. 7a,b**), and restored tube formation (**Fig. 7c**). Treatment with 100 μM H_2O_2 elevated MitoSOX fluorescent intensity during tube formation, whereas over-expression of PKCε normalized MitoSOX intensity (**Fig. 7d,e**), suggesting PKCε –mediated mitochondrial protecting. Taken together, shear stress-activated PKCε expression is implicated in promoting tube formation and decreasing $mtO_2^{\cdot -}$ production.

3.3.6 PKCε Activates Autophagy to Promote Tube Formation

In the setting of H_2O_2-mediated oxidative stress, inhibition of autophagy via bafilomycin treatment (to block the fusion of autophagosomes with lysosomes) or siATG5 transfection significantly attenuated tube formation relative to control (**Fig. 8a**). Inhibiting autophagy via bafilomycin significantly increased $mtO_2^{\cdot -}$ levels following 10 or 50 μM H_2O_2 treatment (**Fig. 8b**). In contrast, activation of autophagy via perifosine and SAHA promoted tube formation in the presence of H_2O_2-mediated oxidative stress (**Fig. 8a**). We observed a 60% increase in LC3-2/LC3-1 ratio in response to 50 μM H_2O_2 ($p < 0.01$, $n = 3$), and this increase was attenuated when HAEC were pre-treated with CA-AdvPKCε (**Fig. 8c**). P62 protein expression was decreased by 50% following treatment with CA-AdvPKCε relative to dominant negative virus, indicating that PKCε activity promotes glycolytic flux (**Fig. 8d**). These findings further indicate that shear stress-responsive PKCε promotes vascular repair via activation of autophagy to maintain mitochondrial homeostasis.

3.4 Discussion

In this study, we elucidate shear stress-activated endothelial metabolomics to modulate vascular repair. Building on the mechano-transduction mechanisms underlying shear stress and inflammatory responses [29-31, 33, 35, 87, 184-186, 201, 202], we provide a mechano-metabolic approach to uncover shear stress-sensitive PKCε signaling to modulate glycolytic metabolites and to recapitulate vascular repair in the *Tg(kdrl:EGFP)* model.

Biomechanical forces modulate vascular endothelial metabolic pathways to maintain cellular homeostasis [62, 63]. Our metabolomic analysis of HAEC responses to shear stress that occur in the athero-protective and –prone regions demonstrated up-regulations of glycolysis-related metabolites (xylitol and dihydroxyacetone, glucose, fructose-6-phosphate, fructose-1-phosphate), and down-regulation of gluconeogenesis-related metabolite (aspartic acid). Laminar shear stress or steady flow ($\partial\tau/\partial t$) has previously been reported to activate KLF2 to suppress PFKFB3-mediated glycolysis with translational implication in attenuating angiogenesis and vessel sprouting [67, 69]. Our results elucidate the mechanisms whereby pulsatile and oscillatory shear stress differentially modulates endothelial glycolysis via PKCε signaling.

In response to the transition from quiescence to proliferation and migration state, increased glycolytic flux develops in the vascular endothelial cells [67]. This mirrors metabolic changes in other cell types during cell proliferation, including malignancies [203]. During endothelial migration, glycolytic enzymes are specifically translocated to lamellipodia to generate high levels of ATP needed for migration [67]. Inhibition of PFKFB3, a potent activator of glycolysis, has been shown to decrease stalk cell proliferation and tip cell migration during vascular sprouting [36], and treatment with PFKFB3 inhibitor 3PO reduced vessel sprouting *in-vitro* and *in-vivo* using the embryonic zebrafish model [69]. In addition to our observed increase in glycolytic metabolites in response to PSS and OSS, we have demonstrated that increased expression of PKCε significantly elevates basal and maximum glycolysis rates of HAEC *in-vitro* (**Fig. 2c,d**) coupled with an increase in PFKFB3 mRNA expression in response to PKCε over-expression (**Fig. 2e**).

Activation of PKCε by nitric oxide (·NO) has been implicated in cardioprotection in response to ischemia/reperfusion injury [204-206]. The mechanism underlying this cardioprotection has been well-elucidated [75], and treatment with PKCε-selective agonist peptide ψεRACK in the context of ischemia results in the phosphorylation of a number of mitochondrial proteins [73], while hearts of constitutively active PKCε transgenic mice demonstrate conserved mitochondrial membrane potential, maintained oxidative phosphorylation coupling, and decreased cytochrome c release [207]. Additionally, cardiac energetic metabolites such as glucose, lactate, and alanine are more highly preserved in constitutively active PKCε transgenic mice [76], and PKCε activation significantly modulates cardiac glucose metabolism [208, 209]. We demonstrated the effect of PKCε on endothelial glycolysis and PFKFB3 expression in normoxic and oxidative stress conditions (**Fig. 2c-e**). We additionally demonstrate the mito-protective role of PKCε to rescue tube formation under oxidative stress conditions (**Fig. 7**).

Additionally, we introduce a method to modulate shear stress *in-vivo* using the embryonic zebrafish model (**Fig. 3, Supplemental Videos 1-3**). Injection of GATA-1a

MO significantly inhibits erythropoiesis up to 6 dpf [210], and computational fluid dynamics confirm a significant decrease in shear stress (**Fig. 3d**). Injection of *epo* mRNA promotes erthropoiesis [211], significantly increasing blood viscocity (**Supplemental Video 3**). This is accompanied by a decrease in blood velocity, leading to simulated shear stress values only slightly higher than control (**Fig. 3d**). Modulating shear stress *in-vivo* by increasing or decreasing erythropoiesis has limited negative effects in the embryonic zebrafish model due to the small size allowing sufficient oxygen to passively diffuse during early development, leading to normal tissue development in the absence of normal erythrocyte levels [110].

Overall, pulsatile and oscillatory shear stress modulates endothelial metabolomics to promote glycolysis with translational implication in vascular repair. We demonstrate reducing shear stress significantly attenuates vascular repair and increasing shear stress promotes vascular repair *in-vivo*. Increasing expression of PKCε rescues vascular repair *in-vivo*, and also increases glycolysis *in-vitro*. We recapitulate the role of PKCε in the matrigel tube formation model, and demonstrate the mito-protective mechanism of PKCε promoting tube formation in the presence of oxidative stress. Treatment with pro-glycolytic metabolites rescues tube formation in the absence of PKCε *in-vitro*. Taken together, these findings provide new metabolomic insights into endothelial shear stress response and identify therapeutic potential of targeted metabolites and PKCε in vascular repair.

3.5 Acknowledgements

We are extremely grateful to Dr. Samarel at Loyola University Medical Center for providing contistutively active and dominant negative PKCε adenovirus. We also thank

Dr. Laurent Vergnes and Dr. Karen Reue for their support with the SeaHorse metabolic studies. This work was supported by NIH R01 HL83015 (TKH), NIH R01 HL118650 (TKH), NIH R01 HD069305 (TKH), NIH R01 HL 111437 (TKH), AHA 15PRE2140019 (JL), and T32 HL007895 (RRSP).

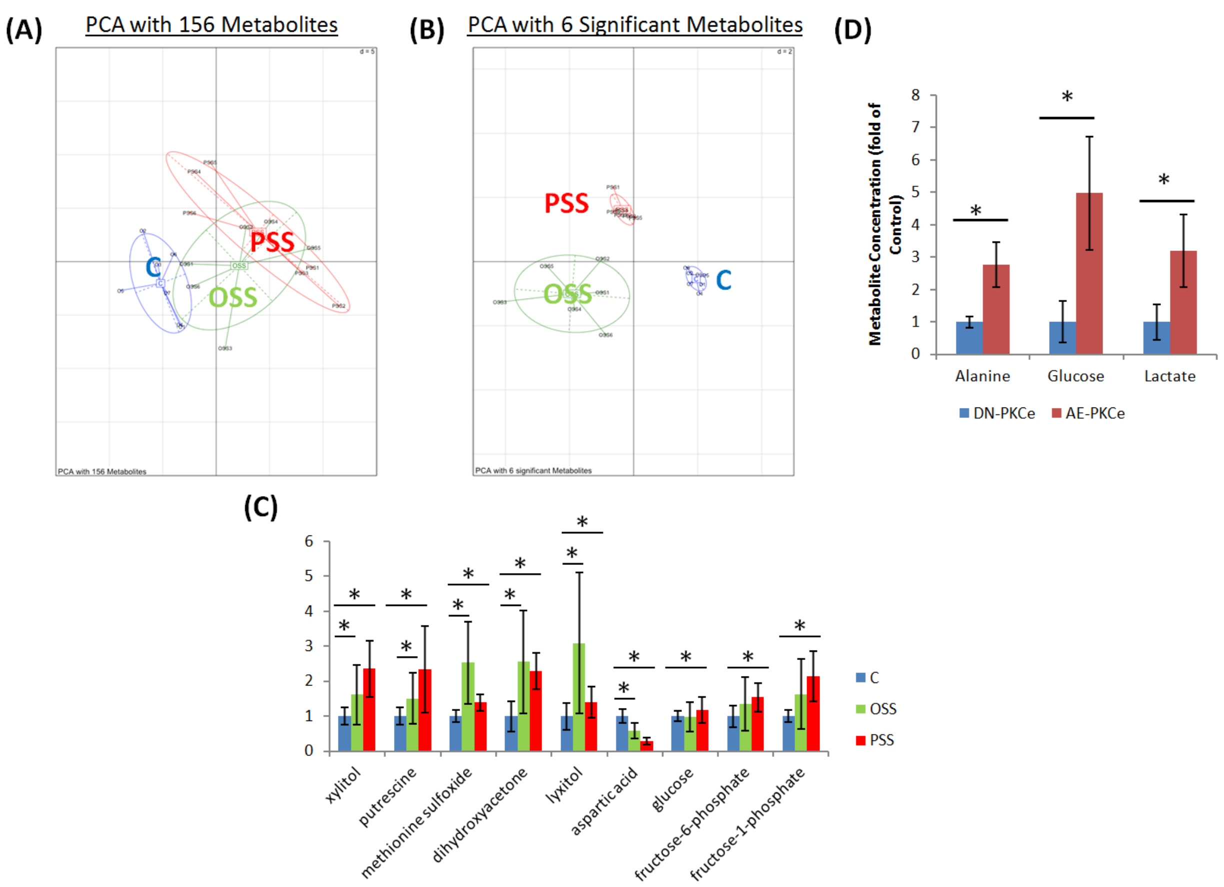

Figure 1. Metabolomic Response to Shear Stress

Metabolite samples were collected from HAEC exposed to either static control (C), OSS, or PSS conditions (*n* = 6 per group). Principal component analysis (PCA) was performed on the host of measured metabolites **(A)** which revealed significant overlap among the three groups. After identification of 6 metabolites statistically different between all groups, PCA using this subset **(B)** revealed clear separation between the groups. Selected metabolites significantly modulated from control are shown **(C)** (**p* < 0.01, *n* = 6). These metabolites include up-regulation of glycolysis-related xylitol, dihydroxyacetone, glucose, fructose-6-phosphate, and fructose-1-phosphate as well as down-regulation of gluconeogenic metabolite aspartic acid. In the active PKCε transgenic mouse model in the setting of ischemia reperfusion injury, glycolysis-related metabolites; namely, alanine, glucose, and lactate, are increased to confer cardiac protection **(D)**.

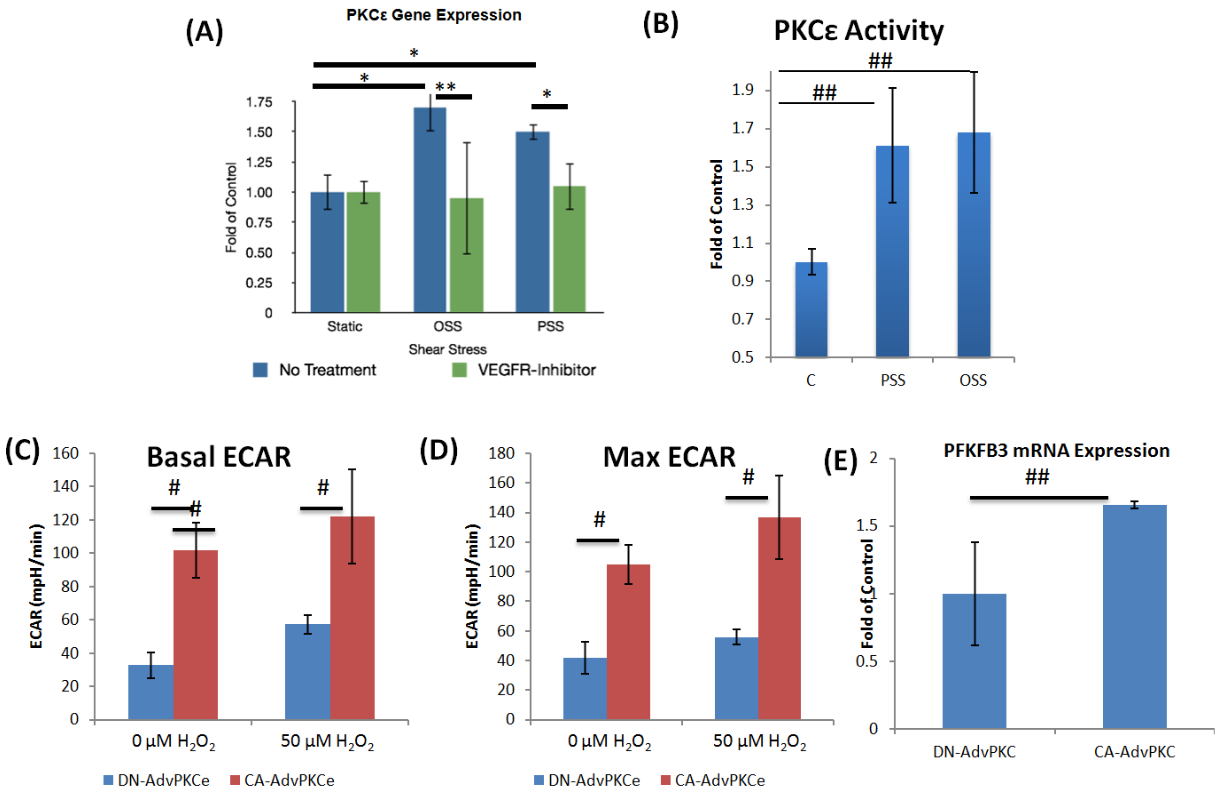

Figure 2. Protein Kinase Cε is Flow-Responsive and Modulates Glycolysis in Endothelial Cells

PKCε mRNA (**A**) and activity **(B)** levels both increased in response to oscillatory shear stress (OSS) and pulsatile shear stress (PSS) (*$n = 3$, $p < 0.01$, ** $n = 3$, $p < 0.05$). Additionally, treatment with CA-AdvPKCε to overexpress constitutively active PKCε significantly increased basal (**C**) and max (**D**) extracellular acidification rate (ECAR), a marker of glycolysis, in control conditions and under exposure to 50 μM H2O2 (#$n = 4$, $p < 0.01$). Under oxidative stress conditions induced by treatment with 50 μM H2O2, CA-

AdvPKCε significantly increased the mRNA expression of PFKFB3, a prominent promoter of glycolysis, compared to DN-AdvPKCε control (##$n = 3$, $p < 0.05$) (**E**).

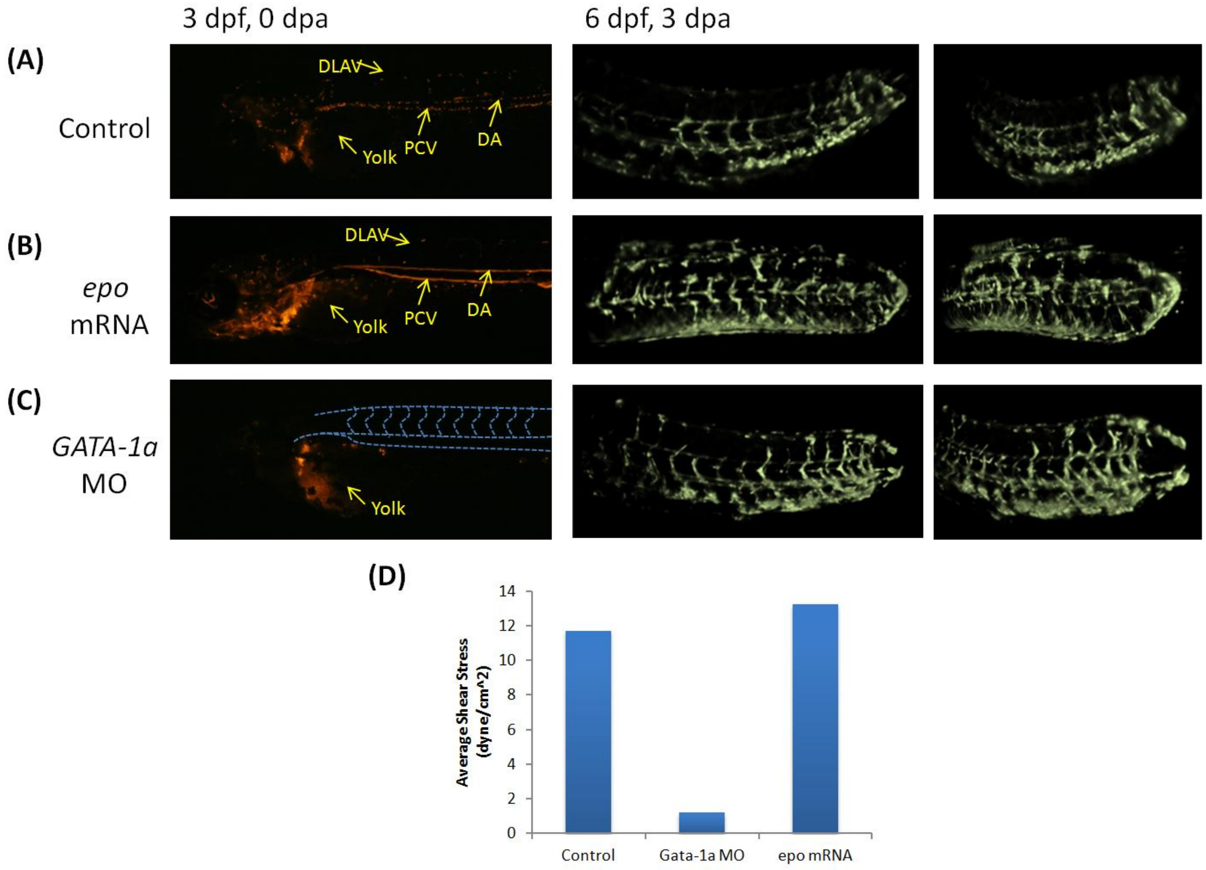

Figure 3. ***In-Vivo*** **Modulation of Shear Stress in Embryonic Zebrafish**

Tg(GATA1a:dsRed) zebrafish embryos were injected with control solution (**A**), 1 nL epo mRNA (20 ng/uL) (**B**) or GATA-1a MO (8 ng/nL) (**C**) at the 1-4 cell stage. At 3 dpf the effects of the epo mRNA and GATA-1a MO can be clearly observed, with significantly increased dsRed fluorescence in the epo mRNA-injected fish, and significantly decreased fluorescence in GATA-1a MO-injected fish. Key embryonic vascular features have been highlighted – the dorsal longitudinal anastomotic vessel (DLAV), posterior cardinal vein (PCV), dorsal aorta (DA), and yolk. Vascular features are not visible in the GATA-1a injected embryos, but have been outlined to aid visualization. At 6 dpf, 3 days post-amputation, SPIM imaging reveals differential tail regeneration. Time-average shear stress at 6 dpf at the tail was simulated using PIV and a 2-D model of the vasculature (**D**). Treatment with GATA-1a MO significantly reduced average shear stress, while epo mRNA injection slightly increased shear stress compared to control.

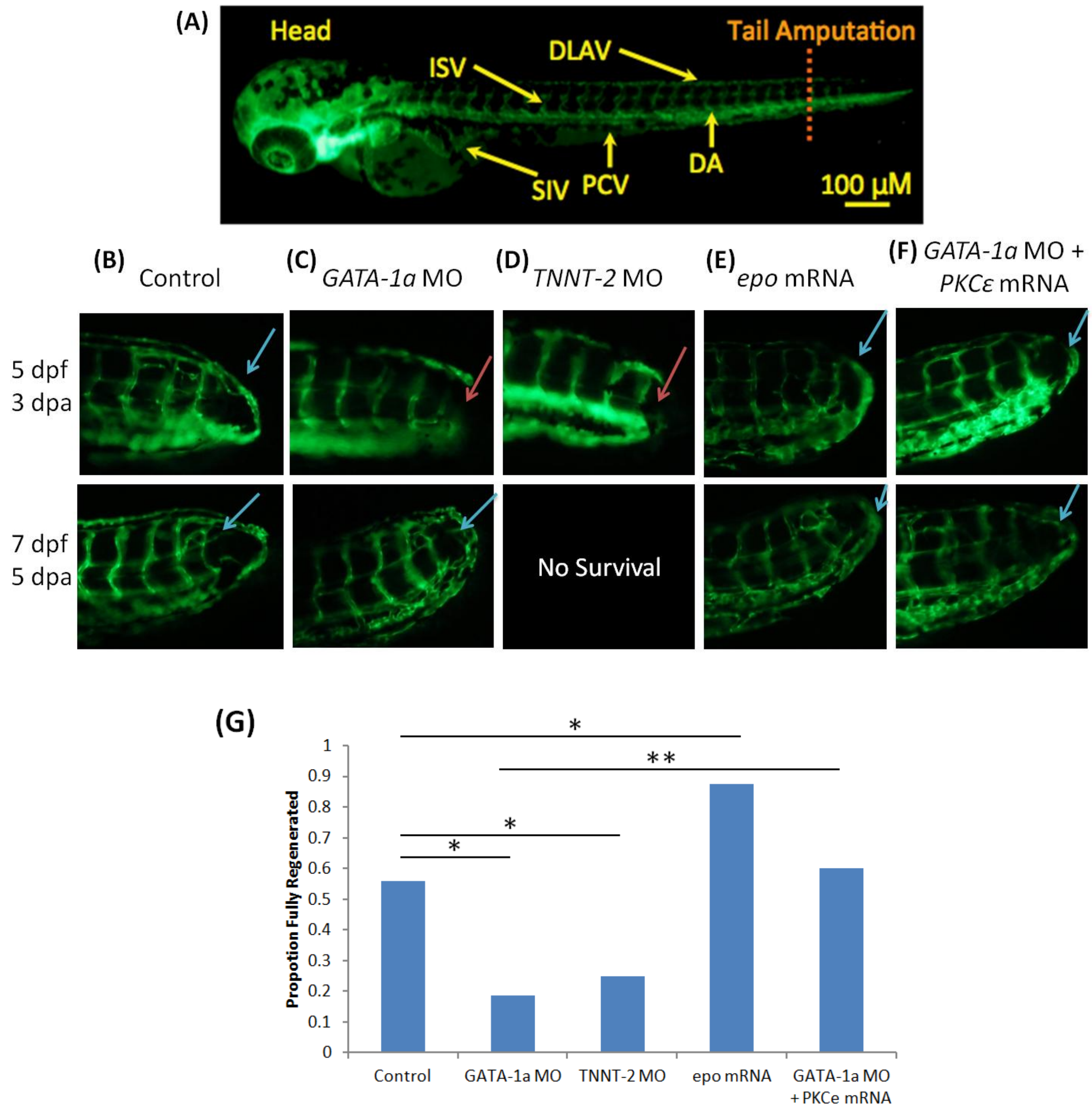

Figure 4. Vascular Repair is Shear Stress-Dependent

Tg(flk1:GFP) embryos were amputated at 2 days post-fertilization (dpf) as shown (**A**). Vascular repair was imaged at 3 days post-amputation (dpa)/5 dpf (**B**). Repair was impaired at 5dpf/3dpa after injection with GATA-1a MO to inhibit red blood cell formation (**C**) (n = 30, $p < 0.01$) or TNNT-2 MO to inhibit cardiomyocyte contraction (**D**) (n = 5, $p < 0.05$). After red blood cell production resumed at 5 dpf in embryos injected with GATA-

1a MO, vascular repair occurred within 2 days (**C**) (*n* = 10, $p < 0.01$). epo mRNA injection promoted tail repair (**E**). Co-injection of GATA-1a MO with PKCε mRNA rescued tail repair at 5 dpf/3dpa (*n* = 5, $p < 0.05$) (**F**). Proportions of embryos exibiting full repair at 3 dpa were quantified (**G**) (* $p < 0.05$ ** $p < 0.01$)

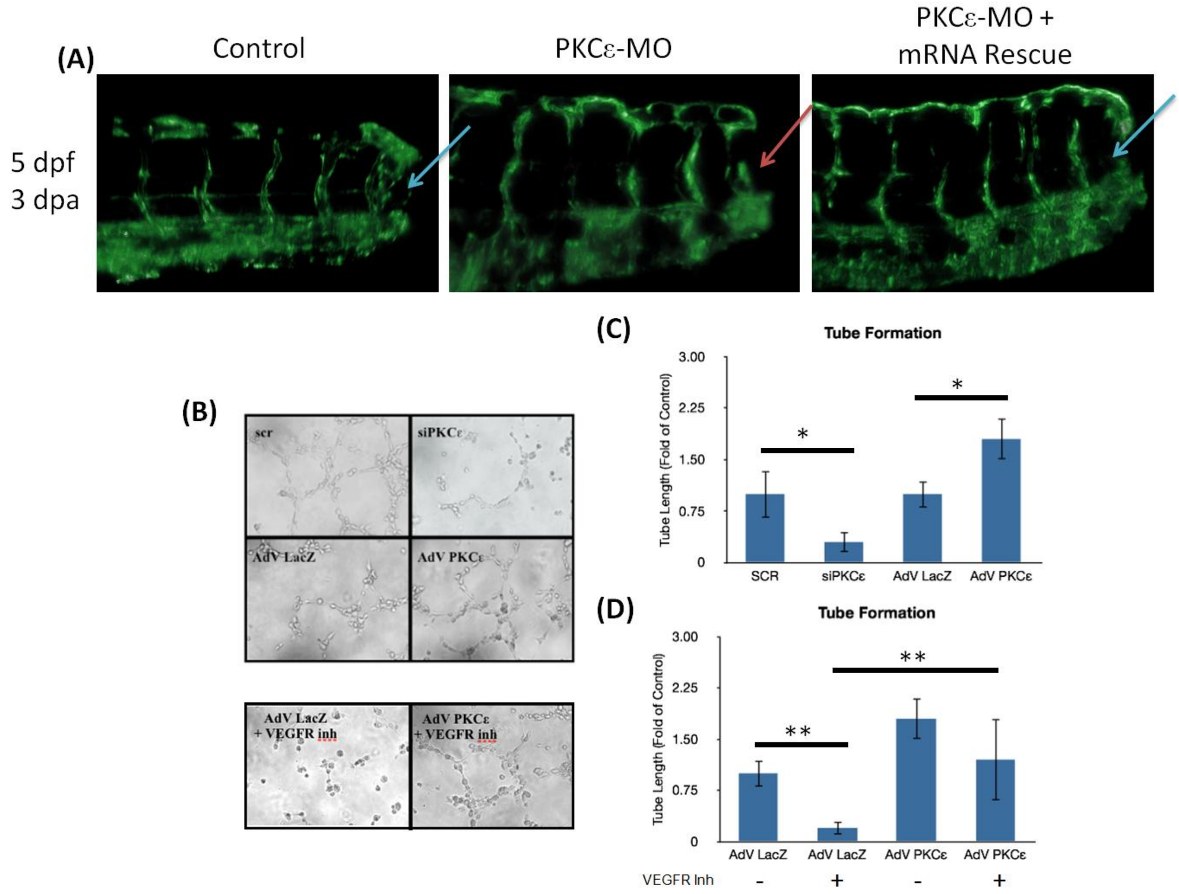

Figure 5. PKCε is implicated for vascular repair in both the *in-vivo* and *in-vitro* model

We acquired 3-D selective plane illumination microscopy (SPIM) images of vascular repair following amputation in the control injection, injection of PKCε MO, and co-injection of PKCε with PKCε mRNA rescue, showing that repair was significantly inhibited in the absence of PKCε, but this effect could be rescued by co-injection (**A**) (*$n = 20$, $p < 0.02$). These results were recapitulated in the *in-vitro* tube formation model, where tube formation was significantly reduced by treatment with siPKCε, but significantly increased by treatment with CA-AdvPKCε (**B,C**) ($n = 5$, $p < 0.02$). Treatment with VEGFR inhibitor, Cediranib, significantly reduced tube formation in the control, however treatment with CA-AdvPKCε rescued this effect, indicating that PKCε is downstream of VEGF signaling (**C,D**) (***n* = 5, $p < 0.05$).

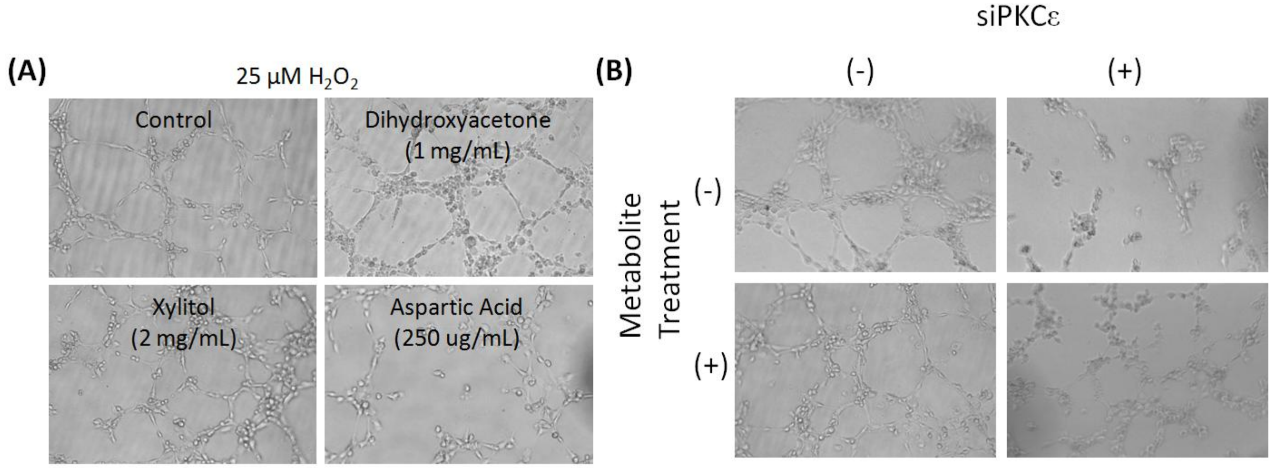

Figure 6. Effect of Glycolytic Metabolites on Tube Formation

In the presence of 25 µM H_2O_2 to induce oxidative stress, treatment with dihydroxyacetone and xylitol were able to partially rescue tube formation, while aspartic acid significantly attenuated tube formation relative to control (**A**). Under normoxic conditions, treatment with a positive set of metabolites (glucose, fructose-6-phosphate, fructose-1-phosphate, dihydroxyactone, and xylitol) was able to rescue tube formation in the presence of siPKCε while treatment with aspartic acid had no effect (**B**).

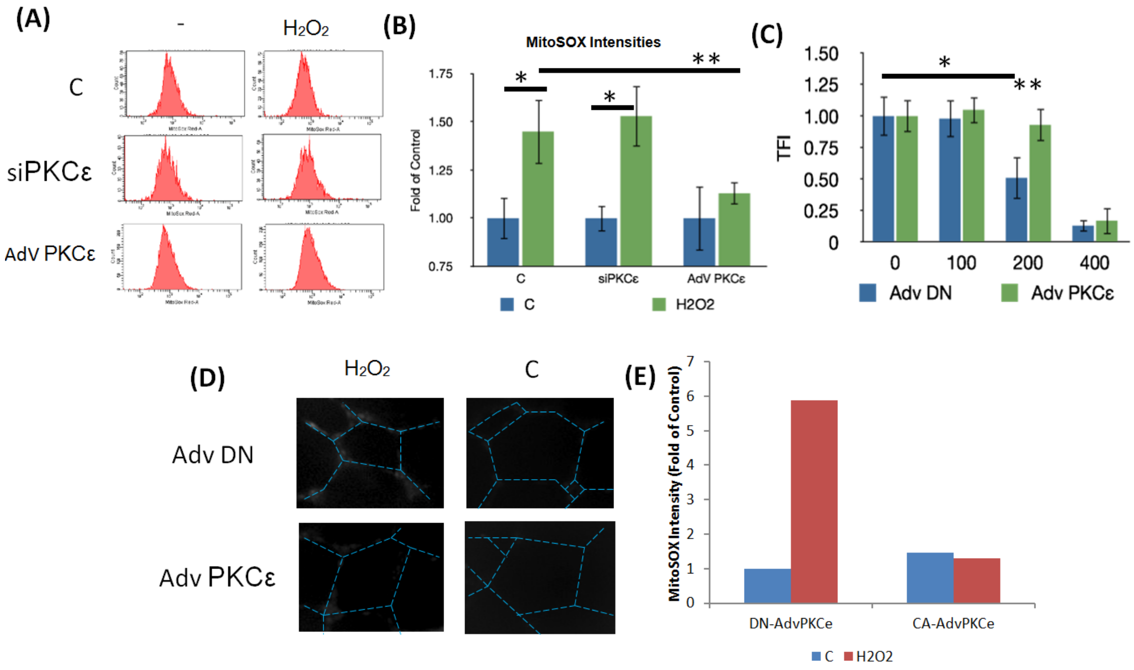

Figure 7. PKCε is mito-protective under oxidative stress conditions

In response to treatment with 200 μM H_2O_2 for 4 hours, Adv PKCε significantly attenuated mitoSOX intensities (**A,B**). At a 200 μM, H_2O_2 treatment significantly attenuated tube formation; however, this was overcome with Adv PKCε treatment (**C**). Images of mitoSOX intensity during tube formation (**D**) validated that when treated with Adv PKCε, mitoSOX levels were decreased during tube formation (**E**).

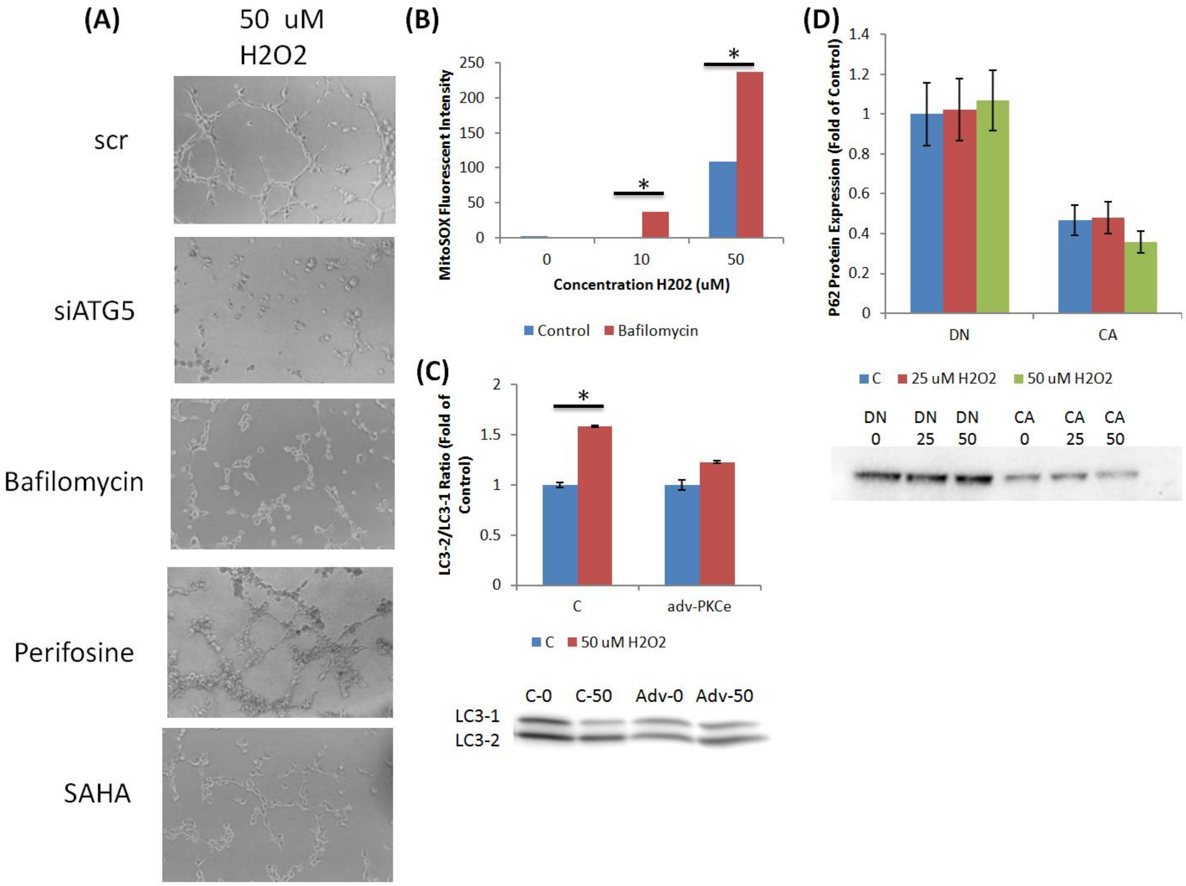

Figure 8. PKCε is implicated in autophagic flux to enable tube formation in the presence of oxidative stress

(**A**) Treatment with siRNA targeting ATG5 to inhibit autophagy as well as treatment with autophagy inhibitor Bafilomycin significantly inhibited *in-vitro* HAEC tube formation in the presence of 50 uM H2O2 to induce oxidative stress. Treatment with autophagy activators, Perifosine and SAHA, rescued vessel formation in the presence of oxidative stress. (**B**) Mitochondrial superoxide (mtO2.-) levels were significantly increased in the presence of Bafilomycin compared to control (**p* < 0.05, n = 3), following treatment with varying concentrations of H2O2, indicating that autophagy plays a key role in regulating mitochondrial homeostasis in response to oxidative stress. (**C**) While treatment with

$H2O2$ induced autophagy as measured by LC3-2/LC3-1 ratio in HAEC (*$p < 0.01$, $n = 3$)*,* treatment with adv-PKCe reduced autophagy levels 4 hours post-oxidative stress. (**D**) P62 protein levels, a reverse marker of autohpagic flux, show an increased level of autophagic flux in response to treatment with constitutively active adv-PKCe (CA) compared to dominant negative (DN).

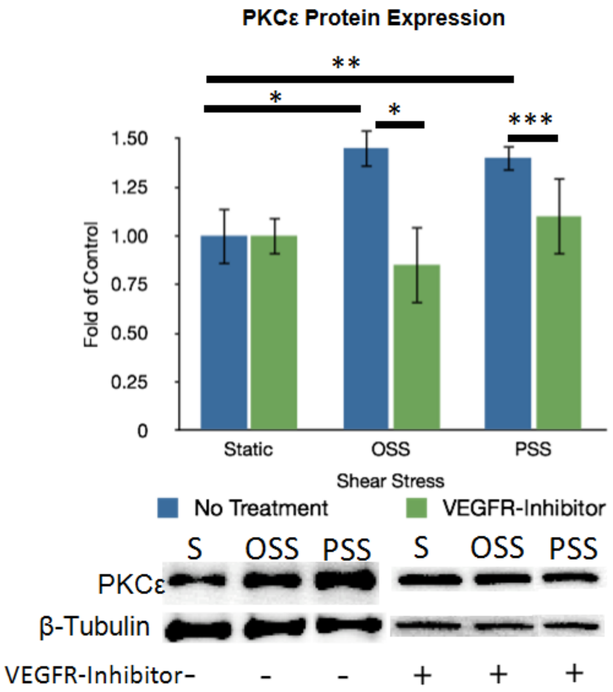

Supplemental Figure 1. OSS and PSS Up-Regulate PKCε in a VEGF-Dependent Manner

Exposure to 4 hr of OSS or PSS significantly increased PKCε protein expression (*$p < 0.01$, ** $p < 0.02$, $n = 4$), while treatment with VEGFR-inhibitor Cediranib significantly attenuated this effect (*$p < 0.01$, *** $p < 0.05$, $n = 4$).

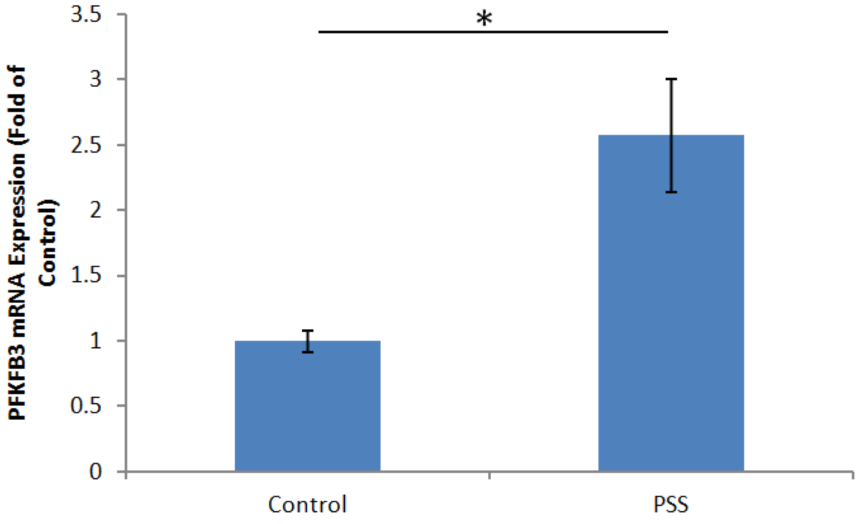

Supplemental Figure 2. Pulsatile Shear Stress Promotes Glycolysis

4-hour PSS treatment increased PFKFB3 mRNA expression levels by 2.6-fold (* $p < 0.01$, n=6).

[Supplemental Videos Available Online]

Supplemental Video I: Micro-injection with the control MO displayed a normal blood circulation in dorsal aorta (DA), posterior cardinal vein (PCV), and subintestinal vein (SIV) in *Tg(GATA1a:dsRed)* transgenic embryos at 5 dpf.

Supplemental Video II: Micro-injection with *GATA-1a* MO led to absence of erythrocytes at 5 dpf.

Supplemental Video III: Micro-injection with *epo* mRNA significantly increased erythropoiesis and blood viscosity at 5 dpf.

Chapter Four: Pulsatile Shear Stress Increased Mitochondrial Membrane Potential: Implication of Mn-SOD

This manuscript is adapted with permission and excerpted from:

Li R, Beebe T, Cui J, Rouhanizadeh M, Ai L, Wang P, Gundersen M, Takabe W, Hsiai TK. "Pulsatile shear stress increased mitochondrial membrane potential: implication of Mn-SOD." Biochem Biophys Res Commun. 2009 Oct 16; 388(2): 406-12. Copyright © 2009 by Elsevier Inc.

4.1 Introduction

Vascular oxidative stress plays an important role in atherosclerosis[86-88]. Hemodynamics, particularly fluid shear stress, regulates the generation of vascular nitrogen (RNS) and reactive oxygen species (ROS)[48, 50, 89]. While eNOS is the major source of RNS, NADPH oxidase system is considered as a major source of ROS in vascular endothelial cells[89, 90]. Mitochondria are also an important source of cellular superoxide anion ($O_2^{\cdot-}$) and H_2O_2[87]. Mitochondrial function is relevant to metabolic homeostasis[80]. Oxidative phosphorylation in the mitochondria drives the proton translocation across the mitochondrial inner membrane to intermembrane space[100], generating an electrochemical proton gradient that is expressed as mitochondrial membrane potential ($\Delta\Psi_m$)[99].

Mitochondrial $\Delta\Psi_m$ is an important indicator of mitochondrial energetic state and cell viability[99]. $\Delta\Psi_m$ is coupled with oxidative phosphorylation to drive ATP synthesis[101, 102]. During myocardial reperfusion injury, opening of the mitochondrial permeability transition pore (MPTP) collapses $\Delta\Psi_m$ and uncouples oxidative phosphorylation, resulting in ATP depletion and apoptosis[103, 104]. Fluid shear stress is reported to influence mitochondrial ATP synthesis, which is coupled with $\Delta\Psi_m$[105].

The formation of mitochondrial ROS (mtROS) is dependent on $\Delta\Psi_m$[97], and mtROS level increases exponentially as $\Delta\Psi_m$ is hyperpolarized above -140 mV[212]. In response to oxidative stress, mitochondrial manganese superoxide dismutase (Mn-SOD) is up-regulated[106], leading to dismutation of $O_2^{\cdot-}$ anion to H_2O_2. In response to laminar shear stress, cytosolic CuZn-SOD expression is also up-regulated[213].

However, the potential mechanism whereby shear stress modulates $\Delta\Psi_m$ via Mn-SOD remains unknown.

We hypothesized that pulsatile shear st*ress (PSS) increased $\Delta\Psi_m$ via an up-regulation of Mn-SOD expression.* In this paper, we provided the following new insights: (1) PSS increased $\Delta\Psi_m$ in HAEC, (2) PSS up-regulated Mn-SOD mRNA and protein expression, and (3) adding Mn-SOD mimetic, MnTMPyP, increased $\Delta\Psi_m$ to the similar extent as induced by PSS while silencing Mn-SOD attenuated PSS-induced increase in $\Delta\Psi_m$. Our findings suggest Mn-SOD up-regulation represents a potential pathway whereby shear stress influenced $\Delta\Psi_m$.

4.2 Materials and Methods

4.2.1 Endothelial Cell Culture

Human aortic endothelial cells (HAEC) were purchased from Cell Applications (San Diego, CA) and cultured in endothelial growth medium (Cell Applications). Endothelial cells (ECs) between passages 4 and 7 were seeded on Cell-Tak cell adhesive (Becton Dickson Labware, Bedford, MA) and Collagen Type I (BD bioscience, San Jose, CA) coated glass slides at 1.5×10^5 cells per slide ($5\ cm^2$). ECs were grown to confluent monolayers in endothelial growth medium for 48 hours in 5% CO_2 at 37^oC before being set up into the dynamic flow system.

4.2.2 Dynamic Flow System

Two-dimensional dynamic flow channels were used to implement shear stress simulating physiologic flow profiles in human carotid arterial bifurcation. PSS that develops in the medial wall of vascular bifurcations or the straight regions is characterized as unidirectional with a positive net forward flow, whereas OSS that develops at the lateral wall of vascular bifurcations or curvatures is characterized as bidirectional with a zero net forward flow [214]. The 2-D flow system provides the precise and well-defined flow profiles across the width of the chamber at various temporal variations in shear stress ($\partial\tau/\partial t$), frequency, and amplitude [215]. HAEC were exposed to the characteristics of pulsatile shear stress at a time-averaged shear stress (τ_{ave}) of 23 $dyn \cdot cm^{-2}$ with a temporal gradient ($\partial\tau/\partial t$) of 71 $dyn.cm^{-2} \cdot sec^{-2}$. The physiologic environment was maintained by a feedback control system between the thermal couple adjacent to the flow channel and the water bath (Fisher Isotemp)[216]. pH sensor (Accunet AP60, Thermo Fisher Scientific) was used to regulate the rate at which CO_2 was infused to maintain a pH of 7.4 in culture medium.

4.2.3 Measurement of Mitochondrial Membrane Potential ($\Delta\Psi_m$)

After exposure to the above flow conditions, HAEC were washed and incubated with a cationic fluorescent dye, tetramethylrhodamine methyl ester ($TMRM^+$) (Molecular probes, Carlsbad, CA), an indicator dye for $\Delta\Psi_m$ [217, 218] at 10 nM for 30 minutes in a Dulbecco's Phosphate Buffered Saline (D-PBS, Hyclone, UT). Fluorescence was measured to calculate $\Delta\Psi_m$. To measure $\Delta\Psi_m$ in response to mitochondrial respiratory chain inhibitors, uncouplers and other chemicals, confluent monolayers of HAEC were treated with (1) 1µM of rotenone (Sigma) (to inhibit the electron transfer from Fe-S centers in Complex I to ubiquinone), (2) 5µg/mL of oligomycin (Alexora) (to inhibit ATP synthase), (3) 1µM of FCCP (Carbonylcyanide-4-(trifluoromethoxy)-phenylhydrazone) (Sigma) (a protonophore and potent uncoupler of oxidative phosphorylation), (4) 10µM

Cyclosporine-A (inhibitor of mitochondrial permeability transition pores), or (5) 50μM MnTMPyP (Alexora) a mimic of Mn-SOD for 1 hour at 37°C. After treatment, the cells were washed and incubated with $TMRM^+$ at 10nM in D-PBS for 30 minutes as described above. Two methods were used to measure $TMRM^+$ fluorescence intensity, which was converted to voltage. 1). Fluorescence microscopy: after treatment, cells were imaged at an excitation wavelength of 555 nm and emission wavelength of 580 nm by the fluorescence microscope (Olympus IX70) and captured with a high performance digital CCD camera (Pixelfly II, Cooke Corporation, MI). The $TMRM^+$ fluorescence intensity in the mitochondria of individual cells was captured by luminescence spectrometer (Perkin Elmer Instruments LS 55) and analyzed by IPlab software (BD bioscience). 2). Flow Cytometry (FACS): After treatment, HAEC were washed with D-PBS, trypsinized, centrifuged, and resuspended in the D-PBS buffer containing $TMRM^+$ at 10nM. $TMRM^+$ intensity was measure with FACS Caliber system from BD Biosciences.

4.2.4 Conversion of $TMRM^+$ Fluorescent Intensity to Voltage

Calculation of $\Delta\Psi_m$ from fluorescence intensity was performed essentially as described by Nicholls[219]. To account for the plasma membrane potential ($\Delta\Psi_p$) in the intact cells, we monitored $\Delta\Psi_p$ by “Membrane Potential Assay kit” (Molecular Devices, Sunnyvale, CA). The fluorescence intensity was captured at an excitation wavelength of 488 nm and emission of 527 nm (Olympus IX70). Calibration curve for $\Delta\Psi_p$ was established by probing the fluorescent intensity at the potassium concentration, ranging from 3.9 mM to 80 mM, followed by application of the Nernst equation[219].

4.2.5 Measurement of Mitochondrial Superoxide Production

Mitochondrial superoxide was measured with flow cytometry (FACS) after staining with mitochondrial superoxide specific dye MitoSOX Red (Invitrogen) as described[200].

4.2.6 Quantitative RT-PCR

Mn-SOD mRNA expression is measured with quantitative RT-PCR. Total RNA was isolated using the RNeasy kit (Qiagen). RNA was reverse-transcribed, followed by PCR amplification using the SuperScript III Platinum two-Step qRT-PCR Kit with SYBR Green (Invitrogen, Carlsbad, CA). The expression levels were normalized to that of 18s rRNA. The primers were as follows: Mn-SOD, forward primer: 5´-GGA AGC CAT CAA ACG TGA CT-3´, reverse primer: 3´-AGC AGG GGG ATA AGA CCT GT-5´; 18s rRNA, forward primer: 5’**-** AAA CGG CTA CCA CAT CCA AG-3’, reverse primer: 5’**-** CCT CCA ATG GAT CCTCGT TA **-**3’. Fidelity of the PCR reaction was determined by melting temperature analysis. The difference in C_T values for various conditions versus control was used to determine the relative difference in the levels of Mn-SOD mRNA expression.

4.2.7 Mn-SOD Activity Assay:

Cells exposed to static condition or shear stress were scrapped into PBS and spun down. The cells were lysed in Mn-SOD assay sample buffer (10mM HEPES, pH7.9, 420mM NaCl, 1.5mM MgCl2, 0.5mM EDTA, 0.1% Triton X-100) for 20 minutes in ice. After spin at 12000g for 5 minutes, the supernatant was collected for Mn-SOD activity assay. Mn-SOD activities were measured using the SOD assay kit from

Cayman Chemicals (#706002 Ann Arbor, MI) in the presence of 2mM potassium cyanide, which inhibited the activities of Cu-Zn-SOD and EC-SOD but not Mn-SOD. Relative SOD activities were expressed as absorbance at 450 nm in the absence SOD less absorbance with sample or SOD standard. Reading in the presence of 1U/ml of SOD standard was used as blank. Relative Mn-SOD activities were normalized to protein concentration of samples.

4.2.8 Transfection of siRNA in Human Aortic Endothelial Cells

Silencer siRNAs for Mn-SOD were custom-designed by Ambion (Austin, TX). The sequences were as follows: sense sequence: GGC CUG AUU AUC UAA AAG Ctt, anti-sense sequence: GCU UUU AGA UAA UCA GGC Ctg. Confluent human aortic endothelial cells (HAEC) were trypsinized and re-suspended to 100,000 cells/mL in standard growth medium. siPORT NeoFX transfection reagent (Ambion, Austin, TX) was diluted in OPTI-MEM I (Invitrogen, CA) medium and incubated at room temperature for 10 minutes. Mn-SOD siRNA at a final concentration of 30 nM was diluted in OPTI-MEM I and mixed with diluted siPORT NeoFX reagent at room temperature for additional 10 minutes. The transfection solution was dispensed into the 6-well plates, followed by adding HAEC in suspension. The medium was changed to standard growth medium after 24 hours. The medium was replaced every other day until confluent HAEC monolayer developed. The cells were cultured for another 24hours and then used for experiments. Quantitative RT-PCR and Western blot were performed to assess the levels of silencing. Scrambled siRNA were used as the control.

4.2.9 Western Blot

Cells were harvested, washed with phosphate-buffered saline and lysed with RIPA buffer. The lysate was centrifuged at 12,000g for 10 minutes, and the resulting supernatants were used as the whole cell lysate. 15µg protein samples were size-separated in 10% SDS BioRad polyacrylamide electrophoresis gel (BioRad, CA). Mn-SOD and ß-tubulin (loading control) were detected with rabbit Mn-SOD antibody (Upstate), mouse anti-ß-tubulin antibody (Millipore). Chemiluminescence signal was developed with Supersignal Western Pico (Pierce) and recorded with FluorChem FC2 (Alpha Inotech Inc). Densitometry scan of western blot was done with the software come with FlorChem FC2 machine.

4.2.10 Statistical Analysis

Data are expressed as mean ± SD and compared among separate experiments. For comparisons between two groups, two-sample independent-groups t-test was used. Comparisons of multiple values were made by one-way analysis of variance (ANOVA), and statistical significance among multiple groups determined using the Tukey test (for pairwise comparisons of means between static-like and pulsatile flow conditions). *p*-values of < 0.05 were considered statistically significant.

4.3 Results

4.3.1 Characterization of Mitochondrial Membrane Potential ($\Delta\Psi_m$) in Human Aortic Endothelial Cells (HAEC)

We employed $TMRM^+$ dye to measure mitochondrial membrane potential ($\Delta\Psi_m$). Mitochondrial respiratory chain inhibitors and uncouplers were used to validate the method in intact HAEC. Addition of FCCP, a protonophore to uncouple oxidative phosphorylation, depolarized $\Delta\Psi_m$ in the intact HAEC and decreased the $TMRM^+$ intensity by 30% compared to the control ($P < 0.05$, n=5). Treatment with rotenone, a NADH dehydrogenase inhibitor, depolarized $\Delta\Psi_m$ and decreased the $TMRM^+$ intensity by 56% ($P < 0.05$, n=5). Treatment with oligomycin, an ATP synthase inhibitor, hyperpolarized $\Delta\Psi_m$ and increased $TMRM^+$ intensity by 2.5-fold ($P < 0.05$, n=5). Furthermore, cyclosporine-A, an inhibitor of mitochondrial permeability transition pores (MPTP), increased the $TMRM^+$ intensity by 2.6-fold ($p < 0.05$, n=5, **supplemental Fig. 1A**). The change in $TMRM^+$ intensity were converted to $\Delta\Psi_m$ (mV) as described in materials and methods with background level of $\Delta\Psi_m$ set at -140mV. In control condition, $\Delta\Psi_m$ was -140mV ± 6.9. In the presence of FCCP, Rotenone, Oligomycin and cyclosporine A, $\Delta\Psi_m$ was -118.6mV ±5, -107.8mV± 7.3, -165mV± 4.2 and -165.3mV ±9.8, respectively (**supplemental Fig.1B**). These data were in agreement with published results [220, 221]. Hence, the dynamic range of $TMRM^+$ provided a basis to characterize shear stress-induced $\Delta\Psi_m$.

4.3.2 Pulsatile Shear Stress Increased Mitochondrial Membrane Potential ($\Delta\Psi_m$)

In response to pulsatile shear stress (PSS) simulating arterial flow at a time-averaged shear stress (τ_{ave}) of 23 $dyn \cdot cm^{-2}$ for 2 and 4 hours, endothelial cells became energized as evidenced by an increase in $\Delta\Psi_m$ (**Fig. 1A**. static: -140 mV±4.9; PSS 2 hours: -170.5±1.5 mV, $P<0.05$, n=4; PSS 4 hours: -187.5±5.6 mV, $P<0.05$, n=4). The dynamic changes in $\Delta\Psi_m$ were consistent with those of physiological range in mammalian cells between -90 and -180 mV[212]. Fluorescence microscopy indicated that PSS increased $TMRM^+$ uptake by HAEC (**Fig. 1B**), consistent with an increase in mitochondrial membrane potential. In parallel, PSS increased mitochondrial superoxide production (**Fig. 1C**). PSS is considered to be cardioprotective[222] and our observations suggest that one of the possible mechanisms whereby PSS confers cardioprotection may be due to an increase in $\Delta\Psi_m$ that is important for oxidative phosphorylation and ATP synthesis[99].

4.3.4 Pulsatile Shear Stress Up-regulated Mn-SOD Expression in HAEC

In response to PSS for 4 hours, Mn-SOD mRNA level was up-regulated by 3.6-fold as compared to that of static condition (*P* <0.01, n=3) (**Fig. 2A**). Mn-SOD protein expression was also increased by 1.9-fold (**Fig. 2B**). In parallel, Mn-SOD activities were increased by 40% (**Fig. 2C**). Next, HAEC were subjected to PSS for 2 hours, followed by static condition for 4 hours. Mitochondrial $\Delta\Psi_m$ was increased to -160±5.3 mV in response to PSS for 2 hours (**Fig. 3A**), a similar trend shown in Fig.1A. $\Delta\Psi_m$ returned to near baseline value at -145±6.4 mV (baseline was -140 mV) after 4 hours in static condition. This finding suggests that changes in $\Delta\Psi_m$ are a dynamic process in response to shear stress. Despite the static condition, the Mn-SOD protein and activity levels remain elevated (**Fig. 3B & 3C**), consistent with Mn-SOD mRNA up-regulation at 4 hours in response to PSS as previously reported in bovine aortic endothelial cells[223].

4.3.5 Mn-SOD Expression Modulated PSS-Mediated Mitochondrial Membrane Potential

To test the role of Mn-SOD on $\Delta\Psi_m$, we first treated HAEC with Mn-SOD mimetic, MnTMPyP, for 4 hours. MnTMPyP treatment resulted in an increase in $\Delta\Psi_m$ to a similar extent as induced by PSS (**Fig. 4A,** *p*<0.05, n=3). To examine the effect of Mn-SOD level on PSS-mediated $\Delta\Psi_m$ change, we transfected HAEC with Mn-SOD siRNA (siMn-SOD). siMn-SOD decreased Mn-SOD mRNA expression by 80% compared to scrambled siRNA in HAEC (**Fig. 4B**). siMn-SOD significantly attenuated PSS-mediated $\Delta\Psi_m$ (**Fig. 4C,** *p*<0.05, n=3). Taken together, our findings support the notion that PSS-induced Mn-SOD expression plays a role on changes in $\Delta\Psi_{m.}$

4.4 Discussion

In this study, we employed a dynamic fluorescent technique to monitor mitochondrial membrane potential ($\Delta\Psi_m$). We demonstrated that pulsatile shear stress (PSS) increased $\Delta\Psi_m$ in the intact aortic endothelial cells (HAEC). PSS also up-regulated mitochondrial Mn-SOD expression. Treatment of HAEC with Mn-SOD siRNA attenuated PSS-mediated increase in $\Delta\Psi_m$ while Mn-SOD mimetic, MnTMPyP, increased $\Delta\Psi_m$ to similar extent as PSS. Our findings suggest that PSS hyperpolarized $\Delta\Psi_m$ via *Mn-SOD up-regulation*.

Maintenance of $\Delta\Psi_m$ at physiologic range (~ -90mV to -150mV) is critical for cellular function [212]. Important factors that influence $\Delta\Psi_m$ include (1) proton leakage across the inner membrane, (2) ATP synthesis or hydrolysis, (3) substrate availability, (4) electron flux through the respiratory chain, and (5) ion transport[224]. The methyl esters of tetramethylrhodamine ($TMRM^+$) is useful for monitoring mitochondrial depolarization relevant to cytosolic Ca^{++} transient and for imaging time-dependent mitochondrial membrane potential[225]. The precise concentration of $TMRM^+$ was critical to detect step changes in $\Delta\Psi_m$. At a low concentration (10 nM), $TMRM^+$ operates at the distribution/redistribution mode. When the mitochondrial membrane is depolarized, $TMRM^+$ in mitochondria undergoes dequenching, rendering a decrease in fluorescent intensity. Distribution mode is applicable to our experiments that involved slow step changes in $\Delta\Psi_m$ at a low $TMRM^+$ concentration[225].

Several lines of evidence support that shear stress increases exogenous ATP release. ATP production is a process dependent on $\Delta\Psi_m$[80]. Kudo *et al.* demonstrated an increase in $\Delta\Psi_m$ and ATP production in endothelial cells exposed to laminar shear stress for 48 hours in a parallel plate flow system[105]. Our data showed a hyperpolarized $\Delta\Psi_m$ in response to pulsatile shear stress within 2 hours. An increase in $\Delta\Psi_m$ is accompanied with an increase of ATP release and the generation of mitochondrial reactive oxygen species (mtROS) when $\Delta\Psi_m$ is above -140mV[101, 102]. *In response to PSS, mitochondrial superoxide generation in HAEC was increased compared to static condition (**Fig. 1C**).* Thus PSS can modulate $\Delta\Psi_m$ and mitochondrial redox state with an implication for endothelial function.

Over-expression of Mn-SOD or SOD mimetic has been shown to protect against beta-amyloid-induced neuronal death and improved mitochondrial respiratory function[226]. Mn-SOD was also reported to suppress selenite-induced decrease in mitochondrial membrane potential[227]. Furthermore, over-expression of Mn-SOD reduced polarization of colorectal cancer cells[228]. In this study, we demonstrated that PSS increased $\Delta\Psi_m$ in endothelial cells, which was at least partially mediated via up-regulation of Mn-SOD expression. Hence, Mn-SOD is important in maintaining homeostasis of endothelial cell function as an antioxidant[229, 230]. Although the precise mechanisms remain to be identified, Mn-SOD-mediated membrane potential increase is likely related to its antioxidant activity since the activity of proton pumps depends on the reductive power at the respiratory chain of mitochondria.

A host of factors modulates mitochondria membrane potential. While Mn-SOD may contribute to PSS-mediated increase in $\Delta\Psi_m$, other factors such as metabolic status and ATP level may dominate. Our data showed that $\Delta\Psi_m$ returned to baseline level (-145mV) after 2 hours of PSS followed by 4 hours of static condition. At the same time, both Mn-SOD protein levels and activities remained elevated. These data are consistent with shear stress-induced Mn-SOD mRNA at 4 hours and the ensuing protein expression observed in bovine aortic endothelial cells[223]. While membrane potential returned to baseline after shear stress exposure, the persistent elevated Mn-SOD may plays an important role in dismutating mitochondrial superoxide production to maintain mitochondrial homeostasis[80].

In summary, PSS favors mitochondrial energetic state with an implication for mitochondrial function in endothelial cells[105]. In this paper, we linked pulsatile shear stress with mitochondrial $\Delta\Psi_m$ in the intact vascular endothelial cells via Mn-SOD regulation. Regulation on $\Delta\Psi_m$ may represent one of the mechanisms whereby pulsatile shear stress confers a cardioprotective effect. The precise mechanisms will be of important interest for future investigation.

4.5 Acknowledgements

The authors were grateful for the scientific advice from Dr. Enrique Cadenas of the Department of Molecular Pharmacology & Toxicology at the University of Southern

California. The authors also appreciate the technical advice from David G. Nicholls of Buck Institute for Age Research, Novato, California. This work was supported by AHA Pre-Doctoral Fellowship 0615063Y (MR), AHA GIA 0655051Y (TKH), NIH HL 83015 (TKH), and HL NIH HL068689 (TKH).

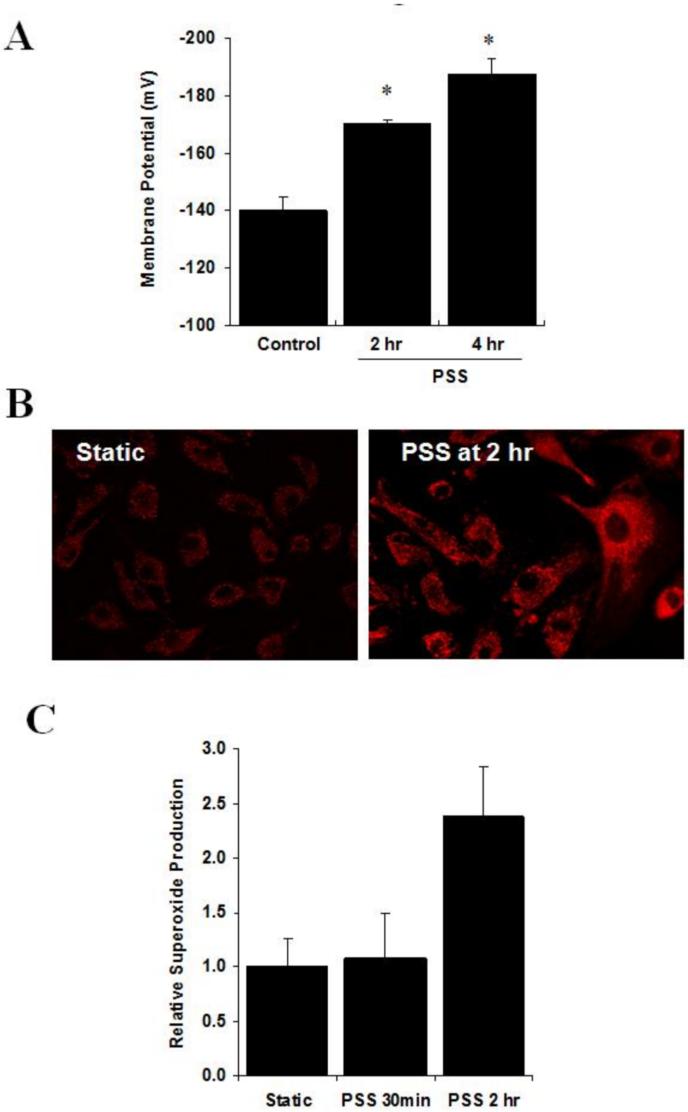

Fig. 1. Pulsatile shear stress (PSS) increased mitochondrial membrane potential ($\Delta\Psi_m$).

A: HAEC were exposed to static condition or PSS for 2 and 4 hours. After PSS exposure, cells were incubated with 10 nM TMRM$^+$ for 30 minutes. TMRM$^+$ intensity was measured by FACS and converted to voltage (mV) as described in "Material and Methods" (* $p < 0.05$ versus static condition, n = 4). **B:** HAEC were exposed to static condition or PSS for 2 hours. Cells were incubated with 10 nM TMRM$^+$ for 30 minutes.

Images were taken with fluorescence microscope. The images were representative of 4 independent experiments. **C**. HAECs were exposed to PSS for 30 minutes or 2 hours. Mitochondrial superoxide production was measured by flow cytometry using mitochondrial superoxide probe MitoSOX Red. Relative superoxide production was calculated based on fluorescence intensity.

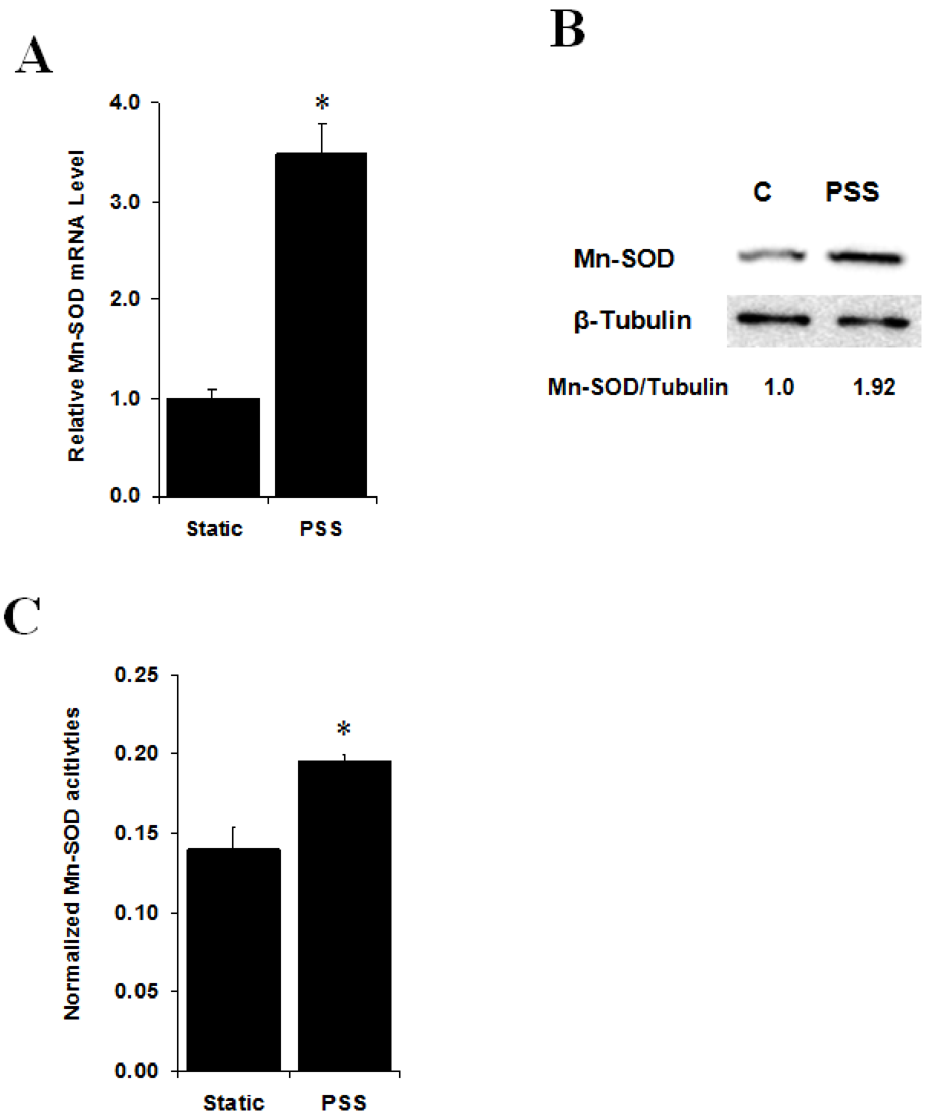

Fig. 2. Pulsatile shear stress up-regulated Mn-SOD expression and activities.

A: HAEC were exposed to static condition or pulsatile shear stress (PSS) for 4 hours. RNAs were isolated and the expression of Mn-SOD mRNA were measured by quantitative RT-PCR and normalized to 18S rRNA (* *p*<0.01, n=3)**.** **B:** HAEC were exposed to static condition or PSS for 4 hours. Mn-SOD protein expression was assessed by western blot. The relative expression of Mn-SOD protein was normalized to β-tubulin from density scan data. ***C**:* HAEC were exposed to static condition or PSS.

The cells were lysed and Mn-SOD activities were measured as described. Relative Mn-SOD activities were normalized to protein concentration (* $p<0.01$, n=3).

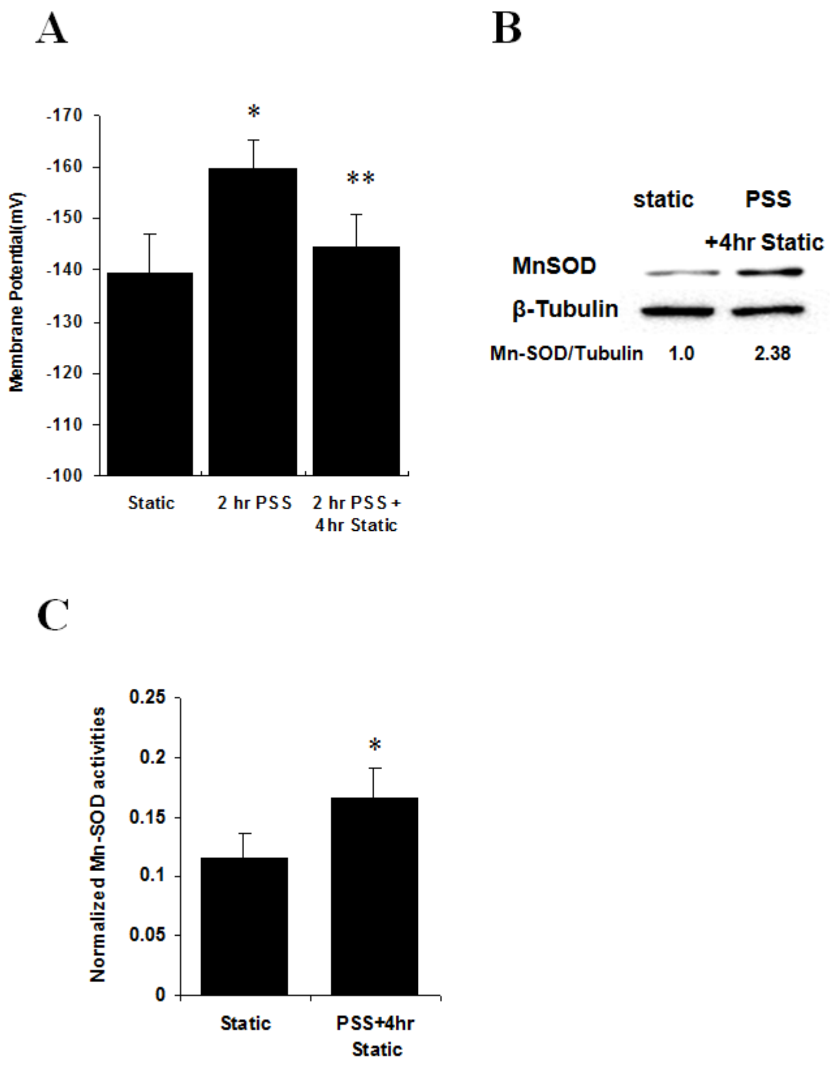

Fig.3. Changes of mitochondrial membrane potential in response to PSS were a dynamic process.

HAEC were subjected to three conditions: (1) static state for 2 hours, (2) PSS exposure for 2 hours, and (3) PSS exposure for 2 hours followed by static state for 4 hours. Mitochondrial membrane potential (**A**), Mn-SOD protein levels (**B**) and Mn-SOD activities (**C**) were measured. (* p<0.02 vs. static state, n=3; ** p<0.05 vs. PSS, n=3).

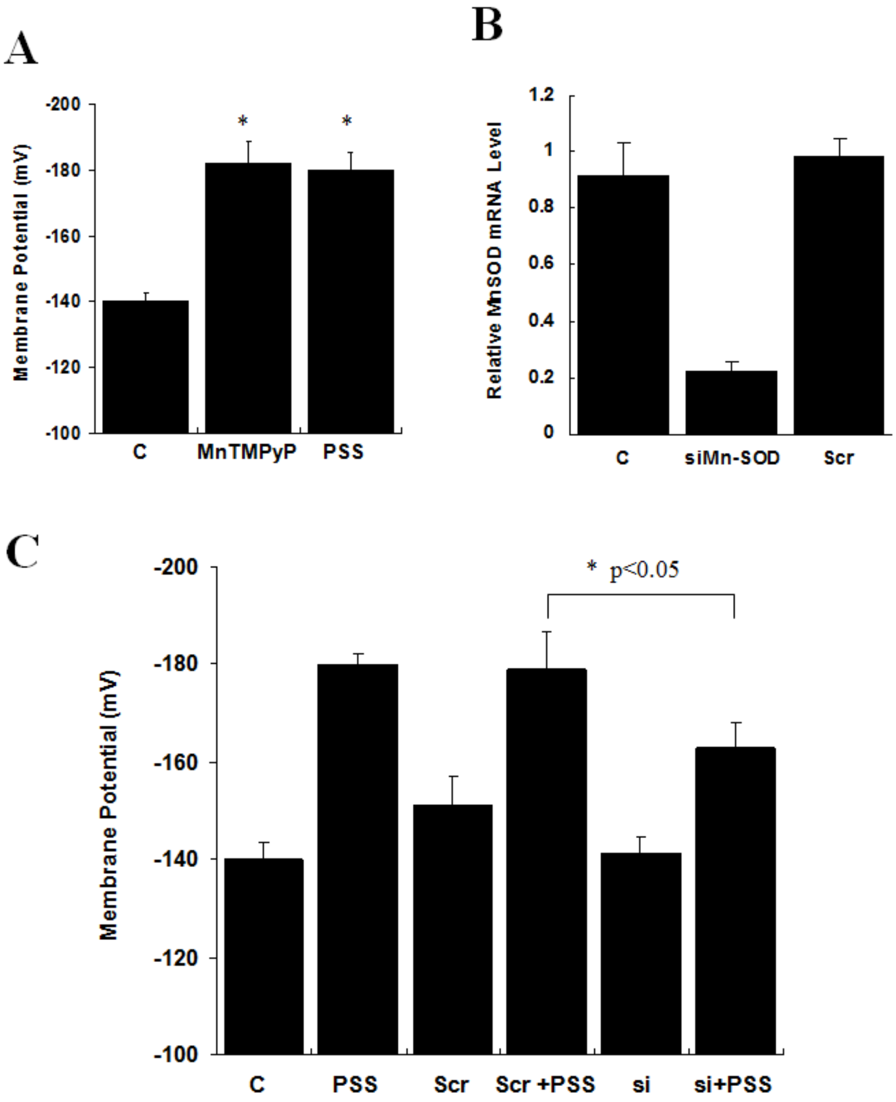

Fig. 4. Mn-SOD mediated PSS-increased mitochondrial membrane potential.

A: Treatment of HAEC with 50μM of Mn-SOD mimetic, MnTMPyP, for 4 hours resulted in an increase in $\Delta\Psi_m$ to a similar extent as induced by PSS for 4 hours. **B:** HAEC were transfected with scrambled control siRNA (Scr) or siRNA for Mn-SOD (siMn-SOD). Mn-SOD mRNA expression was measured by quantitative RT-PCR. Mn-SOD siRNA treatment induced an 80% reduction in Mn-SOD mRNA expression compared to scrambled siRNA. **C:** HAEC were transfected with control siRNA (Scr) or siMn-SOD (si) followed by exposure to shear stress or static condition. Membrane potential was measured. siMn-SOD attenuated PSS induced mitochondrial membrane potential as compared to control siRNA (* $p < 0.05$, n = 3).

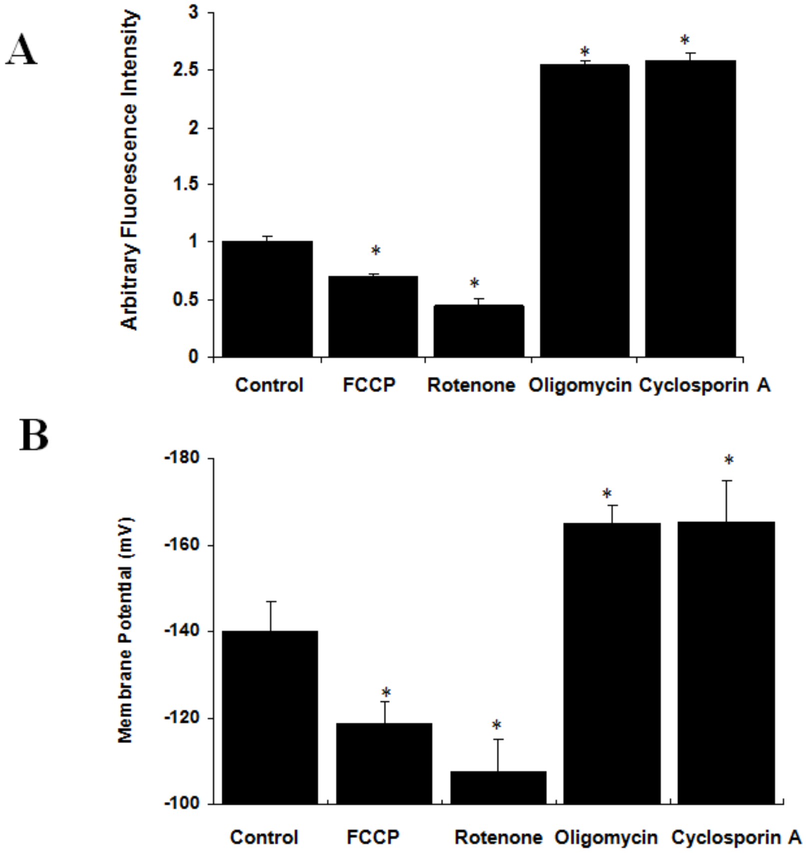

Supplement Fig. 1. Validation of TMRM+ dye to measure mitochondrial membrane potential (ΔΨm).

(A) HAEC were treated with mitochondrial respiratory chain inhibitors and uncouplers (1µM FCCP(Carbonylcyanide-4-(trifluoromethoxy)-phenylhydrazone), 1uM rotenone, 5µg/mL of oligomycin or 10µM Cyclosporine-A for 1 hour at 37°C. After treatment, the cells were washed with D-PBS and incubated with TMRM+ at 10nM in D-PBS for 30 minutes. The cells were then trypsinized, centrifuged, and resuspended in the DPBS buffer containing TMRM+ at 10nM. TMRM+ intensity was measured by flow cytometry. **(B)** Mitochondrial membrane potential in the presence of mitochondrial respiratory chain inhibitors and uncouplers: Nernst equation was applied to convert TMRM+ signals from above to ΔΨm. The changes in ΔΨm in response to mitochondrial respiratory chain inhibitors and uncouplers followed the trends in TMRM+ intensity. (* $p<0.05$ vs control, n=5)

Chapter Five: Flexible and Waterproof Micro-Sensors to Uncover Zebrafish Circadian Rhythms: The Next Generation of Cardiac Monitoring for Drug Screening

This manuscript is adapted with permission and excerpted from:

Beebe T, Zhang X, Jen N, Lee C, Tai Y, Hsiai TK. "Flexible and waterproof micro-sensors to uncover zebrafish circadian rhythms: The next generation of cardiac monitoring for drug screening." Biosens Bioelectron. 2015 Sep 15; 150-7.

5.1 Introduction

The first generation of flexible electronics was established for micromachine-based shear stress sensor arrays mounted on the non-planar surface of air foils for turbulence control[231]. Over the last decade, the advent of flexible microelectronic membranes is evidenced by the biomedical applications to interrogate electrical depolarization in the small vertebrate hearts[126, 127], and the deployment of intravascular flexible shear stress sensors to assess atherosclerotic plaque[127]. These parylene-based high-density electrode arrays have further enabled electrical stimulation in the retina to restore vision and spinal cord to restore locomotion[128]. Stretchable multi-electrode arrays (MEA) further unravel aberrant electrophysiological phenotypes of small animal models of heart regeneration[129]. The MEA membranes adhere to the non-planar body surface, identifying spatial variations in cardiac injury currents from zebrafish hearts[129]. The PDMS-based epidermal electronics revolutionized non-invasive monitoring for mapping cardiac conduction and brain activity[130, 131]. These high density arrays offer precise spatial control of stimulation and recording otherwise challenging with the traditional fine-wire electrodes[128].

Developmental genes involved in zebrafish heart repair are highly conserved in higher vertebrates. The average length of an adult fish is at 2 to 4 cm, accessible for relatively low-cost and high-throughput small molecule screening[132]. Their physiological complexity also provides conserved models of human disease for *in vivo* validation studies[122]. The biological characteristics of zebrafish are suitable for toxicity testing, including eco-toxicology[133]. However, the *Clock* gene involved in the central oscillation to coordinate endogenous rhythms is linked to the generation of circadian rhythms[134]. Thus, sedation of zebrafish influences the circadian variations in heart rate (HR) and heart rate variability (HRV) in response to cardiac injury or to drug testing.

The first micro-electrocardiogram (µECG) signals obtained from adult zebrafish required muscle paralysis[135-137]. The gill motion was arrested to reduce electromagnetic (EMG) artifacts while oxygenation was provided to prevent hypoxia and arrhythmias via a needle-to-mouth resuscitation[135-137]. Our group avoided paralytic agents to establish high signal-to-noise ratios for µECG signals via wavelet transform with Tricaine-based sedation[136, 137]. However, translating the zebrafish model to unequivocal drug screening and toxicity testing in the absence of sedation remained a challenge.

To address circadian rhythm-associated heart rates (HR) and heart rate variability (HRV), we have designed stretchable parylene cable and microelectrodes to establish 24 hour telemetry of adult zebrafish. We performed real-time recording and analyses of µECG signals at 10, 18 and 26 days post ventricular amputation without sedation. We compared the nocturnal and daytime HR and HRV prior to and post ventricular amputation. We further identified changes in QTc intervals in response to Amiodarone, a class III anti-arrhythmic agent[232] in the presence versus absence of sedation. Our findings revealed HR and HRV in response to cardiac circadian rhythms, providing a physiological basis to advance drug development and toxicity testing as well as future mobile health and sleep research[233, 234].

5.2 Materials and Methods

5.2.1 Design and Mounting of the Multi-Electrode Array (MEA) to Zebrafish

The design of MEA highlighted two gold (Au) electrodes (chest electrode and reference electrode) at 3 mm apart **(Fig. 1 a-c)**. Each electrode harbored a micro meshed structure with 25µm x 25µm openings to reduce the stress on the Au thin film in response to stretching. We developed a mounting jacket made with micro-molded partially cured silicone MED4210 (Dow Corning, USA) to closer match the fish skin's modulus of approximately 0.04 GPa for long-term wear[235]. The ultra-soft silicone jacket has a Young's modulus of approximately 0.001 GPa, which significantly reduces strain on the fish surface compared to parylene-C's Young's modulus of 3.2 GPa[236-239]. Moreover, to reduce the long-term stress from extra weight of the jacket, micro glass-spheres are mixed in by weight ratio 15:1 (silicone : micro glass sphere) so that the ultrasoft silicone jacket harbored an effective density close to 1g/cm^3. The ultra-soft silicone jacket utilized a zip-tie structure with multiple teeth to adapt to different sizes of the zebrafish. The extended zip tie length was removed with micro surgical scissors after threading to secure the electrode contact to the ventral part of the animal. A back padding was provided to reduce the stress on the dorsal part of the fish where stress was concentrated in response to forward swimming motion. The chest electrode was threaded through the jacket's center "cross" opening, and placed at the tip of the jacket. The electrode was fixed onto the jacket with an additional application of uncured silicone around the anchor holes on the electrodes. The electrode harbored a PA-C/Ti/Au/PA-C stacked structure which underwent a vacuum oven annealing process at 200^0C for 16 hours to enhance long-term parylene-parylene adhesion, and the micro-fabrication process as previously reported[129, 240]. The complete device consisted of PA electrode, cable, silicone jacket, flexible flat connector (**Fig. 2 b**). The micro electrode cable was fixed to a flat FFC cable as a guide to plug into a zero insertion force FFC connector. The fish was able to comfortably wear the jacket and swam freely in the aquatic environment (**Fig. 2 f-g)**.

5.2.2 Signal Processing

Due to the inherent gill motion artifact in absence of sedation, the recorded raw data required further processing to subtract the large breathing baseline for morphology study. Raw data was first processed with a peak detection algorithm[241, 242] to detect the R-peaks in order to index the data into single ECG wave segments. All the segments were then aligned at their R-peaks and averaged to eliminate the non-correlated breathing baselines. The averaged waveform was subsequently baseline subtracted with a cubic spline fitting to generate the ECG wave morphology (**Fig.3 b-c**). The peak detection results were also used to calculate the HR between two consecutive R-peaks as well as HRV. For the raw signals that did not present excessive low frequency artifacts, we further used the adaptive threshold wavelet filter as previously described[129, 136].

5.2.3 Zebrafish

The studies on the zebrafish were performed in accordance with the Institutional Animal Care and Use Committees (IACUC) at Children Hospital Los Angeles, Los Angeles, CA, USA. The animal experiments were performed in compliance with the Guide for the Care and Use of Laboratory Animals of the National Institutes of Health. Adult zebrafish, 3–5 cm in length, were acquired from Tong’s Tropical Fish and Supplies (CA) and maintained under standard laboratory conditions at 24 °C. The individual fish were fed daily with brine shrimp (hatched from eggs in 10 mL in 2 L salt water), kept in constantly circulating water, and isolated from other fish for ECG follow-up post-resection.

5.2.4 Heart Resection

Eighteen fish were divided into two arms: 6 sham operation and 12 apical ventricular resection. Twelve zebrafish underwent apical ventricular resection according to the previously described method[111]. Zebrafish were sedated in 5% Tricaine methanesulfonate (Tricaine). A midline incision of 0.25 cm in length was created posterior to the ventricle and approximately 20% of the apical ventricle was excised by scissors. The control fish underwent sham operation; that is, ventral midline incision was performed without ventricular resection. The zebrafish were returned to freshwater in the presence of a continuous oxygenator.

5.2.5 Amiodarone Treatment

Amiodarone (Sigma) was dissolved in 0.3% dimethyl sulfoxide solution and then added to fish system water to either 10 uM or 50 uM final concentration. Adult zebrafish aged 3 – 6 months were exposed to control system water with DMSO, 10 uM Amiodarone, or 50 uM Amiodarone for 24 hours followed by recording of ECG either by our jacket design as described above or traditional needle electrode ECG recording as described previously[136]. Fish were returned to fresh water after the measurement was complete.

5.3 Results

5.3.1 Parylene C-based Flexible Electrode Design and Fabrication

Two gold (Au) electrodes were embedded into parylene-C 3 mm apart as the recording and reference electrodes (**Fig 1 A-B, E**). The flexible electrode has a parylene-gold-parylene sandwich structure as illustrated in the fabrication process (**Fig 1 C**). The front recording electrode was placed near the heart, and the second placed on the abdomen as reference. Differential ECG voltages were collected by the electrode pair and were processed through the filtering and amplification circuitry. In addition, the electrodes were integrated into a new ultra-soft silicone jacket designed to comfortably wrap around the swimming fish to secure the chest electrodes. The design of the jacket consisted of a zip tie structure to adapt to various fish sizes, back padding to reduce the stress on the fish, and anchoring for the electrode to integrate with the jacket via "wings" on the electrode, which were removed once integrated (**Fig 2 A**). The electrode was connected to an adapter board via a stretchable MEMS cable (**Fig 2 B**).

5.3.2 ECG Recording Signal Processing

The wearable jacket design allowed for the electrodes to be securely adhered to the ventral surface of the zebrafish for ECG recording. Zip ties secured the jacket to the size of the particular fish, and there was padding to reduce stress on the fish, allowing for ECG telemetry for 24 hours**. (Fig 2 C-E.**). Over the 24 hour recording period, no sensitivity loss of the sensor was observed. The fish was able to swim while tethered to the recording system via a stretchable MEMS cable (**Fig 2 F, Supp Fig 1, Supp Video 1**). During signal recording, the fish was confined in a transparent cylinder to restrict movement and to reduce mechanical noise (**Fig 2 G**). Raw ECG data were notable for noise emanated from gill motion and low frequency baseline wandering (**Fig 3 A**). Approximately 500 ECG segments were superimposed at their R peaks, and then averaged, to produce the gill-motion-subtracted ECG (the gill motion was assumed to be non-correlated to the heart beats, and thus were "averaged out"). Individual waveforms were in black, and the averaged ECG waveform in red (**Fig 3 B).** The gill motion subtracted ECG was further subtracted with a manually fitted spline curve (blue) at its iso-electrical line to eliminate the residual gill motion and low frequency baseline. The resulting ECG demonstrated the P-wave, QRS-complex, and T-wave components (**Fig 3 C**).

5.3.3 QT Prolongation and Heart Rate Decrease in Response to Ventricular Resection

Having established ECG telemetry, we investigated the electrical phenotypes in response to ventricular resection. We unraveled circadian rhythm variations in terms of HR and HRV from the non-sedated fish (**Fig 4 A**). Non-sedated HR varied over the course of heart regeneration, with significantly reduced HR at 10 days post-amputation (dpa) (**Fig 4 C**) accompanied by increased HRV (**Fig 4 D**) in the amputated fish compared to control, and normalized to baseline at 26 dpa. QT interval prolongation was observed in the amputated fish at 10 dpa, and normalized to baseline by 26 dpa (**Fig 4 B**). Thus, our 24 hour telemetry identified physiological significance in the heart rate and heart rate variability of the regenerating fish.

5.3.4 QT Prolongation in Response to Amiodarone Treatment

We assessed the effects of sedation on Amiodarone-mediated QT prolongation. We compared non-sedated analysis using our jacket design with sedated regimen using needlepoint electrodes. In the absence of sedation, we observed a decrease in mean HR (n=3, $p< 0.01$) and increase in QT interval (**Fig 5 A-C, Supp Fig 3**), whereas in the presence of sedation, the change in HR was masked ($p < 0.7$, n=4), HRV amongst measurements increased, and the change in QTc was not detected (**Fig 5 D-F, Supp**

Fig 4). Thus, the data highlighted the effect of sedation to mask physiological rhythms and electrical repolarization for cardiac toxicity testing.

5.4 Discussion

The novelty of this study is to establish waterproof wearable sensors for long-term continuous monitoring of zebrafish ECG signals in the absence of confounding sedative effects. Our group has previously developed sensors to detect zebrafish ECG signals to characterize cardiac regeneration under sedation [243] as well as wearable microelectrode membranes for the neonatal mouse model[244]. However, the design of the current wearable sensors is the first to enable long-term non-sedated monitoring of the zebrafish ECG signal for applications such as circadian rhythm detection.. For the first time, the new ultra-soft silicone jacket was designed to comfortably wrap around the swimming fish to secure the chest electrodes. We uncovered circadian rhythm variations in terms of HR and HRV from the non-sedated animals. Specifically, we observed a reduction in mean HR and an increase in HRV at 10 dpa, accompanied by QT prolongation as well as diurnal variations, followed by normalization in mean HR and QT intervals at 26 dpa. We further revealed Amiodarone-mediated QTc prolongation, HR reduction and HRV otherwise masked by sedation. Identifying these physiologically relevant effects otherwise masked by traditional needle electrodes advances future toxicity testing and drug screening.

Our novel design incorporating parylene-C based ECG sensors with an ultra-soft silicone wearable jacket enables ECG telemetry. The extended parylene cable connecting the underwater chest electrodes and out-of water electronics allows the fish to swim freely through its aquatic habitat, and eliminates the needs to disturb the cardiac physiology prior to ECG recording. The zip-tie design of the jacket accommodates varying sizes of fish to maintain adherence of the chest electrodes while the fish is moving. The jacket is made of micro-molded partially cured silicone to match the Young's modulus of the fish surface and to minimize potential tissue strain for long-term wear. Matching elastic modulus properties of the sensing platform with the contacted tissue is important to address patients' acceptance and adherence to flexible and wearable biosensors[245]. Another innovation is to embed micro glass-spheres in the thin film of silicone to reduce the effective density of the jacket to close to 1 $g \cdot cm^{-3}$; thereby, eliminating the additional weight of the jacket. Non-linear signal processing techniques further filters out the breathing and electromagnetic artifacts arising from gill and muscle movements. Together, these advances provide the opportunity for long-term monitoring and observation of circadian phenomena in response to heart resection, repair, and drug toxicity.

Circadian variation in the frequency of onset of acute myocardial infarction has been widely recognized in humans, with a peak incidence between 6 a.m. and 12 noon[246]. Long-term monitoring also allows for a higher chance of observing cardiovascular events - nocturnal cardiovascular events are more frequent at the beginning and end of the night[247]. As a corollary, Zebrafish constitutes the ideal vertebrate system to study the complexity of the circadian clock in relation to behavioral, sleep cycle, cellular, and molecular responses. The National Institutes of Health (NIH) has ranked the role of zebrafish as the third most important experimental organism[248]. It has become a widely used model organism because of its fecundity, its and physiological similarity to mammals, the existence of many genomic tools, and the ease with which large, phenotype-based screens can be performed[233]. They have an immune system, bones, and digestive, nervous and cardiovascular systems. In addition to developmental process and disease modeling, transgenic mutants have provided the opportunity for optogenetic control of cardiac function[249], hemodynamic stress-mediated developmental genes for vascular repair[122], and a platform for *in vivo* drug discovery[233].

The application of zebrafish to preclinical drug development and toxicity testing, including recent advances in mutant generation, strengthens the capabilities this model organism in drug discovery. It is widely known that anesthesia drugs affect both the heart rate and the morphology of ECG measurements. The quantified effects of anesthesia are unknown and heavily based upon individual response, and thus cannot be systematically subtracted. By enabling non-sedated measurement, our wearable and waterproof ECG electrodes uncovered prolonged QT intervals and reduced heart rates in response to Amiodarone at concentrations where traditional sedated needle ECG measurements failed to detect any difference. This enhanced acuity is essential as a preclinical model to recognize potentially dangerous electrocardiac phenotypes.

5.5 Conclusions

In this paper, we introduce the next generation of waterproof and wearable micro-ECG telemetry for mobile health. The ultra-soft jacket for long-term monitoring, the zip-tie design of the jacket to maintain adherence of the electrodes, and the embedded micro-glass spheres for light weight are the technical advances to uncover physiological phenomena for small animal models of tissue regeneration, and drug discovery. The technical innovation further paves the way for mobile health, wearable sensors, and sleep research[233, 234].

5.6 Acknowledgements

This study was supported by National Institutes of Health: HL083015 (T.K.H., N.C.C.) and HD069305 (N.C.C., T.K.H.).

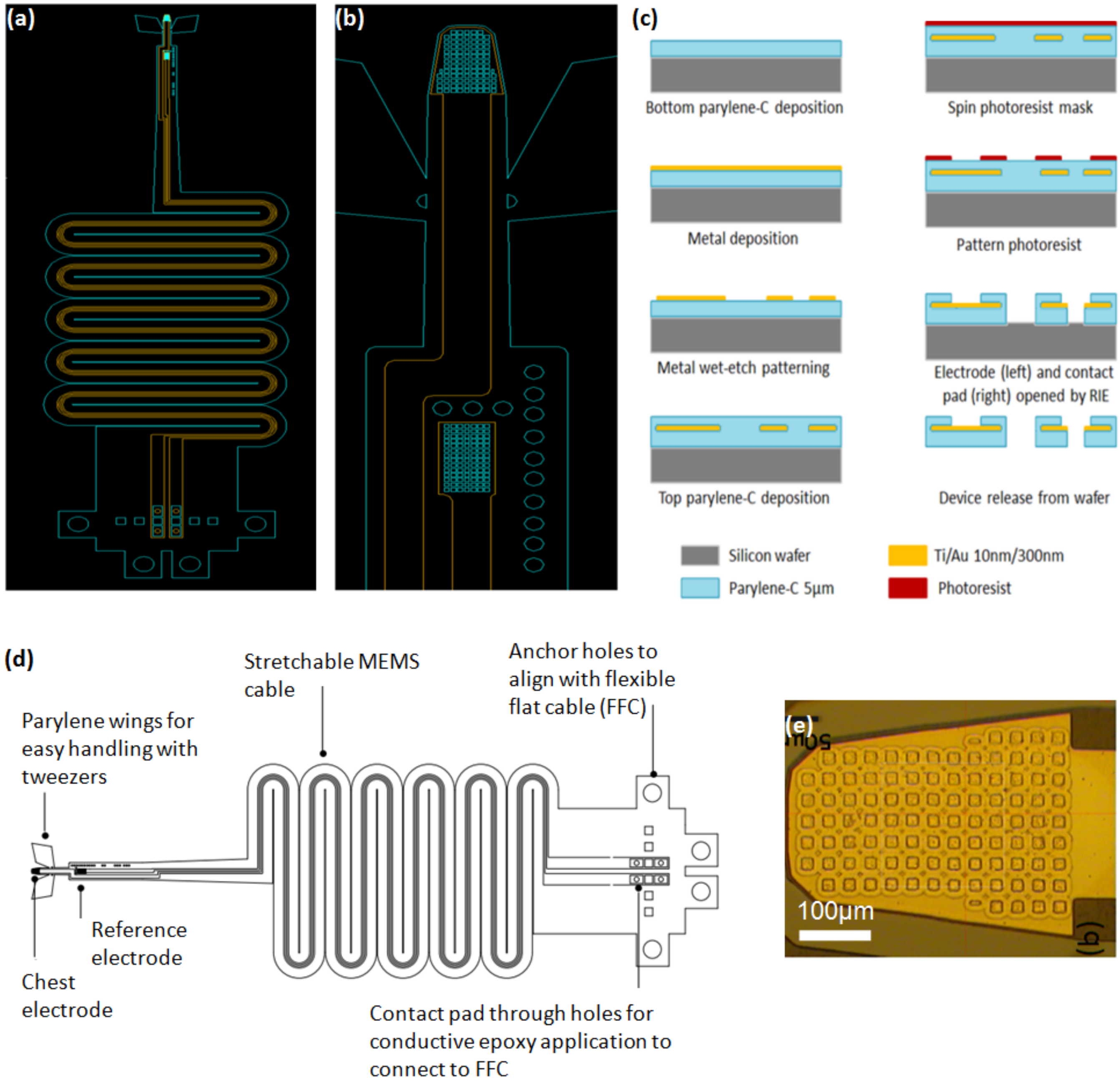

Figure 1: Parylene C-based electrode and cable design, micro-fabrication, and device integration

(a) The blue pattern illustrates the Parylene outline, and yellow pattern is the gold (Au) trace. Two Au electrodes (chest electrode and reference electrode) are patterned at 3 mm apart. Each electrode harbors a micro meshed structure with 5 µm x 25 µm openings designed to reduce stress on the Au thin film in response to stretching. The “wings” next to the chest electrode are designed to thread the zip tie ribbons into the silicone jacket, and are removed after the integration with jacket is complete. The PA holes around the reference electrode allow for anchoring the MEMS electrode/cable onto the jacket. Uncured silicone will be applied at these holes to adhere the electrode onto the jacket. **(b)** The zoomed-in view reveals the chest and reference electrodes. **(c)** Micro-fabrication process of the PA-Au/Ti-PA electrodes highlight the use of parylene C to embed electodes **(d)** Schematic diagram of the flexible cable and electrodes. **(e)** The zoomed-in view reveals the micro mesh openings in the chest electrode. Each opening is at 25 µm x25 µm.

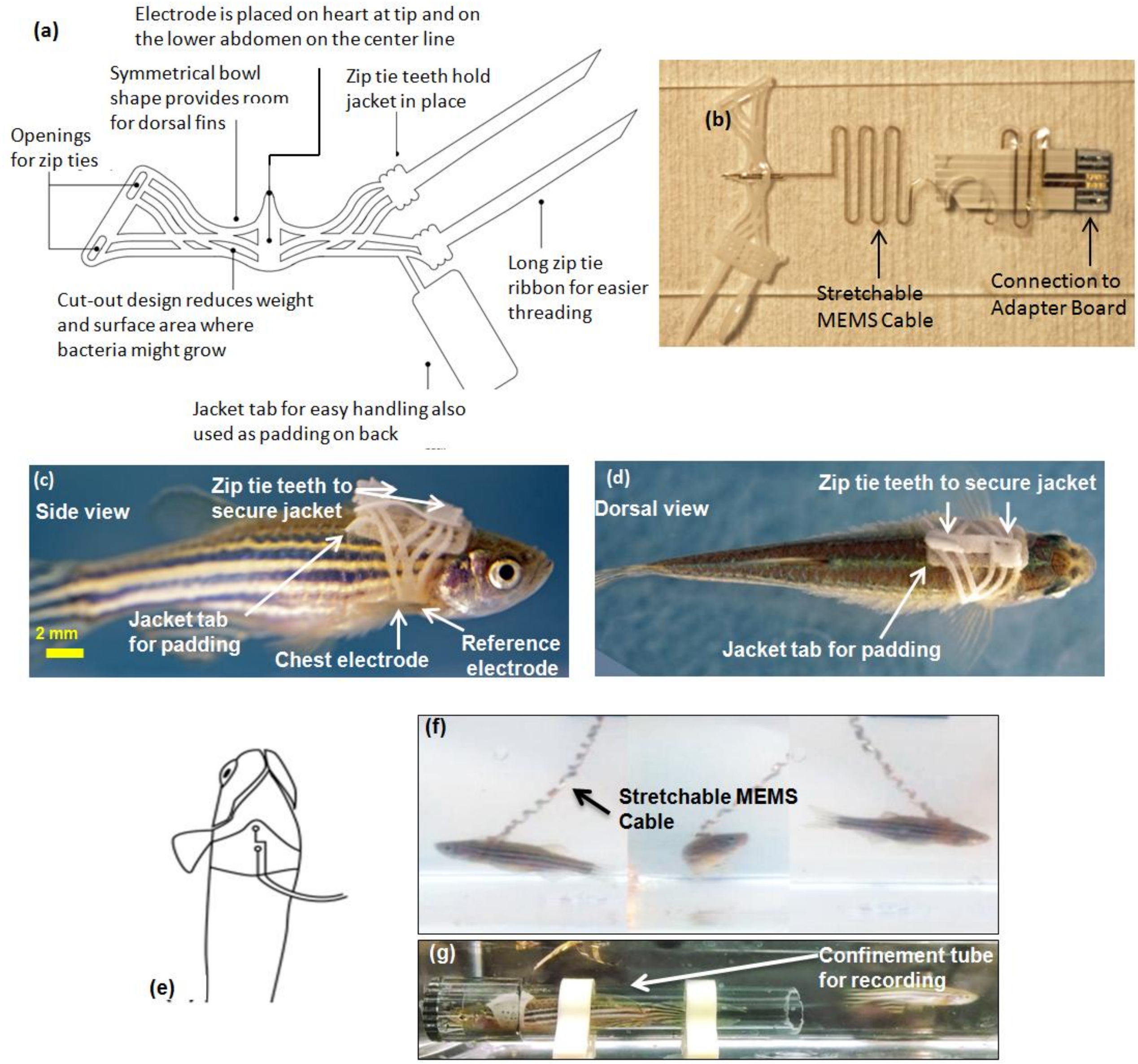

Figure 2. The PDMS-based jacket allows the multi-electrode array (MEA) to securely adhere to the ventral surface of zebrafish for ECG recording.

(a) Schematic diagram of the ultra-soft silicone jacket reveals a zip tie structure with multiple teeth to adapt to various fish sizes; the extended zip tie length will be cut after threading. A back padding reduces the stress on the fish skin in response to the Young’s modulus mismatch between the skin and the silicone jacket. The chest electrode will be threaded through the center “cross” opening at the tip of the jacket. The electrode is anchored at the PA opening holes. **(b)** Stretchable cable and micro electrodes integrated with PDMS jacket and FFC connection. **(c)** and **(d)** Wearable silicone jacket is made of a dry film micro-casted with a medical grade PDMS elastomer (MDX4210, Dow Corning, USA) at a mixing ratio of 20:1 to reduce Young’s modulus, and is mixed with hollow micro glass beads (3M-S38 Microspheres, 3M, USA) to minimize the weight at 1g/ml. . **(e)** A schematic diagram illustrates the placement of electrodes on the ventral part of zebrafish. **(f)** The fish is wearing the silicon jacket tethered to the recording system. **(g)** Fish is confined in a tube for real-time ECG recording.

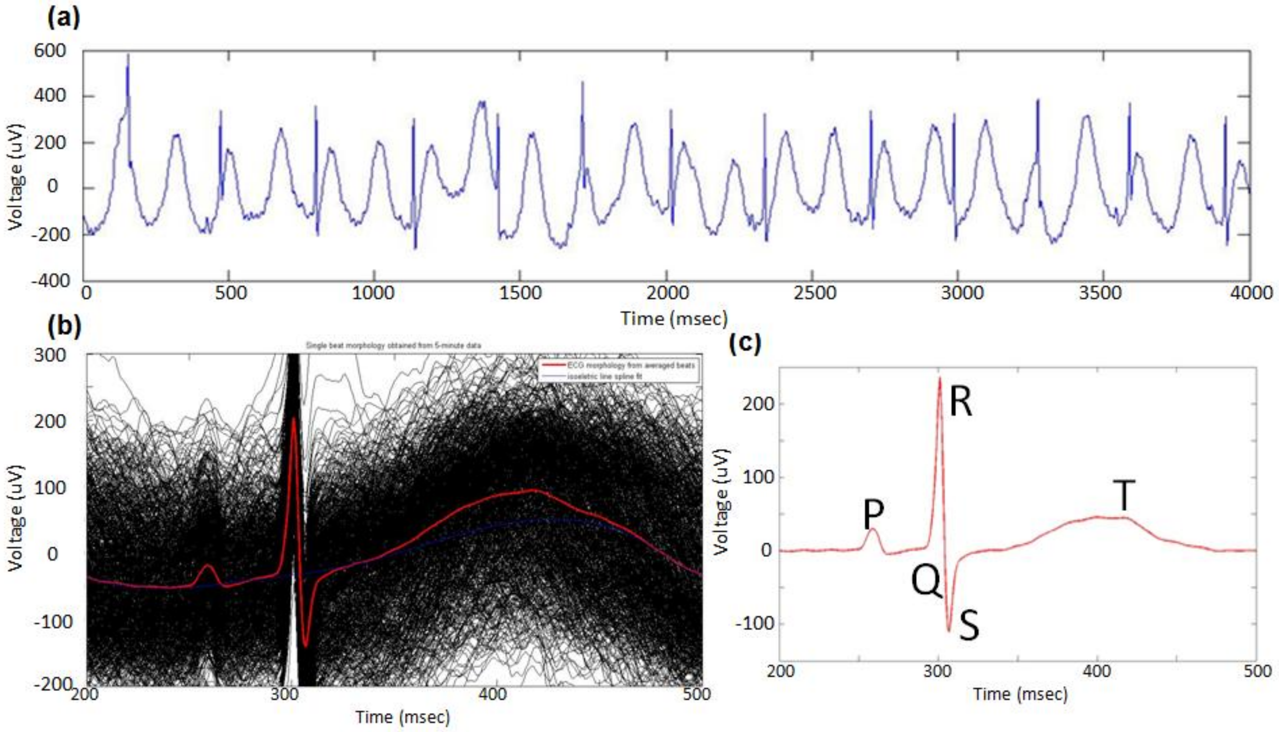

Figure 3. ECG Recording and Signal Processing

(a) Raw data of a representative ECG waveform in the presence of gill motion and low frequency baseline wandering. R waves were detected by using an in-house R wave detection algorithm. Specifically, all of the individual ECG signals were aligned with the peak R waves and were summed together to filter the unsynchronized breathing artifacts and wandering baselines. **(b)** A summed ECG waveform over 5 minutes was highlighted as the red ECG pattern while the black waveforms were the individual ECG signals. **(c)** The residual baseline was then fitted with a cubic spline curve (blue) and subtracted from the summed ECG waveform.

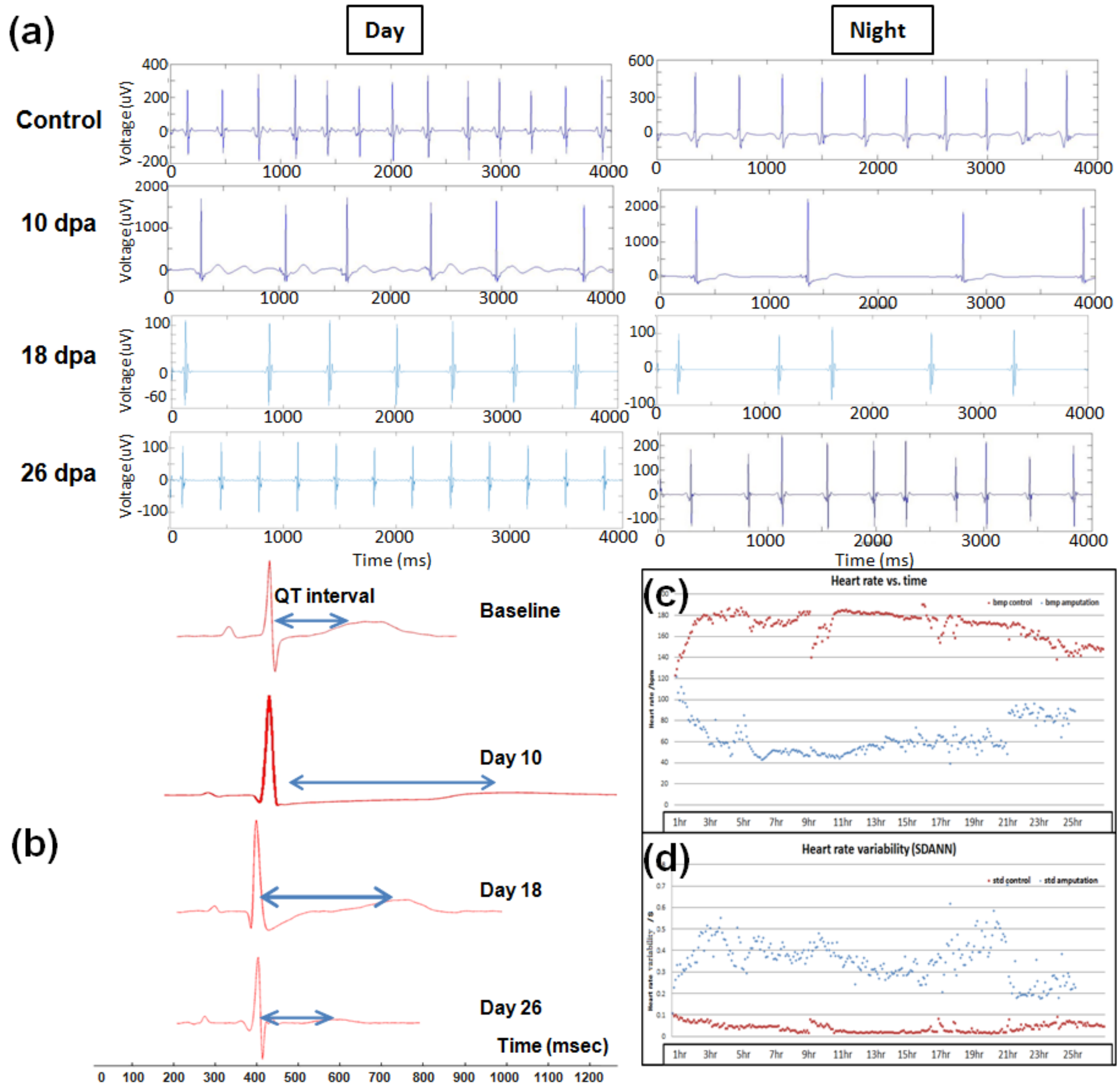

Figure 4. Circadian variation in heart rates.

(a) At day 0 (baseline), the mean heart rate at day time was 192, and at night was 154. At day 10, the mean heart rate at day time was 88, and at night was 51. At day 18, the mean heart rate at day time was 103, and at night was 77. At day 26, the mean heart rate at day time was 168, and at night was 154. At night when fish is resting, the heart rate is slightly slower. However the heart rate difference in the 10 day post surgery case is much more pronounced. At 18 day post surgery, the heart rate has increased and at

26 day post surgery the heart rate has approximately recovered back to normal. **(b)** QT intervals were prolonged in response to ventricular injury at day 10 and 18, followed by normalization at day 26. The ECG monitoring captured the electrical phenotypes to recapitulate the regenerative capacity of adult zebrafish. We applied the R wave detection algorithm to extract all of the heart rate intervals. We calculated the mean heart rates (HR) and heart rate variability (HRV) at every 5 minutes. Next, we plotted the HR and HRV as a function of time for 24 hours. **(c)** Comparison of HR between the sham-treated and the ventricular injury fish over 24 hours at 10 day post resection. Interestingly, HR tends to be higher in the sham group (n=5) **(d)** Comparison of HRV between sham- and amputated-treated animals for 24 hours at 10 day post amputation (dpa). HRV is higher in the amputated than the sham-treaed group (n=5).

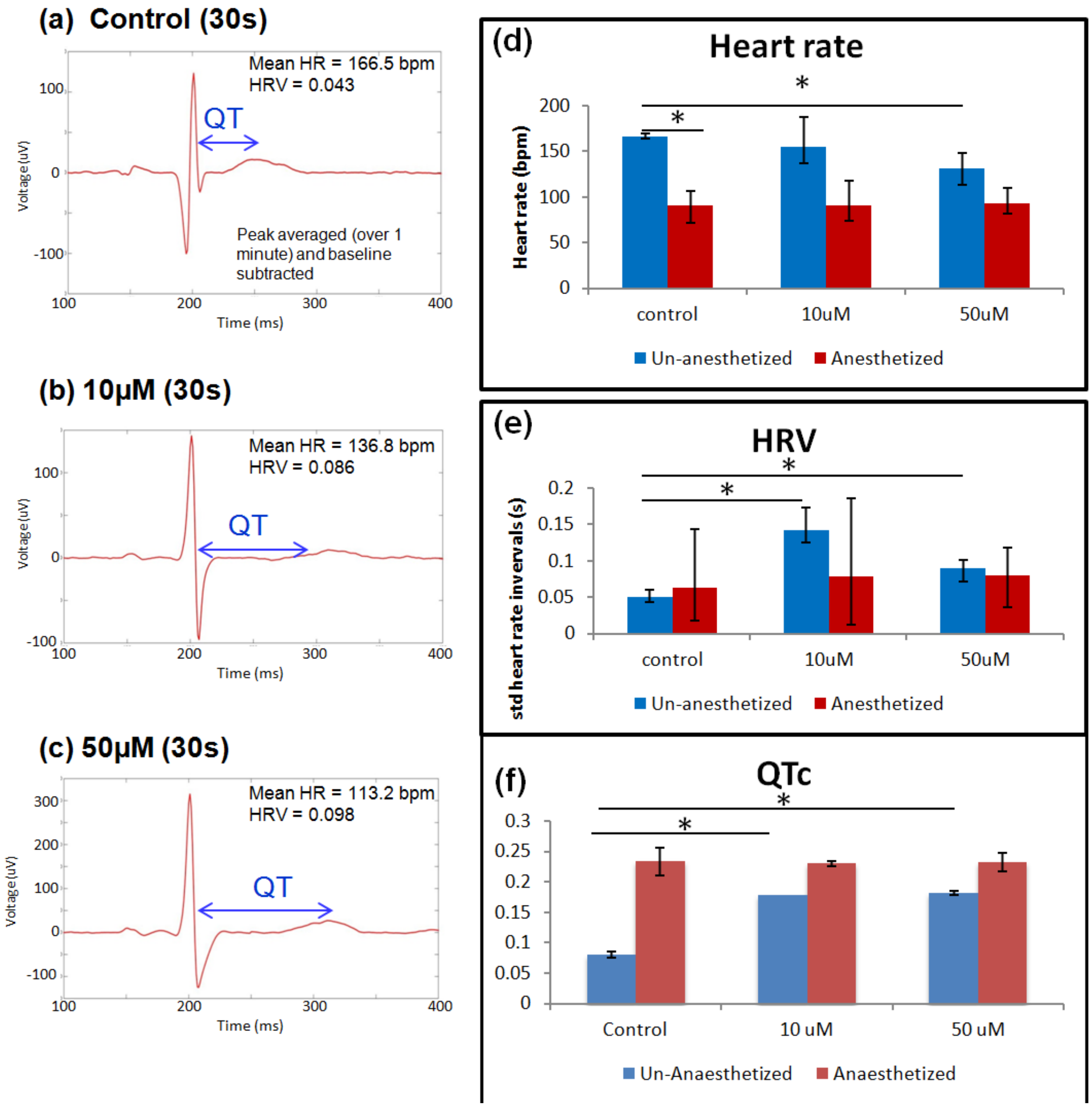

Figure 5. ECG Analysis in response to amiodarone treatment.

The left panels represent the signals obtained from control **(a)**, treatment with 10µM **(b)**, and 50µM **(c)** of Amiodarone in the non-sedated fish (n=5), respectively, to highlight changes in heart rate (HR) and prolonged QT intervals in response to 10µM and 50µM of Amiodarone. **(d)** In the non-sedated animals, the mean HR significantly decreased in response to 50 µM of Amiodarone (* $P < 0.01$, n=3). In the sedated animals, the mean HR is significantly lower than those of non-sedated animals (* $P < 0.01$, n=3), but it is not responsive to an increase in Amiodarone concentration ($P > 0.7$, n=4). **(e)** In the non-sedated animals, HRV is responsive to 10 µM and 50 µM of Amiodarone (* $P < 0.01$, n=3). In the sedated animals, HRV is statistically insignificant ($P > 0.6$, n=4). **(f)** QTc reveals significant change in corrected QT interval between control and both 10µM and 50µM Amiodarone treatment (* $P < 0.05$, n=3).

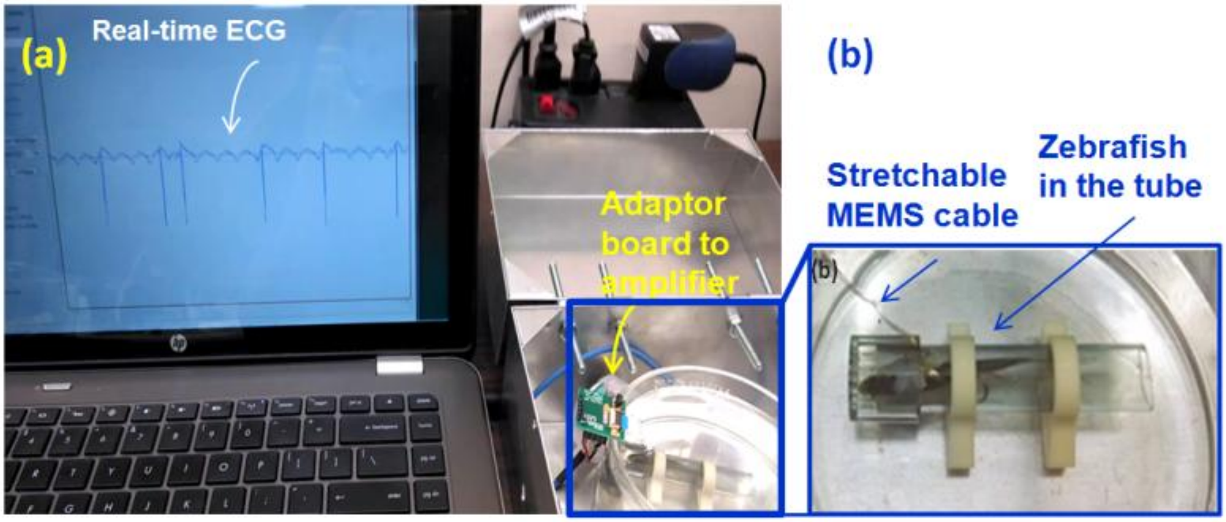

Supplemental Figure 1. ECG Signal Acquisition and Fish Confinement.

The zebrafish was held underwater in a clear tube during measurement to limit mechanical noise from excess muscle movement and prevent tangling of the stretchable MEMS cable over long-term measurements. Signals were acquired real-time.

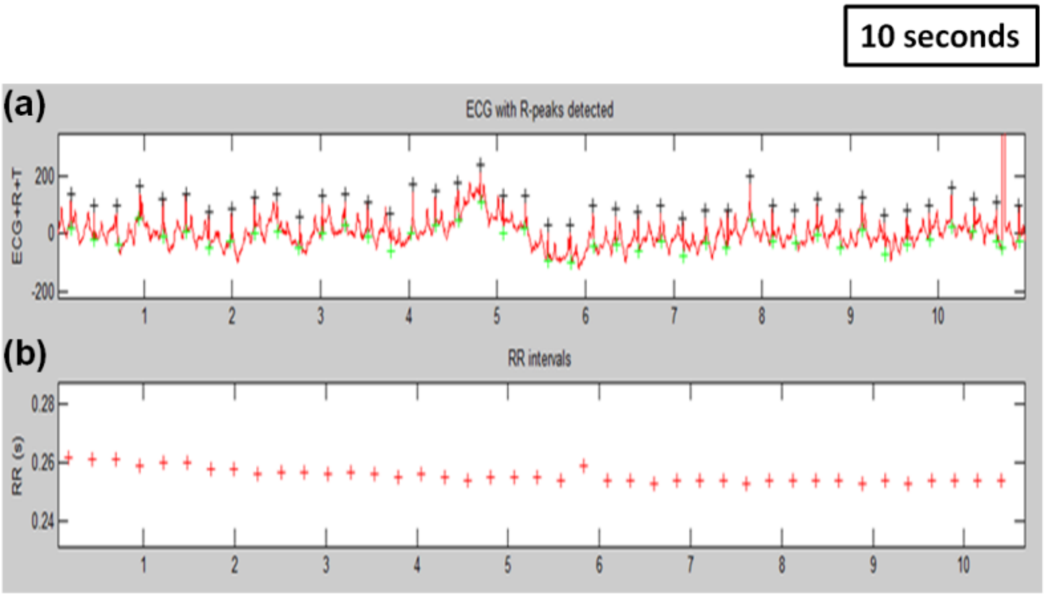

Supplemental Figure 2. R-peak Detection

We used a R-peak detection algorithm to measure heart rate (HR) and heart rate variability (HRV) over time from the acquired ECG signals.

Heart rate (bpm)			
Fish no.	control	10uM	50uM
1	167	137	113
2	169	142	149
3	164	188	133
4			133
5			127
Average	166.7	155.6	131.02
S.D.	2.5	28.1	13.0

Heart rate variability (sec)			
Fish no.	control	10uM	50uM
1	0.043	0.126	0.098
2	0.061	0.173	0.087
3	0.049	0.130	0.101
4			0.072
5			0.096
Average	0.051	0.143	0.091
S.D.	0.0092	0.0261	0.0118

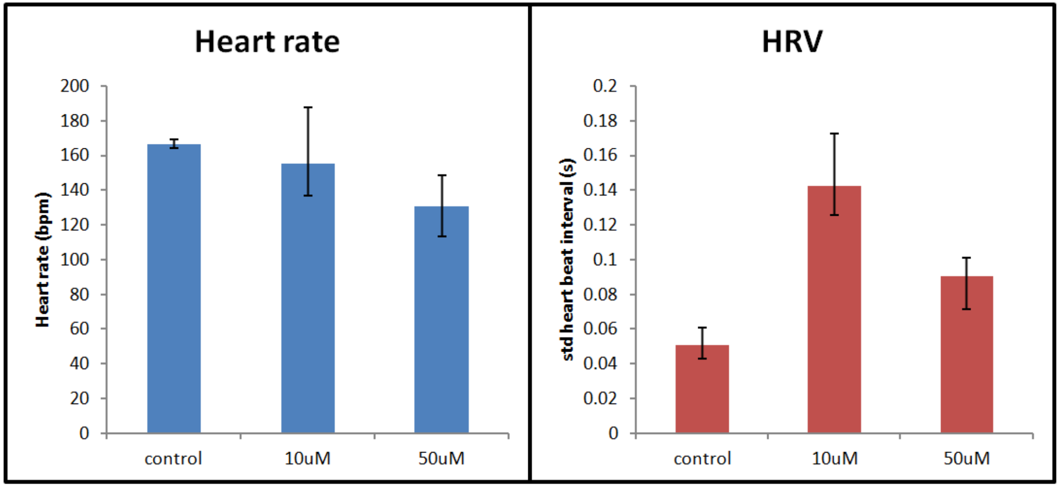

Supplemental Figure 3. Non-Sedated Amiodarone Treatment.

When measured in the absence of sedation, fish treated with Amiodarone experienced decreased heart rate and increased heart rate variability.

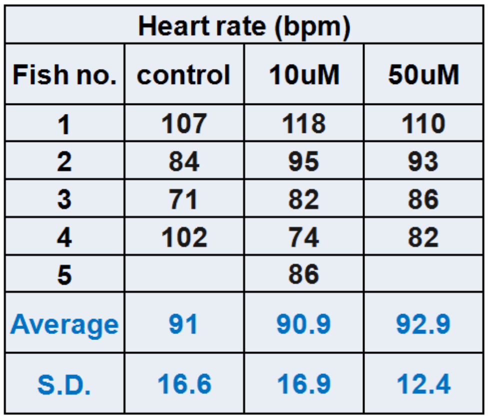

Heart rate (bpm)			
Fish no.	control	10uM	50uM
1	107	118	110
2	84	95	93
3	71	82	86
4	102	74	82
5		86	
Average	91	90.9	92.9
S.D.	16.6	16.9	12.4

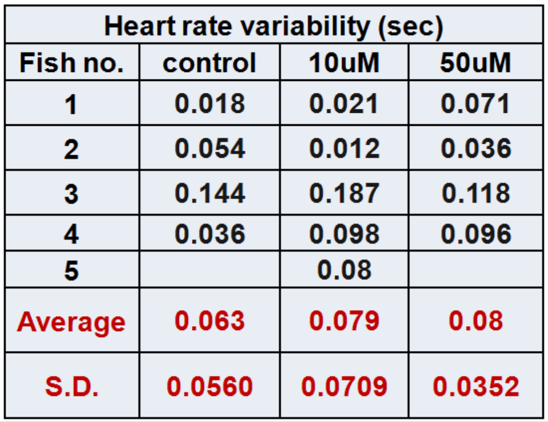

Heart rate variability (sec)			
Fish no.	control	10uM	50uM
1	0.018	0.021	0.071
2	0.054	0.012	0.036
3	0.144	0.187	0.118
4	0.036	0.098	0.096
5		0.08	
Average	0.063	0.079	0.08
S.D.	0.0560	0.0709	0.0352

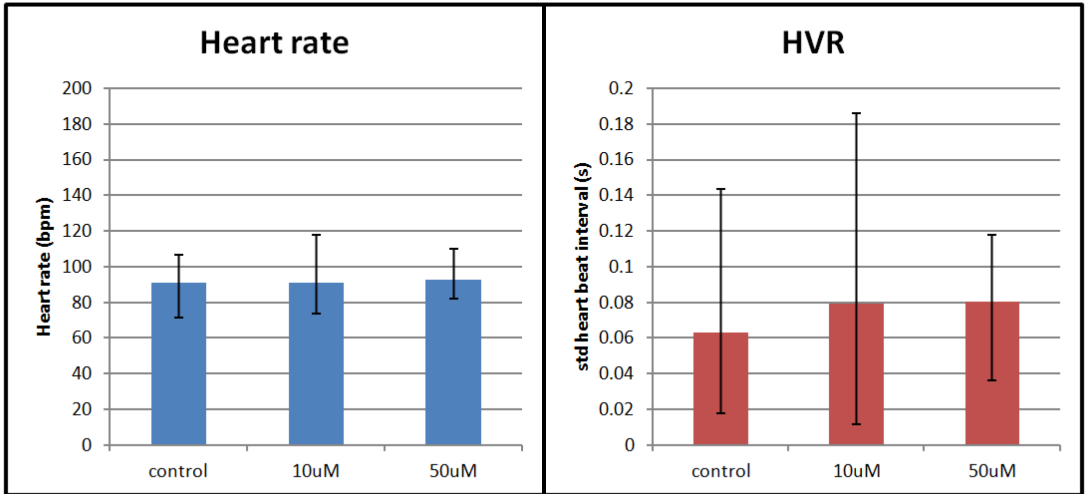

Supplemental Figure 4. Sedated Amiodarone Treatment.

When measured in the presence of sedation using traditional needle electrodes, there was no observed change in heart rate or heart rate variability after treatment with Amiodarone.

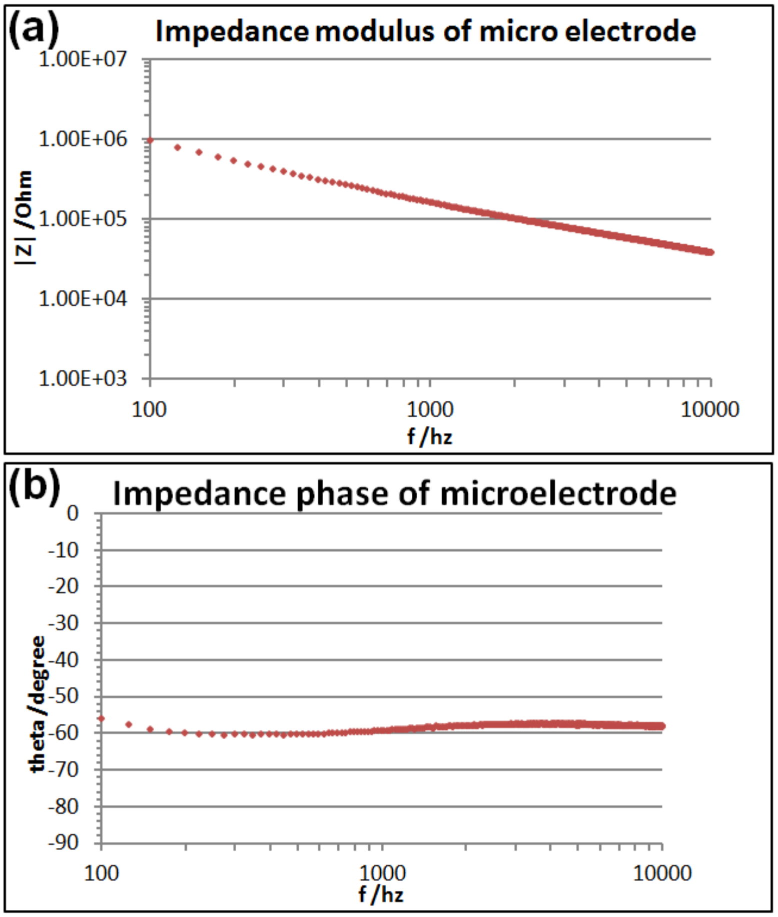

Supplemental Figure 5. Electrode Characterization.

We characterized the impedance of the microelectrode sensor. The total impedance for two microelectrodes in series is approximately 200 Kohm, which is sufficiently below the required 1 Mohm for sufficient sensitivity using our first stage instrumentation amplifier with an input impedance of 10 Mohm at 1 KHz (Intan RHD2000 Amplifier Chip, Los Angeles, USA).

[Supplemental Video Available Online]

Supplemental Video 1. Real-Time Signal Acquisition.

The non-sedated zebrafish is wearing the jacket/microelectrode device while swimming.

ECG signals are acquired and can be observed in real-time.

References

1. Potente, M., et al., *SIRT1 controls endothelial angiogenic functions during vascular growth.* Genes Dev, 2007. 21(20): p. 2644-58.
2. Li, Y.-S.J., J.H. Haga, and S. Chien, *Molecular basis of the effects of shear stress on vascular endothelial cells.* Journal of biomechanics, 2005. 38(10): p. 1949-1971.
3. Ando, J. and K. Yamamoto, *Effects of shear stress and stretch on endothelial function.* Antioxidants & redox signaling, 2011. 15(5): p. 1389-1403.
4. Cheng, C., et al., *Atherosclerotic lesion size and vulnerability are determined by patterns of fluid shear stress.* Circulation, 2006. 113(23): p. 2744-2753.
5. Cunningham, K.S. and A.I. Gotlieb, *The role of shear stress in the pathogenesis of atherosclerosis.* Laboratory investigation, 2005. 85(1): p. 9-23.
6. Davies, P.F., et al., *Influence of hemodynamic forces on vascular endothelial function. In vitro studies of shear stress and pinocytosis in bovine aortic cells.* Journal of Clinical Investigation, 1984. 73(4): p. 1121.
7. Malek, A.M., S.L. Alper, and S. Izumo, *Hemodynamic shear stress and its role in atherosclerosis.* Jama, 1999. 282(21): p. 2035-2042.
8. Wang, H., et al., *Shear stress induces endothelial differentiation from a murine embryonic mesenchymal progenitor cell line.* Arteriosclerosis, thrombosis, and vascular biology, 2005. 25(9): p. 1817-1823.
9. Yamamoto, K., et al., *Proliferation, differentiation, and tube formation by endothelial progenitor cells in response to shear stress.* Journal of Applied Physiology, 2003. 95(5): p. 2081-2088.
10. Hsiai, T.K., et al., *Endothelial cell dynamics under pulsating flows: significance of high versus low shear stress slew rates (∂ τ/∂ τ).* Annals of biomedical engineering, 2002. 30(5): p. 646-656.
11. Harrison, D., et al., *Role of oxidative stress in atherosclerosis.* The American journal of cardiology, 2003. 91(3): p. 7-11.
12. Hsiai, T.K., et al., *Hemodynamics influences vascular peroxynitrite formation: Implication for low-density lipoprotein apo-B-100 nitration.* Free Radical Biology and Medicine, 2007. 42(4): p. 519-529.
13. Sorescu, G.P., et al., *Bone morphogenic protein 4 produced in endothelial cells by oscillatory shear stress induces monocyte adhesion by stimulating reactive oxygen species production from a nox1-based NADPH oxidase.* Circulation research, 2004. 95(8): p. 773-779.
14. Ai, L., et al., *Shear stress influences spatial variations in vascular Mn-SOD expression: implication for LDL nitration.* American Journal of Physiology-Cell Physiology, 2008. 294(6): p. C1576-C1585.
15. Hwang, J., et al., *Pulsatile versus oscillatory shear stress regulates NADPH oxidase subunit expression implication for native LDL oxidation.* Circulation research, 2003. 93(12): p. 1225-1232.
16. Hwang, J., et al., *Oscillatory shear stress stimulates endothelial production of from p47phox-dependent nad (p) h oxidases, leading to monocyte adhesion.* Journal of Biological Chemistry, 2003. 278(47): p. 47291-47298.
17. Nigro, P., J.-i. Abe, and B.C. Berk, *Flow shear stress and atherosclerosis: a matter of site specificity.* Antioxidants & redox signaling, 2011. 15(5): p. 1405-1414.
18. Li, R., et al., *Pulsatile shear stress increased mitochondrial membrane potential: implication of Mn-SOD.* Biochemical and biophysical research communications, 2009. 388(2): p. 406-412.

19. Bagi, Z., et al., *PECAM-1 mediates NO-dependent dilation of arterioles to high temporal gradients of shear stress.* Arteriosclerosis, thrombosis, and vascular biology, 2005. 25(8): p. 1590-1595.
20. Shyy, J.Y.-J. and S. Chien, *Role of integrins in endothelial mechanosensing of shear stress.* Circulation research, 2002. 91(9): p. 769-775.
21. Newman, P.J. and D.K. Newman, *Signal transduction pathways mediated by PECAM-1 New roles for an old molecule in platelet and vascular cell biology.* Arteriosclerosis, thrombosis, and vascular biology, 2003. 23(6): p. 953-964.
22. Conway, D.E., et al., *Fluid shear stress on endothelial cells modulates mechanical tension across VE-cadherin and PECAM-1.* Current Biology, 2013. 23(11): p. 1024-1030.
23. Nilius, B. and G. Droogmans, *Ion channels and their functional role in vascular endothelium.* Physiological reviews, 2001. 81(4): p. 1415-1459.
24. Tarbell, J.M., S.I. Simon, and F.-R.E. Curry, *Mechanosensing at the vascular interface.* Annual review of biomedical engineering, 2014. 16: p. 505-532.
25. Bao, P., et al., *The Role of Vascular Endothelial Growth Factor in Wound Healing.* The Journal of surgical research, 2009. 153(2): p. 347-358.
26. Baldwin, H.S., *Early embryonic vascular development.* Cardiovasc Res, 1996. 31 Spec No: p. E34-45.
27. Weis, S.M. and D.A. Cheresh, *Tumor angiogenesis: molecular pathways and therapeutic targets.* Nat Med, 2011. 17(11): p. 1359-1370.
28. Obi, S., et al., *Fluid shear stress induces arterial differentiation of endothelial progenitor cells.* J Appl Physiol (1985), 2009. 106(1): p. 203-11.
29. Huang, H., et al., *Differentiation from embryonic stem cells to vascular wall cells under in vitro pulsatile flow loading.* J Artif Organs, 2005. 8(2): p. 110-8.
30. Wang, H., et al., *Shear stress induces endothelial differentiation from a murine embryonic mesenchymal progenitor cell line.* Arterioscler Thromb Vasc Biol, 2005. 25(9): p. 1817-23.
31. Yamamoto, K., et al., *Fluid shear stress induces differentiation of Flk-1-positive embryonic stem cells into vascular endothelial cells in vitro.* Am J Physiol Heart Circ Physiol, 2005. 288(4): p. H1915-24.
32. Toh, Y.C. and J. Voldman, *Fluid shear stress primes mouse embryonic stem cells for differentiation in a self-renewing environment via heparan sulfate proteoglycans transduction.* FASEB J, 2011. 25(4): p. 1208-17.
33. Li, Y.S., J.H. Haga, and S. Chien, *Molecular basis of the effects of shear stress on vascular endothelial cells.* J Biomech, 2005. 38(10): p. 1949-71.
34. Ando, J. and K. Yamamoto, *Effects of shear stress and stretch on endothelial function.* Antioxid Redox Signal, 2011. 15(5): p. 1389-403.
35. Davies, P.F., et al., *Influence of hemodynamic forces on vascular endothelial function. In vitro studies of shear stress and pinocytosis in bovine aortic cells.* J Clin Invest, 1984. 73(4): p. 1121-9.
36. De Bock, K., M. Georgiadou, and P. Carmeliet, *Role of endothelial cell metabolism in vessel sprouting.* Cell Metab, 2013. 18(5): p. 634-47.
37. Felcht, M., et al., *Angiopoietin-2 differentially regulates angiogenesis through TIE2 and integrin signaling.* The Journal of Clinical Investigation, 2012. 122(6): p. 1991-2005.
38. Fagiani, E. and G. Christofori, *Angiopoietins in angiogenesis.* Cancer Lett, 2013. 328(1): p. 18-26.
39. Fiedler, U. and H.G. Augustin, *Angiopoietins: a link between angiogenesis and inflammation.* Trends Immunol, 2006. 27(12): p. 552-8.

40. **Gale, N.W., et al., *Angiopoietin-2 Is Required for Postnatal Angiogenesis and Lymphatic Patterning, and Only the Latter Role Is Rescued by Angiopoietin-1.* Developmental Cell, 2002. 3(3): p. 411-423.**
41. **Tressel, S.L., et al., *Laminar shear inhibits tubule formation and migration of endothelial cells by an angiopoietin-2 dependent mechanism.* Arterioscler Thromb Vasc Biol, 2007. 27(10): p. 2150-6.**
42. **Ahmed, A., et al., *Angiopoietin-2 confers Atheroprotection in apoE-/- mice by inhibiting LDL oxidation via nitric oxide.* Circ Res, 2009. 104(12): p. 1333-6.**
43. **Ahmed, A. and T. Fujisawa, *Multiple roles of angiopoietins in atherogenesis.* Curr Opin Lipidol, 2011. 22(5): p. 380-5.**
44. **Thomas, M. and H.G. Augustin, *The role of the Angiopoietins in vascular morphogenesis.* Angiogenesis, 2009. 12(2): p. 125-37.**
45. **Felcht, M., et al., *Angiopoietin-2 differentially regulates angiogenesis through TIE2 and integrin signaling.* J Clin Invest, 2012. 122(6): p. 1991-2005.**
46. **Korff, T., et al., *Angiopoietin-1 mediates inhibition of hypertension-induced release of angiopoietin-2 from endothelial cells.* Cardiovasc Res, 2012. 94(3): p. 510-8.**
47. **Resnick, N. and M.A. Gimbrone, Jr., *Hemodynamic forces are complex regulators of endothelial gene expression.* FASEB J, 1995. 9(10): p. 874-82.**
48. **Hwang, J., et al., *Pulsatile versus oscillatory shear stress regulates NADPH oxidase subunit expression: implication for native LDL oxidation.* Circ Res, 2003. 93(12): p. 1225-32.**
49. **Conway, D.E., et al., *Endothelial metallothionein expression and intracellular free zinc levels are regulated by shear stress.* Am J Physiol Cell Physiol, 2010. 299(6): p. C1461-7.**
50. **Hwang, J., et al., *Oscillatory shear stress stimulates endothelial production of O2- from p47phox-dependent NAD(P)H oxidases, leading to monocyte adhesion.* J Biol Chem, 2003. 278(47): p. 47291-8.**
51. **Chatzizisis, Y.S., et al., *Role of endothelial shear stress in the natural history of coronary atherosclerosis and vascular remodeling: molecular, cellular, and vascular behavior.* J Am Coll Cardiol, 2007. 49(25): p. 2379-93.**
52. **Tressel, S.L., et al., *Angiopoietin-2 stimulates blood flow recovery after femoral artery occlusion by inducing inflammation and arteriogenesis.* Arterioscler Thromb Vasc Biol, 2008. 28(11): p. 1989-95.**
53. **Patti, G.J., O. Yanes, and G. Siuzdak, *Metabolomics: the apogee of the omic triology.* Nature reviews. Molecular cell biology, 2012. 13(4): p. 263-269.**
54. **Fiehn, O., *Metabolomics--the link between genotypes and phenotypes.* Plant Mol Biol, 2002. 48(1-2): p. 155-71.**
55. **Fiehn, O., *Combining Genomics, Metabolome Analysis, and Biochemical Modelling to Understand Metabolic Networks.* Comparative and Functional Genomics, 2001. 2(3): p. 155-168.**
56. **Bino, R.J., et al., *Potential of metabolomics as a functional genomics tool.* Trends in Plant Science, 2004. 9(9): p. 418-425.**
57. **Cairns, R.A., I.S. Harris, and T.W. Mak, *Regulation of cancer cell metabolism.* Nat Rev Cancer, 2011. 11(2): p. 85-95.**
58. **Luni, C., J.D. Marth, and F.J. Doyle, III, *Computational Modeling of Glucose Transport in Pancreatic β-Cells Identifies Metabolic Thresholds and Therapeutic Targets in Diabetes.* PLoS ONE, 2012. 7(12): p. e53130.**
59. ***Parkinson disease: Metablomics study reveals novel biomarkers for PD.* Nat Rev Neurol, 2013. 9(9): p. 484-484.**

60. Clyne, M., *Kidney cancer: Metabolomics for targeted therapy.* Nat Rev Urol, 2012. 9(7): p. 355-355.
61. *Stroke: Molecular markers could help predict stroke risk after TIA.* Nat Rev Neurol, 2015. 11(1): p. 3-3.
62. Kluge, M.A., J.L. Fetterman, and J.A. Vita, *Mitochondria and endothelial function.* Circ Res, 2013. 112(8): p. 1171-88.
63. Sun, X. and M.W. Feinberg, *Regulation of endothelial cell metabolism: just go with the flow.* Arterioscler Thromb Vasc Biol, 2015. 35(1): p. 13-5.
64. Wang, Y., et al., *Regulation of VEGF-induced endothelial cell migration by mitochondrial reactive oxygen species.* Am J Physiol Cell Physiol, 2011. 301(3): p. C695-704.
65. Culic, O., M.L. Gruwel, and J. Schrader, *Energy turnover of vascular endothelial cells.* Am J Physiol, 1997. 273(1 Pt 1): p. C205-13.
66. Mertens, S., et al., *Energetic response of coronary endothelial cells to hypoxia.* Am J Physiol, 1990. 258(3 Pt 2): p. H689-94.
67. De Bock, K., et al., *Role of PFKFB3-driven glycolysis in vessel sprouting.* Cell, 2013. 154(3): p. 651-63.
68. Suarez, J. and R. Rubio, *Regulation of glycolytic flux by coronary flow in guinea pig heart. Role of vascular endothelial cell glycocalyx.* Am J Physiol, 1991. 261(6 Pt 2): p. H1994-2000.
69. Schoors, S., et al., *Partial and transient reduction of glycolysis by PFKFB3 blockade reduces pathological angiogenesis.* Cell Metab, 2014. 19(1): p. 37-48.
70. Wang, S., et al., *P2Y2 and Gq/G11 control blood pressure by mediating endothelial mechanotransduction.* J Clin Invest, 2015. 125(8): p. 3077-86.
71. Jones, R., et al., *Molecular beacons can assess changes in expression and 3'-polyadenylation of human eNOS mRNA.* Am J Physiol Cell Physiol, 2009. 296(3): p. C498-504.
72. Inagaki, K., et al., *Cardioprotection by epsilon-protein kinase C activation from ischemia: continuous delivery and antiarrhythmic effect of an epsilon-protein kinase C-activating peptide.* Circulation, 2005. 111(1): p. 44-50.
73. Budas, G., et al., *Identification of epsilonPKC targets during cardiac ischemic injury.* Circ J, 2012. 76(6): p. 1476-85.
74. Cross, H.R., et al., *Expression of activated PKC epsilon (PKC epsilon) protects the ischemic heart, without attenuating ischemic H(+) production.* J Mol Cell Cardiol, 2002. 34(3): p. 361-7.
75. Edmondson, R.D., et al., *Protein kinase C epsilon signaling complexes include metabolism- and transcription/translation-related proteins: complimentary separation techniques with LC/MS/MS.* Mol Cell Proteomics, 2002. 1(6): p. 421-33.
76. Mayr, M., et al., *Proteomic and metabolomic analysis of cardioprotection: Interplay between protein kinase C epsilon and delta in regulating glucose metabolism of murine hearts.* J Mol Cell Cardiol, 2009. 46(2): p. 268-77.
77. Rask-Madsen, C. and G.L. King, *Differential regulation of VEGF signaling by PKC-alpha and PKC-epsilon in endothelial cells.* Arterioscler Thromb Vasc Biol, 2008. 28(5): p. 919-24.
78. Carracedo, S., et al., *Redundant role of protein kinase C delta and epsilon during mouse embryonic development.* PLoS One, 2014. 9(8): p. e103686.
79. Koh, W., et al., *Formation of endothelial lumens requires a coordinated PKCepsilon-, Src-, Pak- and Raf-kinase-dependent signaling cascade downstream of Cdc42 activation.* J Cell Sci, 2009. 122(Pt 11): p. 1812-22.
80. Nisoli, E., et al., *Defective mitochondrial biogenesis: a hallmark of the high cardiovascular risk in the metabolic syndrome?* Circ Res, 2007. 100(6): p. 795-806.
81. Addabbo, F., et al., *The Krebs cycle and mitochondrial mass are early victims of endothelial dysfunction: proteomic approach.* Am J Pathol, 2009. 174(1): p. 34-43.

82. Madamanchi, N.R., A. Vendrov, and M.S. Runge, *Oxidative stress and vascular disease.* Arterioscler Thromb Vasc Biol, 2005. 25(1): p. 29-38.
83. Yu, E., J. Mercer, and M. Bennett, *Mitochondria in vascular disease.* Cardiovasc Res, 2012. 95(2): p. 173-82.
84. Darley-Usmar, V., *The powerhouse takes control of the cell; the role of mitochondria in signal transduction.* Free Radic Biol Med, 2004. 37(6): p. 753-4.
85. Widlansky, M.E. and D.D. Gutterman, *Regulation of endothelial function by mitochondrial reactive oxygen species.* Antioxid Redox Signal, 2011. 15(6): p. 1517-30.
86. Giordano, F.J., *Oxygen, oxidative stress, hypoxia, and heart failure.* J Clin Invest, 2005. 115(3): p. 500-8.
87. Griendling, K.K. and G.A. FitzGerald, *Oxidative stress and cardiovascular injury: Part II: animal and human studies.* Circulation, 2003. 108(17): p. 2034-40.
88. Sorescu, D., et al., *Superoxide production and expression of nox family proteins in human atherosclerosis.* Circulation, 2002. 105(12): p. 1429-35.
89. Hsiai, T.K., et al., *Hemodynamics influences vascular peroxynitrite formation: Implication for low-density lipoprotein apo-B-100 nitration.* Free Radic Biol Med, 2007. 42(4): p. 519-29.
90. Gorlach, A., et al., *A gp91phox containing NADPH oxidase selectively expressed in endothelial cells is a major source of oxygen radical generation in the arterial wall.* Circ Res, 2000. 87(1): p. 26-32.
91. Chen, K., et al., *Mitochondrial function is required for hydrogen peroxide-induced growth factor receptor transactivation and downstream signaling.* J Biol Chem, 2004. 279(33): p. 35079-86.
92. Connor, K.M., et al., *Mitochondrial H2O2 regulates the angiogenic phenotype via PTEN oxidation.* J Biol Chem, 2005. 280(17): p. 16916-24.
93. Hughes, G., M.P. Murphy, and E.C. Ledgerwood, *Mitochondrial reactive oxygen species regulate the temporal activation of nuclear factor kappaB to modulate tumour necrosis factor-induced apoptosis: evidence from mitochondria-targeted antioxidants.* Biochem J, 2005. 389(Pt 1): p. 83-9.
94. Ballinger, S.W., *Mitochondrial dysfunction in cardiovascular disease.* Free Radic Biol Med, 2005. 38(10): p. 1278-95.
95. Ong, S.B., A.R. Hall, and D.J. Hausenloy, *Mitochondrial dynamics in cardiovascular health and disease.* Antioxid Redox Signal, 2013. 19(4): p. 400-14.
96. Sobenin, I.A., et al., *Changes of mitochondria in atherosclerosis: possible determinant in the pathogenesis of the disease.* Atherosclerosis, 2013. 227(2): p. 283-8.
97. Korshunov, S.S., V.P. Skulachev, and A.A. Starkov, *High protonic potential actuates a mechanism of production of reactive oxygen species in mitochondria.* FEBS Lett, 1997. 416(1): p. 15-8.
98. Lee, I., E. Bender, and B. Kadenbach, *Control of mitochondrial membrane potential and ROS formation by reversible phosphorylation of cytochrome c oxidase.* Mol Cell Biochem, 2002. 234-235(1-2): p. 63-70.
99. Chen, L.B., *Mitochondrial membrane potential in living cells.* Annu Rev Cell Biol, 1988. 4: p. 155-81.
100. Duchen, M.R., A. Surin, and J. Jacobson, *Imaging mitochondrial function in intact cells.* Methods Enzymol, 2003. 361: p. 353-89.
101. Liberman, E.A., et al., *Mechanism of coupling of oxidative phosphorylation and the membrane potential of mitochondria.* Nature, 1969. 222(5198): p. 1076-8.
102. Senior, A.E., *ATP synthesis by oxidative phosphorylation.* Physiol Rev, 1988. 68(1): p. 177-231.

103. Beltran, B., et al., *The effect of nitric oxide on cell respiration: A key to understanding its role in cell survival or death.* Proc Natl Acad Sci U S A, 2000. 97(26): p. 14602-7.

104. Hausenloy, D.J. and D.M. Yellon, *The mitochondrial permeability transition pore: its fundamental role in mediating cell death during ischaemia and reperfusion.* J Mol Cell Cardiol, 2003. 35(4): p. 339-41.

105. Kudo, S., et al., *Shear-stress effect on mitochondrial membrane potential and albumin uptake in cultured endothelial cells.* Biochem Biophys Res Commun, 2000. 270(2): p. 616-21.

106. Abid, M.R., et al., *Vascular endothelial growth factor-mediated induction of manganese superoxide dismutase occurs through redox-dependent regulation of forkhead and IkappaB/NF-kappaB.* J Biol Chem, 2004. 279(42): p. 44030-8.

107. Inoue, N., et al., *Shear Stress Modulates Expression of Cu/Zn Superoxide Dismutase in Human Aortic Endothelial Cells.* Circulation Research, 1996. 79(1): p. 32-37.

108. Staton, C.A., M.W.R. Reed, and N.J. Brown, *A critical analysis of current in vitro and in vivo angiogenesis assays.* International Journal of Experimental Pathology, 2009. 90(3): p. 195-221.

109. Isogai, S., M. Horiguchi, and B.M. Weinstein, *The vascular anatomy of the developing zebrafish: an atlas of embryonic and early larval development.* Developmental biology, 2001. 230(2): p. 278-301.

110. Gore, A.V., et al., *Vascular Development in the Zebrafish.* Cold Spring Harbor Perspectives in Medicine, 2012. 2(5): p. a006684.

111. Sun, P., et al., *Micro-electrocardiograms to study post-ventricular amputation of zebrafish heart.* Ann Biomed Eng, 2009. 37(5): p. 890-901.

112. Pardo-Martin, C., et al., *High-throughput in vivo vertebrate screening.* Nat Meth, 2010. 7(8): p. 634-636.

113. Varshney, G.K., et al., *High-throughput gene targeting and phenotyping in zebrafish using CRISPR/Cas9.* Genome Research, 2015.

114. Miscevic, F., O. Rotstein, and X.Y. Wen, *Advances in zebrafish high content and high throughput technologies.* Comb Chem High Throughput Screen, 2012. 15(7): p. 515-21.

115. Wang, G., et al., *First quantitative high-throughput screen in zebrafish identifies novel pathways for increasing pancreatic β-cell mass.* eLife, 2015.

116. Gaj, T., C.A. Gersbach, and C.F. Barbas, 3rd, *ZFN, TALEN, and CRISPR/Cas-based methods for genome engineering.* Trends Biotechnol, 2013. 31(7): p. 397-405.

117. Yelon, D., *Cardiac patterning and morphogenesis in zebrafish.* Dev Dyn, 2001. 222(4): p. 552-63.

118. Liu, J. and D.Y.R. Stainier, *Zebrafish in the Study of Early Cardiac Development.* Circulation Research, 2012. 110(6): p. 870-874.

119. Bakkers, J., *Zebrafish as a model to study cardiac development and human cardiac disease.* Cardiovascular Research, 2011.

120. Stainier, D.Y., R.K. Lee, and M.C. Fishman, *Cardiovascular development in the zebrafish. I. Myocardial fate map and heart tube formation.* Development, 1993. 119(1): p. 31-40.

121. Nguyen, C.T., et al., *Zebrafish as a model for cardiovascular development and disease.* Drug discovery today. Disease models, 2008. 5(3): p. 135-140.

122. Li, R., et al., *Shear stress-activated Wnt-angiopoietin-2 signaling recapitulates vascular repair in zebrafish embryos.* Arterioscler Thromb Vasc Biol, 2014. 34(10): p. 2268-75.

123. Poss, K.D., L.G. Wilson, and M.T. Keating, *Heart Regeneration in Zebrafish.* Science, 2002. 298(5601): p. 2188-2190.

124. Kikuchi, K., et al., *Primary contribution to zebrafish heart regeneration by gata4+ cardiomyocytes.* Nature, 2010. 464(7288): p. 601-605.

125. Kikuchi, K., *Advances in understanding the mechanism of zebrafish heart regeneration.* Stem Cell Research, 2014. 13(3, Part B): p. 542-555.

126. Ai, L., et al., *Real-time intravascular shear stress in the rabbit abdominal aorta.* IEEE Trans Biomed Eng, 2009. 56(6): p. 1755-64.

127. Ai, L., et al., *Optimization of intravascular shear stress assessment in vivo.* J Biomech, 2009. 42(10): p. 1429-37.

128. Rodger, D.C., et al. *High-Density Flexible Parylene-Based Multielectrode Arrays for Retinal and Spinal Cord Stimulation*. in *Solid-State Sensors, Actuators and Microsystems Conference, 2007. TRANSDUCERS 2007. International*. 2007.

129. Cao, H., et al., *Wearable multi-channel microelectrode membranes for elucidating electrophysiological phenotypes of injured myocardium.* Integr Biol (Camb), 2014. 6(8): p. 789-95.

130. Viventi, J., et al., *A conformal, bio-interfaced class of silicon electronics for mapping cardiac electrophysiology.* Sci Transl Med, 2010. 2(24): p. 24ra22.

131. Viventi, J., et al., *Flexible, foldable, actively multiplexed, high-density electrode array for mapping brain activity in vivo.* Nat Neurosci, 2011. 14(12): p. 1599-605.

132. Gibert, Y., M.C. Trengove, and A.C. Ward, *Zebrafish as a genetic model in pre-clinical drug testing and screening.* Curr Med Chem, 2013. 20(19): p. 2458-66.

133. Zhang de, L., et al., *Antioxidative responses in zebrafish liver exposed to sublethal doses Aphanizomenon flos-aquae DC-1 aphantoxins.* Ecotoxicol Environ Saf, 2015. 113: p. 425-32.

134. Whitmore, D., et al., *Zebrafish Clock rhythmic expression reveals independent peripheral circadian oscillators.* Nat Neurosci, 1998. 1(8): p. 701-7.

135. Milan, D.J., et al., *In vivo recording of adult zebrafish electrocardiogram and assessment of drug-induced QT prolongation.* Am J Physiol Heart Circ Physiol, 2006. 291(1): p. H269-73.

136. Yu, F., et al., *Electrocardiogram signals to assess zebrafish heart regeneration: implication of long QT intervals.* Ann Biomed Eng, 2010. 38(7): p. 2346-57.

137. Lee, J., et al., *Hemodynamics and ventricular function in a zebrafish model of injury and repair.* Zebrafish, 2014. 11(5): p. 447-54.

138. Yamamoto, K., et al., *Fluid shear stress induces differentiation of Flk-1-positive embryonic stem cells into vascular endothelial cells in vitro.* American Journal of Physiology-Heart and Circulatory Physiology, 2005. 288(4): p. H1915-H1924.

139. Obi, S., et al., *Fluid shear stress induces arterial differentiation of endothelial progenitor cells.* Journal of Applied Physiology, 2009. 106(1): p. 203-211.

140. Toh, Y.-C. and J. Voldman, *Fluid shear stress primes mouse embryonic stem cells for differentiation in a self-renewing environment via heparan sulfate proteoglycans transduction.* The FASEB Journal, 2011. 25(4): p. 1208-1217.

141. Huang, H., et al., *Differentiation from embryonic stem cells to vascular wall cells under in vitro pulsatile flow loading.* J Artif Organs, 2005. 8(2): p. 110-118.

142. Wang, H., et al., *Shear Stress Induces Endothelial Differentiation From a Murine Embryonic Mesenchymal Progenitor Cell Line.* Arterioscler. Thromb. Vasc. Biol., 2005. 25: p. 1817 - 1823.

143. Tressel, S.L., et al., *Laminar Shear Inhibits Tubule Formation and Migration of Endothelial Cells by an Angiopoietin-2–Dependent Mechanism.* Arteriosclerosis, thrombosis, and vascular biology, 2007. 27(10): p. 2150-2156.

144. Ahmed, A., et al., *Angiopoietin-2 confers atheroprotection in apoE−/− mice by inhibiting LDL oxidation via nitric oxide.* Circulation research, 2009. 104(12): p. 1333-1336.

145. Ahmed, A. and T. Fujisawa, *Multiple roles of angiopoietins in atherogenesis.* Current Opinion in Lipidology, 2011. 22(5): p. 380-385.

146. Thomas, M. and H.G. Augustin, *The role of the Angiopoietins in vascular morphogenesis.* Angiogenesis, 2009. 12(2): p. 125-137.
147. Felcht, M., et al., *Angiopoietin-2 differentially regulates angiogenesis through TIE2 and integrin signaling.* The Journal of Clinical Investigation, 2012. 122(6): p. 1991.
148. Korff, T., et al., *Angiopoietin-1 mediates inhibition of hypertension-induced release of angiopoietin-2 from endothelial cells.* Cardiovascular research, 2012. 94(3): p. 510-518.
149. Resnick, N. and M. Gimbrone, *Hemodynamic forces are complex regulators of endothelial gene expression.* The FASEB Journal, 1995. 9(10): p. 874-882.
150. Hwang, J., et al., *Pulsatile versus oscillatory shear stress regulates NADPH oxidase subunit expression: implication for native LDL oxidation.* Circulation research, 2003. 93(12): p. 1225-1232.
151. Conway, D.E., et al., *Endothelial metallothionein expression and intracellular free zinc levels are regulated by shear stress.* American Journal of Physiology-Cell Physiology, 2010. 299(6): p. C1461-C1467.
152. Chatzizisis, Y.S., et al., *Role of endothelial shear stress in the natural history of coronary atherosclerosis and vascular remodeling: molecular, cellular, and vascular behavior.* Journal of the American College of Cardiology, 2007. 49(25): p. 2379-2393.
153. Tressel, S.L., et al., *Angiopoietin-2 stimulates blood flow recovery after femoral artery occlusion by inducing inflammation and arteriogenesis.* Arteriosclerosis, thrombosis, and vascular biology, 2008. 28(11): p. 1989-1995.
154. Logan, C.Y. and R. Nusse, *The Wnt signaling pathway in development and disease.* Annu Rev Cell Dev Biol, 2004. 20: p. 781-810.
155. Jen, N., et al., *Atrial fibrillation pacing decreases intravascular shear stress in a New Zealand white rabbit model: implications in endothelial function.* Biomechanics and Modeling in Mechanobiology, 2012: p. 1-11.
156. Fuerer, C. and R. Nusse, *Lentiviral vectors to probe and manipulate the Wnt signaling pathway.* PLoS One, 2010. 5(2): p. e9370.
157. Li, R., et al., *Ultra fine particles from diesel engines induce vascular oxidative stress via JNK activation.* Free radical biology & medicine, 2009. 46(6): p. 775-782.
158. Susa, M., et al., *Inhibition of ABCB1 (MDR1) expression by an siRNA nanoparticulate delivery system to overcome drug resistance in osteosarcoma.* PLoS One, 2010. 5(5): p. e10764.
159. MacDonald, B.T., K. Tamai, and X. He, *Wnt/β-catenin signaling: components, mechanisms, and diseases.* Developmental cell, 2009. 17(1): p. 9-26.
160. Lin, G. and J.M. Slack, *Requirement for Wnt and FGF signaling in Xenopus tadpole tail regeneration.* Developmental biology, 2008. 316(2): p. 323-335.
161. Chen, B., et al., *Small molecule–mediated disruption of WNT-dependent signaling in tissue regeneration and cancer.* Nature chemical biology, 2009. 5(2): p. 100-107.
162. Kwon, C., et al., *Canonical Wnt signaling is a positive regulator of mammalian cardiac progenitors.* Proc Natl Acad Sci U S A, 2007. 104(26): p. 10894-9.
163. Camenisch, T.D., et al., *Disruption of hyaluronan synthase-2 abrogates normal cardiac morphogenesis and hyaluronan-mediated transformation of epithelium to mesenchyme.* J Clin Invest, 2000. 106(3): p. 349-60.
164. Vijayaragavan, K. and M. Bhatia, *Early cardiac development: a Wnt beat away.* Proc Natl Acad Sci U S A, 2007. 104(23): p. 9549-50.
165. Galli, L.M., et al., *Differential inhibition of Wnt-3a by Sfrp-1, Sfrp-2, and Sfrp-3.* Dev Dyn, 2006. 235(3): p. 681-90.
166. Niida, A., et al., *DKK1, a negative regulator of Wnt signaling, is a target of the beta-catenin/TCF pathway.* Oncogene, 2004. 23(52): p. 8520-6.

167. Park, C.H., et al., *Ionomycin downregulates β-catenin/Tcf signaling in colon cancer cell line.* Carcinogenesis, 2005. 26(11): p. 1929-1933.

168. Park, C.H., et al., *Ionomycin downregulates beta-catenin/Tcf signaling in colon cancer cell line.* Carcinogenesis, 2005. 26(11): p. 1929-33.

169. Goettsch, W., et al., *Flow-dependent regulation of angiopoietin-2.* Journal of cellular physiology, 2008. 214(2): p. 491-503.

170. Chlench, S., et al., *Regulation of Foxo-1 and the angiopoietin-2/Tie2 system by shear stress.* FEBS letters, 2007. 581(4): p. 673-680.

171. Mochizuki, Y., et al., *Angiopoietin 2 stimulates migration and tube-like structure formation of murine brain capillary endothelial cells through c-Fes and c-Fyn.* J Cell Sci, 2002. 115(Pt 1): p. 175-83.

172. Maisonpierre, P.C., et al., *Angiopoietin-2, a natural antagonist for Tie2 that disrupts in vivo angiogenesis.* Science, 1997. 277(5322): p. 55-60.

173. Li, R., et al., *Angiopoeitin-2 modulates Survivin expression in OxLDL-induced endothelial cell apoptosis.* Biochemical and Biophysical Research Communications, 2011. 417(1): p. 619-622.

174. Etoh, T., et al., *Angiopoietin-2 is related to tumor angiogenesis in gastric carcinoma: possible in vivo regulation via induction of proteases.* Cancer Res, 2001. 61(5): p. 2145-53.

175. Silha, J.V., et al., *Angiogenic factors are elevated in overweight and obese individuals.* Int J Obes (Lond), 2005. 29(11): p. 1308-14.

176. Ziegler, T., et al., *Angiopoietin 2 mediates microvascular and hemodynamic alterations in sepsis.* The Journal of Clinical Investigation, 2013. 123(8): p. 3436.

177. Kubota, Y., et al., *Cooperative interaction of Angiopoietin-like proteins 1 and 2 in zebrafish vascular development.* Proceedings of the National Academy of Sciences of the United States of America, 2005. 102(38): p. 13502-13507.

178. Zheng, P.-P., et al., *Circulation status of subintestinal vessels is a sensitive parameter for monitoring suboptimal systemic circulation in experimental zebrafish embryos.* Cell Cycle, 2009. 8(22): p. 3782-3783.

179. Zarins, C.K., et al., *Carotid bifurcation atherosclerosis. Quantitative correlation of plaque localization with flow velocity profiles and wall shear stress.* Circ Res, 1983. 53(4): p. 502-14.

180. DePaola, N., et al., *Vascular endothelium responds to fluid shear stress gradients.* Arterioscler Thromb, 1992. 12(11): p. 1254-7.

181. Dewey, C.F., Jr., et al., *The dynamic response of vascular endothelial cells to fluid shear stress.* J Biomech Eng, 1981. 103(3): p. 177-85.

182. Frangos, J.A., T.Y. Huang, and C.B. Clark, *Steady shear and step changes in shear stimulate endothelium via independent mechanisms--superposition of transient and sustained nitric oxide production.* Biochem Biophys Res Commun, 1996. 224(3): p. 660-5.

183. Chiu, J.J., et al., *Effects of disturbed flow on endothelial cells.* J Biomech Eng, 1998. 120(1): p. 2-8.

184. Milkiewicz, M., et al., *Association between shear stress, angiogenesis, and VEGF in skeletal muscles in vivo.* Microcirculation, 2001. 8(4): p. 229-41.

185. Roman, B.L. and K. Pekkan, *Mechanotransduction in embryonic vascular development.* Biomech Model Mechanobiol, 2012. 11(8): p. 1149-68.

186. Boselli, F., J.B. Freund, and J. Vermot, *Blood flow mechanics in cardiovascular development.* Cell Mol Life Sci, 2015. 72(13): p. 2545-59.

187. Bakker, J.L., H. Meijers-Heijboer, and H. Verheul, *Novel strategies towards the use of anti-angiogenic agents in breast cancer.* Eur J Pharmacol, 2013. 717(1-3): p. 36-9.

188. Prokopiou, E.M., S.A. Ryder, and J.J. Walsh, *Tumour vasculature targeting agents in hybrid/conjugate drugs.* Angiogenesis, 2013. 16(3): p. 503-24.

189. Kim, B., et al., *Exercise-mediated wall shear stress increases mitochondrial biogenesis in vascular endothelium.* PLoS One, 2014. 9(11): p. e111409.

190. Wright, G.L., et al., *VEGF stimulation of mitochondrial biogenesis: requirement of AKT3 kinase.* FASEB J, 2008. 22(9): p. 3264-75.

191. Duluc, L., et al., *Delphinidin inhibits VEGF induced-mitochondrial biogenesis and Akt activation in endothelial cells.* Int J Biochem Cell Biol, 2014. 53: p. 9-14.

192. Doddaballapur, A., et al., *Laminar shear stress inhibits endothelial cell metabolism via KLF2-mediated repression of PFKFB3.* Arterioscler Thromb Vasc Biol, 2015. 35(1): p. 137-45.

193. Jen, N., et al., *Atrial fibrillation pacing decreases intravascular shear stress in a New Zealand white rabbit model: implications in endothelial function.* Biomech Model Mechanobiol, 2013. 12(4): p. 735-45.

194. Subramaniam, S.R., et al., *Region specific mitochondrial impairment in mice with widespread overexpression of alpha-synuclein.* Neurobiology of Disease, 2014. 70: p. 204-213.

195. TeSlaa, T. and M.A. Teitell, *Techniques to Monitor Glycolysis.* Methods in enzymology, 2014. 542: p. 91-114.

196. Ping, P., et al., *Formation of protein kinase C(epsilon)-Lck signaling modules confers cardioprotection.* J Clin Invest, 2002. 109(4): p. 499-507.

197. Pass, J.M., et al., *PKCepsilon activation induces dichotomous cardiac phenotypes and modulates PKCepsilon-RACK interactions and RACK expression.* Am J Physiol Heart Circ Physiol, 2001. 280(3): p. H946-55.

198. Mayr, M., et al., *Combined metabolomic and proteomic analysis of human atrial fibrillation.* J Am Coll Cardiol, 2008. 51(5): p. 585-94.

199. Nowak, G., D. Bakajsova, and A.M. Samarel, *Protein kinase C-epsilon activation induces mitochondrial dysfunction and fragmentation in renal proximal tubules.* Am J Physiol Renal Physiol, 2011. 301(1): p. F197-208.

200. Li, R., et al., *Ultrafine particles from diesel engines induce vascular oxidative stress via JNK activation.* Free Radic Biol Med, 2009. 46(6): p. 775-82.

201. Harrison, D., et al., *Role of oxidative stress in atherosclerosis.* Am J Cardiol, 2003. 91(3A): p. 7A-11A.

202. Shyy, J.Y. and S. Chien, *Role of integrins in endothelial mechanosensing of shear stress.* Circ Res, 2002. 91(9): p. 769-75.

203. Vander Heiden, M.G., et al., *Metabolic pathway alterations that support cell proliferation.* Cold Spring Harb Symp Quant Biol, 2011. 76: p. 325-34.

204. Chen, C.H., M.O. Gray, and D. Mochly-Rosen, *Cardioprotection from ischemia by a brief exposure to physiological levels of ethanol: role of epsilon protein kinase C.* Proc Natl Acad Sci U S A, 1999. 96(22): p. 12784-9.

205. Dorn, G.W., 2nd, et al., *Sustained in vivo cardiac protection by a rationally designed peptide that causes epsilon protein kinase C translocation.* Proc Natl Acad Sci U S A, 1999. 96(22): p. 12798-803.

206. Chen, C.H., et al., *Activation of aldehyde dehydrogenase-2 reduces ischemic damage to the heart.* Science, 2008. 321(5895): p. 1493-5.

207. McCarthy, J., et al., *PKCepsilon activation augments cardiac mitochondrial respiratory post-anoxic reserve--a putative mechanism in PKCepsilon cardioprotection.* J Mol Cell Cardiol, 2005. 38(4): p. 697-700.

208. Depre, C., J.L. Vanoverschelde, and H. Taegtmeyer, *Glucose for the heart.* Circulation, 1999. 99(4): p. 578-88.

209. Vogt, A.M., et al., *Regulation of glycolytic flux in ischemic preconditioning. A study employing metabolic control analysis.* J Biol Chem, 2002. 277(27): p. 24411-9.

210. Kulkeaw, K. and D. Sugiyama, *Zebrafish erythropoiesis and the utility of fish as models of anemia.* Stem Cell Research & Therapy, 2012. 3(6): p. 55-55.

211. Chu, C.Y., et al., *The zebrafish erythropoietin: functional identification and biochemical characterization.* FEBS Lett, 2007. 581(22): p. 4265-71.

212. Lee, I., E. Bender, and B. Kadenbach, *Control of mitochondrial membrane potential and ROS formation by reversible phosphorylation of cytochrome c oxidase.* Molecular and Cellular Biochemistry, 2002. 234(1): p. 63-70.

213. Inoue, N., et al., *Shear stress modulates expression of Cu/Zn superoxide dismutase in human aortic endothelial gels.* Circulation Research, 1996. 79(1): p. 32-37.

214. Ku, D.N., et al., *Pulsatile Flow and Atherosclerosis in the Human Carotid Bifurcation - Positive Correlation between Plaque Location and Low and Oscillating Shear-Stress.* Arteriosclerosis, 1985. 5(3): p. 293-302.

215. Rouhanizadeh, M., et al., *MEMS sensors to resolve spatial variations in shear stress in a 3-D blood vessel bifurcation model.* IEEE Sensors Journal, 2006. 6(1): p. 78-88.

216. Hsiai, T.K., et al., *Endothelial cell dynamics under pulsating flows: Significance of high versus low shear stress slew rates (delta tau/delta t).* Annals of Biomedical Engineering, 2002. 30(5): p. 646-656.

217. Floryk, D. and J. Houstek, *Tetramethyl rhodamine methyl ester (TMRM) is suitable for cytofluorometric measurements of mitochondrial membrane potential in cells treated with digitonin.* Bioscience Reports, 1999. 19(1): p. 27-34.

218. Scaduto, R.C. and L.W. Grotyohann, *Measurement of mitochondrial membrane potential using fluorescent rhodamine derivatives.* Biophysical Journal, 1999. 76(1): p. 469-477.

219. Nicholls, D.G., *Simultaneous monitoring of ionophore- and inhibitor-mediated plasma and mitochondrial membrane potential changes in cultured neurons.* Journal of Biological Chemistry, 2006. 281(21): p. 14864-14874.

220. Cassarino, D.S., et al., *Cyclosporin A increases resting mitochondrial membrane potential in SY5Y cells and reverses the depressed mitochondrial membrane potential of Alzheimer's disease cybrids.* Biochemical and Biophysical Research Communications, 1998. 248(1): p. 168-173.

221. Ward, M.W., et al., *Mitochondrial membrane potential and glutamate excitotoxicity in cultured cerebellar granule cells.* Journal of Neuroscience, 2000. 20(19): p. 7208-7219.

222. Hwang, J., et al., *Pulsatile versus oscillatory shear stress regulates NADPH oxidase subunit expression - Implication for native LDL oxidation.* Circulation Research, 2003. 93(12): p. 1225-1232.

223. Ai, L., et al., *Shear stress influences spatial variations in vascular Mn-SOD expression: implication for LDL nitration.* Am J Physiol Cell Physiol, 2008. 294(6): p. C1576-85.

224. Nicholls, D.G., *Influence of Respiration and Atp Hydrolysis on Proton-Electrochemical Gradient across Inner Membrane of Rat-Liver Mitochondria as Determined by Ion Distribution.* European Journal of Biochemistry, 1974. 50(1): p. 305-315.

225. Loew, L.M., et al., *Imaging in 5 Dimensions - Time-Dependent Membrane-Potentials in Individual Mitochondria.* Biophysical Journal, 1993. 65(6): p. 2396-2407.

226. Sompol, P., et al., *A neuronal model of Alzheimer's disease: an insight into the mechanisms of oxidative stress-mediated mitochondrial injury.* Neuroscience, 2008. 153(1): p. 120-30.

227. Xiang, N., R. Zhao, and W. Zhong, *Sodium selenite induces apoptosis by generation of superoxide via the mitochondrial-dependent pathway in human prostate cancer cells.* Cancer Chemother Pharmacol, 2009. 63(2): p. 351-62.

228. Behrend, L., et al., *Manganese superoxide dismutase induces p53-dependent senescence in colorectal cancer cells.* Mol Cell Biol, 2005. 25(17): p. 7758-69.

229. Cai, H. and D.G. Harrison, *Endothelial dysfunction in cardiovascular diseases: the role of oxidant stress.* Circ Res, 2000. 87(10): p. 840-4.
230. Tomasian, D., J.F. Keaney, and J.A. Vita, *Antioxidants and the bioactivity of endothelium-derived nitric oxide.* Cardiovasc Res, 2000. 47(3): p. 426-35.
231. Yong, X., et al., *IC-integrated flexible shear-stress sensor skin.* Microelectromechanical Systems, Journal of, 2003. 12(5): p. 740-747.
232. Wu, L., et al., *Augmentation of late sodium current unmasks the proarrhythmic effects of amiodarone.* Cardiovasc Res, 2008. 77(3): p. 481-8.
233. Zon, L.I. and R.T. Peterson, *In vivo drug discovery in the zebrafish.* Nat Rev Drug Discov, 2005. 4(1): p. 35-44.
234. Rihel, J. and A.F. Schier, *Behavioral screening for neuroactive drugs in zebrafish.* Dev Neurobiol, 2012. 72(3): p. 373-85.
235. Videler, J., *The structure of the swimming apparatus: shape, skin and special adaptations*, in *Fish Swimming*. 1993, Springer Netherlands. p. 71-92.
236. Wang, Z., A.A. Volinsky, and N.D. Gallant, *Crosslinking effect on polydimethylsiloxane elastic modulus measured by custom-built compression instrument.* Journal of Applied Polymer Science, 2014. 131(22): p. n/a-n/a.
237. Lin, J.C.H., G. Lam, and T. Yu-Chong. *Viscoplasticity of parylene-C film at body temperature*. in *Micro Electro Mechanical Systems (MEMS), 2012 IEEE 25th International Conference on*. 2012.
238. Lin, J., *Chapter 5 Characterstics of Parylene-C Film*, in *Electrical Engineering*2012, California Institute of Technology.
239. Do, H., *Dynamic Mechanical Analysis of Silicone Elastomer*, in *Electrical Engineering*2012, California Institute of Technology.
240. Chang, J.H.-C., *Wireless parylene-based retinal implant*, 2014, California Insitute of Technology.
241. Pan, J. and W.J. Tompkins, *A real-time QRS detection algorithm.* IEEE Trans Biomed Eng, 1985. 32(3): p. 230-6.
242. Hamilton, P.S. and W.J. Tompkins, *Quantitative investigation of QRS detection rules using the MIT/BIH arrhythmia database.* IEEE Trans Biomed Eng, 1986. 33(12): p. 1157-65.
243. Yu, F., et al., *Flexible microelectrode arrays to interface epicardial electrical signals with intracardial calcium transients in zebrafish hearts.* Biomed Microdevices, 2012. 14(2): p. 357-66.
244. Zhao, Y., et al., *Dry-contact microelectrode membranes for wireless detection of electrical phenotypes in neonatal mouse hearts.* Biomed Microdevices, 2015. 17(2): p. 9912.
245. Labroo, P. and Y. Cui, *Flexible graphene bio-nanosensor for lactate.* Biosens Bioelectron, 2013. 41: p. 852-6.
246. Muller, J.E., et al., *Circadian variation in the frequency of onset of acute myocardial infarction.* N Engl J Med, 1985. 313(21): p. 1315-22.
247. Boudreau, P., et al., *Circadian variation of heart rate variability across sleep stages.* Sleep, 2013. 36(12): p. 1919-28.
248. *Trans-NIH Zebrafish Initiative*. Available from: www.nih.gov/science/models/zebrafish/.
249. Arrenberg, A.B., et al., *Optogenetic control of cardiac function.* Science, 2010. 330(6006): p. 971-4.